DEVELOPMENT OF STRENGTH REDUCTION FACTORS FOR PERFORMANCE-BASED SEISMIC DESIGN OF BRIDGES IN FAR-FAULT SEISMIC REGIONS

A THESIS SUBMITTED TO
THE GRADUATE SCHOOL OF NATURAL AND APPLIED SCIENCES
OF
MIDDLE EAST TECHNICAL UNIVERSITY

BY

TAREQ Z. S. RABAIA

IN PARTIAL FULFILLMENT OF THE REQUIREMENTS
FOR
THE DEGREE OF MASTER OF SCIENCE
IN
ENGINEERING SCIENCES

SEPTEMBER 2021

Approval of the thesis:

DEVELOPMENT OF STRENGTH REDUCTION FACTORS FOR PERFORMANCE-BASED SEISMIC DESIGN OF BRIDGES IN FAR-FAULT SEISMIC REGIONS

submitted by **TAREQ Z. S. RABAIA** in partial fulfillment of the requirements for the degree of **Master of Science** i**n Engineering Sciences, Middle East Technical University** by,

Prof. Dr. Halil Kalıpçılar

Dean, Graduate School of **Natural and Applied Sciences**

Prof. Dr. Murat Dicleli

Head of the Department, **Engineering Sciences**

Prof. Dr. Murat Dicleli

Supervisor, **Engineering Sciences, METU**

Examining Committee Members:

Assoc. Prof. Dr. Ferhat Akgül

Engineering Sciences, METU

Prof. Dr. Murat Dicleli

Engineering Sciences, METU

Prof. Dr. Tolga Akış

Civil Engineering, Atılım University

Date: 06.09.2021

I hereby declare that all information in this document has been obtained and presented in accordance with academic rules and ethical conduct. I also declare that, as required by these rules and conduct, I have fully cited and referenced all material and results that are not original to this work.

Name Last name : Tareq Z. S. Rabaia

Signature:

ABSTRACT

DEVELOPMENT OF STRENGTH REDUCTION FACTORS FOR PERFORMANCE-BASED SEISMIC DESIGN OF BRIDGES IN FAR-FAULT SEISMIC REGIONS

Rabaia, Tareq Z. S.
Master of Science, Engineering Sciences
Supervisor: Prof. Dr. Murat Dicleli

September 2021, 132 pages

In this thesis, a methodology to develop strength reduction factors for performance-based seismic design of bridges in far-fault seismic regions is presented. The presented methodology is mainly based on performing linear 5%-damped response spectrum analyses (RSA) and nonlinear time history analyses (NTHA) of bridge piers modeled as single degree of freedom (SDOF) systems. Bridge piers of both circular and rectangular sections are analyzed for wide ranges of various design parameters considering several substructure-superstructure connections. Subsequently, a set of strength reduction factor (R-factor) equations derived by performing parametric linear regression analyses on the data resulted from the conducted structural analyses is proposed. The proposed R-factor equations are formulated in terms of the design parameters that significantly affect R-factor, and the maximum displacement ductility obtained from the NTHA considering various failure modes such as shear, shear-flexural, and flexural failure modes. Moreover, other equations to estimate the yield curvature, ultimate curvature, and yield moment capacities of bridge piers are proposed. Such equations that could be used to estimate

the design displacement and flexural strength capacity of piers in the performance-based seismic design of bridges. Based on the derived equations in this thesis, a new performance-based seismic design procedure for bridge structures that mainly depends on R-factor is proposed. Finally, the implementation of the proposed design procedure is explained via design examples of bridge structures.

Keywords: Strength Reduction Factor, Performance-Based Design, Seismic Design, Bridges.

ÖZ

UZAK FAY SİSMİK BÖLGELERİNDE KÖPRÜLERİN PERFORMANSA DAYALI SİSMİK TASARIMI İÇİN DEPREM YÜKÜ AZALTMA KATSAYILARININ GELİŞTİRİLMESİ

Rabaia, Tareq Z. S.
Yüksek Lisans, Mühendislik Bilimleri
Tez Yöneticisi: Prof. Dr. Murat Dicleli

Eylül 2021, 132 sayfa

Bu tezde, uzak fay sismik bölgelerinde köprülerin performansa dayali sismik tasarimi için deprem yükü azaltma katsayilarinin geliştirilmesi için bir yöntem sunulmaktadır. Bu yöntem, esasen köprü ayaklarının %5- sönümlemeli deprem tasarım spektrum analizlerinin (RSA) ve doğrusal olmayan zaman tanım alanı analizlerinin (NTHA) tek serbestlik dereceli (SDOF) sistemlerinin sunulmasına dayanmaktadır. Dairesel ve dikdörtgenel koprü ayağı kesitleri pek çok altyapı-üstyapı bağlatıları dikkat alınarak analiz edilmişlerdir. Gerçekleştirilen yapı analizlerin sonucunda paramatrik doğrusal regresyon analizleri kullanarak bir set deprem yükü azaltma katsayisi (R-faktör) denklemleri sunulmaktadır. Sunulan R-faktör denklemleri, R-faktörünü belirgin biçimde etkileyen tasarım parametreleri ile kesme, Kesme-dönme, ve dönme başarısızlık modları gibi pek çok mod göz önünde bulundurularak gerçekleştirilen NTHA'dan elde edilen maksimum deplasman sünekliği esas alınarak elde edilmiştir. Ek olarak, köprü ayaklarının akma eğrisi, maksimum eğrisi, ve akma moment kapasitelerini değerlendirmek için denklemler sunulmuştur. Bu tür denklemler, köprülerin performansa dayalı sismik tasarımında,

köprü ayaklarının tasarım deplasmanını ve dönme mukavemet kapasitesini hesaplamak için kullanılabilir. Bu tezdeki sunulan denklemler esas alınarak, R-faktörü temelli yeni bir performansa dayalı sismik tasarım prosedürü sunulmaktadır. Son olarak, köprü yapılarının tasarım örnekleri vasitasiyla sunulan tasarım prosedürünün uygulaması ortaya koyulmaktadır.

Anahtar Kelimeler: Deprem Yükü Azaltma Katsayısı, Performansa Dayalı Tasarım, Sismik Tasarım, Köprüler.

To my family

ACKNOWLEDGMENTS

I would like to express my deep gratitude and appreciation to my supervisor Prof. Dr. Murat Dicleli for his genuine support, supervision, and guidance. This work would not have been accomplished without his motivation and encouragement.

I would like to thank Assoc. Prof. Ferhat Akgül, and Prof. Dr. Tolga Akış for being in my thesis committee and providing me valuable feedback.

I acknowledge that the computing sources used in this work were provided by the National Center for High Performance Computing of Turkey (UHeM) under grant number 1008502020.

I would like to thank my family and friends for their support.

TABLE OF CONTENTS

LIST OF TABLES

TABLES

LIST OF FIGURES

FIGURES

LIST OF ABBREVIATIONS

ABBREVIATIONS

SMSA: Single-Mode Spectral Analyses.

MMSA: Multi-Mode Spectral Analyses.

NTHA: Nonlinear Time History Analyses.

RSA: Response Spectrum Analyses.

R-factor: Strength Reduction Factor.

RC: Reinforced Concrete.

FFGM: Far-Fault Ground Motions.

SDOF: Single Degree of Freedom.

PGA: Peak Ground Acceleration.

PGV: Peak Ground Velocity.

MDOF: Multi-Degree of Freedom.

MLSRA: Minimum Least Square Regression Analyses.

PCA: Principal Components Analysis.

CHAPTER 1

INTRODUCTION

1.1 Motivation and Problem Definition

The concept of performance-based design has been the concern of many researchers in the past decades. Performance-based seismic design is a methodology based on designing structures able to achieve predefined performance objectives under certain seismic levels. The performance objectives are defined using quantitative limit states expressed in terms of loads, stresses, strains, and displacement [1], [2]. The importance of such methodology does not only emerge from the need of having structures capable of providing life safety but also ensuring serviceability, acceptable levels of damage, and acceptable economic losses during seismic actions [3]. Performance-based seismic design enables engineers to come up with more reliable designs by involving structural performance targets in the design stages. Nevertheless, it helps designers and decision-makers to have more realistic loss estimates and risk management as it relies on probabilistic approaches in determining seismic capacities and demands [3], [4].

The rising interest in performance-based seismic design is derived by the need to improve current design codes. After Northridge (1994) and Kobe (1995) earthquakes, researchers and engineers started to call for new design procedures capable of resulting in more reliable structures. Although many structures sustained during these earthquakes, the economic losses caused by the extensive damage repair and the loss of use were very high [2]. Thus, many research studies emphasized that seismic design codes should not only ensure collapse prevention, but they should be able also to account for acceptable damage levels during strong seismic actions [5].

Most of current seismic design codes, such as AASHTO [6], Eurocode [7], and ASCE 7-16 [8], adopt conventional design procedures based on capacity design principle. Such design procedures rely on force-based design that mainly depends on strength rather than ductility. In force-based seismic design, the design forces are obtained by performing various structural analysis methods. Some of these methods are linear such as single-mode spectral analyses (SMSA) method, multi-mode spectral analyses (MMSA) method, and uniform load method. As the seismic behavior of structures is inherently nonlinear, other nonlinear methods such as nonlinear time history analyses (NTHA) method and nonlinear pushover analyses method are preferably used to provide better prediction of the actual seismic response of structures. Nonlinear analyses methods are essentially used in the design of structures expected to achieve certain performance levels during strong seismic actions.

However, the use of nonlinear analyses methods is considered unpractical as they require huge computational efforts where suitable ground motion records representing site conditions are needed to be selected and scaled to match the design spectrum. Therefore, linear analyses methods are believed to be more practical for their simplicity and ease of implementation. In practice, engineers tend to design structures by performing response spectrum analyses (RSA) procedures followed by nonlinear analyses methods to verify the capability of the designed structures to resist seismic loads efficiently. Due to the inelastic behavior that structures exhibit during seismic actions, the elastic linear analyses procedures need to be modified in such a way that they become equivalent to the nonlinear analyses. Therefore, strength reduction factors (response modification factors) are used to reduce the demand elastic forces resulting in more realistic designs.

The importance of strength reduction factor (R-Factor) emerges from the fact that in the seismic design of structures, R-factors are used to reduce the elastic design forces to a certain level accounting for the expected strength capacity of structures. Moreover, the application of R-factor, which reflects the available ductility in structures, is essentially used to ensure the capability of a structure to dissipate

seismic energy inelastically by allowing the structure to undergo plastic deformations and have acceptable damage level within the desired performance limit states [7], [9].

Although some design provisions recommend R-factor values to ensure ductile seismic response of structures, the bases on which R-factors are evaluated are still unclear, leaving the door wide open for engineering judgement. The error margin ensued from relying on engineering judgement in R-factor evaluation leads to misestimate the energy dissipation capacity of structures. Consequently, several design iterations are needed to be conducted, followed by series of nonlinear seismic assessment analyses (e.g. Pushover and time history analyses) till the target performance level is achieved.

The main reason R-factor estimation is a challenging issue is that the value of R-factor significantly depends on parameters, some of which are obtained from the outcome of the design procedure where R-factor is essentially used. Indeed, it is inevitably correlated to a target damage level expected to be within predefined limit states varying from a design code to another. Lastly, the variety of the seismic and structural parameters that affect R-factor, as it represents the balance point between the seismic demand and capacity of structures, which might have different types and categories.

1.2 The Objective of the Thesis

The objective of this thesis is to develop a methodology to estimate the strength reduction factor (R-factor) for performance-based seismic design of RC bridges. Moreover, this study aims to propose R-factor estimation equations for bridge piers exposed to far-fault ground motions (FFGM). Such simple equations mainly depend on various design parameters, including the tip displacement of bridge piers, paving the way to develop a new performance-based seismic design procedure that could be incorporated into seismic design codes of bridge structures.

Indeed, a set of expressions to estimate curvature and strength capacities of bridge piers is aimed to be proposed and integrated with the developed design procedure.

1.3 Proposed Methodology and Procedures

In this thesis, a methodology to develop strength reduction factors (R-factor) for performance-based seismic design of RC bridges is introduced. The introduced methodology is developed based on calculating R-factors for bridge piers expected to resist seismic forces during earthquakes. Therefore, piers of both circular and rectangular sections are modeled as single degree of freedom (SDOF) systems, where the corresponding arbitrary dynamic mass of superstructure is represented by a lumped mass at pier's top. Moreover, piers are classified according to their substructure-superstructure connection into three types such as pinned, rotationally fixed, and elastomeric bearing connected piers.

The R-factor, which is defined as the ratio of the elastic seismic force to the yield strength capacity of an element, is derived by performing 5%-damped linear response spectrum analysis (RSA) and nonlinear time history analysis (NTHA) for many piers considering wide ranges of various design parameters such as design spectrum, natural period, aspect ratio of pier, arbitrary mass of pier, bearing stiffness, longitudinal reinforcement ratio, transverse reinforcement ratio, and the unconfined compressive strength of concrete. The ranges of these design parameters are determined to be within the limits specified in common seismic design codes such as AASTHO [6], and Eurocode [7]. Moreover, a set of 110 far-fault ground motions (FFGM) of different soil types is acquired from the PEER database [10]. The ground motions are grouped according to their peak ground acceleration to peak ground velocity (PGA/PGV) ratios into 10 groups each of 11 ground motions. These ground motions are selected carefully to represent different soil types as A, B, C, and D. The 5%-damped spectra of the ground motions are obtained, where the smoothed average response spectrum of each group is used as a design spectrum scaled with respect to various PGA values. As the PGA/PGV ratio is not often used in engineering practice,

it is correlated to the second corner period of the design spectrum, which is considered as an additional design parameter.

After determining the ranges of the considered design parameters, the nonlinear behavior of piers caused by the material nonlinearities at section levels is simulated using idealized moment-curvature relationships defined at specific plastic hinge locations along pier length. Therefore, parametric sectional analyses are performed considering the adopted sectional design parameters to obtain the corresponding theoretical moment-curvature relationships. Subsequently, the obtained moment-curvatures relationships are idealized, and the related sectional capacities are determined. From the results of the performed parametric sectional analyses, the effects of various sectional parameters on curvature and yield moment capacities of RC sections are investigated. Moreover, a set of equations to estimate yield curvature, ultimate curvature, and yield moment capacities for both circular and rectangular RC sections are derived.

Afterwards, the strength reduction factors of the considered SDOF systems are calculated by performing both RSA and NTHA. From RSA, the elastic demand forces are obtained, where the corresponding inelastic demand displacements are calculated as the averaged maximum displacements resulted from NTHA for each group of ground motions. In the performed NTHA, the IMK pinching hysteretic model [11] is used to simulate the seismic behavior of the SDOF systems considering several failure modes such as shear, shear-flexure combined, and flexure failure mode. Then, parametric RSA and NTHA are performed in parallel for a large number of SDOF systems by writing structural analysis programs in OpenSees software [12].

As a result of the performed parametric structural analyses, a total of 9 data sets corresponding to SDOF systems of piers considering their substructure-superstructure connection, section type, and the direction of analysis (for rectangular sections) are acquired. The acquired data sets are mined and structured in terms of the adopted design parameters as well as both the averaged tip displacements and the corresponding R-factor values. Consequently, 9 R-factor equations are derived by

performing regression data analyses on the available data. The derived equations are expressed in simple form as a function of the design parameters affecting R-factor significantly and the displacement ductility of piers.

Based on the derived R-factor equations presented in this thesis, a new performance-based seismic design procedure is proposed. The proposed procedure is implemented and explained throughout design examples of RC bridges with various configurations. Lastly, the final designs of these bridges are verified by performing NTHA in both transverse and longitudinal directions.

1.4 Contributions and Novelties

The contributions and novelties of this thesis are as follows:

- A new concept of ‘’performance-based R-factor’’ is introduced. The introduced concept relies on making a relationship between the strength reduction factor (R-factor) used in the seismic design of bridge structures and the target design displacement. In other words, this concept redefines R-factor not only as a factor used to reduce the elastic design force to make use of the available plastic capacity of structures, but also it correlates R-factor to a specific design displacement.

- A new methodology to estimate the ‘’performance-based R-factor’’ of bridges is proposed. The proposed methodology spots the light on several design parameters differentiating the ways in which R factors are generated. It is based on simple structural modeling of bridge piers as the main earthquake resisting elements of bridges where lumped plasticity approach is adopted by localizing damage in plastic hinges. In this methodology, advanced plastic hinge hysteretic models are used accounting for different failure modes, which significantly affect the energy dissipation mechanism of structures. Furthermore, the effects of bridge design parameters on R-

factor are examined, and performance-based R-factor estimation equations are proposed.

- A set of equations to estimate the yield curvature, ultimate curvature, and yield moment capacities of reinforced concrete sections of bridge piers is proposed. The proposed equations are suggested to be used in the preliminary design and structural assessment stages of bridges without conducting sectional analyses.

- A new performance-based seismic design procedure for RC bridges is proposed in this thesis. The proposed design procedure mainly depends on the performance-based R-factor, which is employed in reducing the design elastic forces, ensuring inelastic behavior with a certain target tip displacement. The target tip displacement of a pier is calculated based on the desired seismic performance level and predefined damage limit states at plastic hinge locations. Such design procedure is code-independent and might be incorporated into different design codes regardless of the damage limit states adopted. Moreover, several advantages come out from using this design procedure as it is simple, enables designers to have optimal designs, and reduces the need for performing rigorous nonlinear structural analyses that are complex and time-consuming rather than being done using expensive structural analysis software.

1.5 The Outline of the Thesis

Chapter 2 presents a literature review of various topics related to the seismic design of structures. It begins with introducing a review of the available equations and expressions used to estimate the yield and ultimate curvature capacities of RC elements. Next, it introduces an overview of the strength reduction factor equations presented by several research studies and design codes. Then, Chapter 2 provides an

overview of the performance-based seismic design procedures existing in literature and seismic design codes.

Chapter 3 introduces the design parameters anticipated to have significant effects on the strength reduction factor. Indeed, it presents the ranges of the considered parameters adopted in the parametric analyses performed in this thesis.

Chapter 4 presents the performed sectional analyses of bridge piers based on the adopted sectional design parameters. It introduces the material models used in modeling the RC sections. It also provides the details of the procedures used to obtain the idealized moment-curvature relationships used in simulating the nonlinear behavior of piers. Moreover, Chapter 4 proposes a set of equations to estimate the yield curvature, ultimate curvature, and yield moment capacities of RC pier sections. The proposed equations in this chapter are expressed in terms of the design parameters proven to affect the curvature and strength capacities of sections significantly. Finally, the performance of the proposed equations is investigated by comparing the estimated values with the actual results.

Chapter 5 begins with modeling bridge piers as SDOF systems corresponding for different substructure-superstructure connection types. Next, the performed parametric RSA and NTHA are thoroughly explained and discussed. Then, the strength reduction factors of the considered SDOF systems are calculated. Next, the datasets obtained from the performed structural analyses are mined and structured in matrice forms. Subsequently, the data analysis procedures and the data model used in deriving the R-factor equations are presented. As a result, a total of 9 R-factor equations are proposed. Finally, the accuracy of the proposed R-factor equations is examined by performing error performance analyses.

Chapter 6 introduces a new performance-based seismic design procedure of bridges based on the equations proposed in Chapter 4 and Chapter 5. The application of the proposed procedure is explicitly explained via various bridge design examples.

Chapter 7 presents a brief summary of all the works done in this thesis. It also provides conclusions of the results obtained from the performed analyses. Furthermore, it discusses the limitations of the equations and the design procedure proposed in this thesis.

CHAPTER 2

LITERATURE REVIEW

2.1 Introduction

In this chapter, a review of the commonly used equations/expressions in estimating the displacement capacities of RC columns available in literature is done. Indeed, an overview of R-factors and R-factor equations, present in different design standards and those proposed in various research studies, is presented. Moreover, famous performance-based seismic design procedures available in literature are discussed.

2.2 Sectional Properties of RC Sections

In the seismic design of structures, the required strength and displacement capacities of reinforced concrete elements are determined throughout several assumptions aiming to properly simulate the actual seismic performance of structures during earthquake excitations. As recommended by various design codes, the seismic response of structures is determined by performing different linear analyses methods such as uniform load method, single-mode spectral analyses (SMSA) method, and multi-mode spectral analyses (MMSA) method. These methods mainly depend on estimating the effective stiffness of structures, which is vital for predicting the natural period and hence the structural seismic behavior.

Design standards such as AASHTO [6], Eurocode [7], and ASCE 7-16 [8] propose several methods to estimate the effective stiffness of structures. These methods are mainly based on estimating the cracked section flexural stiffness of structural elements. However, there is still no accurate estimation of the effective flexural stiffness as it depends on many design parameters determining the strength and displacement capacities of structural elements. Thus, the error ensued from

misestimating the effective stiffness might result in errors in calculating the effective natural period and hence, the design forces of structures.

According to Priestley et al. [1], the effective stiffness of reinforced concrete sections is determined based on the nominal point of the idealized moment-curvature relationship. In other words, it is defined as the stiffness corresponding to the elastic part of the idealized moment-curvature relationship calculated as follows [1]:

$$EI_{eff} = \frac{M_N}{\varphi_y} \quad (1)$$

where EI_{eff} is the effective flexural stiffness, M_N is the nominal moment capacity, and φ_y is the effective yield curvature of reinforced concrete section. Moreover, Priestley et al. [1] presented formulas to estimate yield and ultimate tip displacements of piers based on their yield and ultimate curvature capacities.

Therefore, the accurate estimation of curvature and strength capacities of structural elements such as piers is very important in the seismic design of structures. In case of knowing sectional properties such as effective yield curvature, ultimate curvature, and nominal moment capacities of structural components, the corresponding effective stiffness, yield, and ultimate displacements of elements could be easily calculated [1].

2.2.1 Yield and Ultimate Curvature Equations Available in Literature

To the author's knowledge, while several studies have been carried out to provide expressions for estimating the effective yield curvature of columns, limited studies focused on proposing accurate estimates for ultimate curvature. Therefore, a detailed review of the yield and ultimate curvature equations available in literature are summarized as follows:

In their study, Priestley et al. [1] suggested an equation for estimating the effective yield curvature of circular reinforced concrete bridge columns. The suggested

equation is simple as it depends on the diameter of the gross section and the yield strain of the longitudinal reinforcements of columns. However, it lacks other parameters such as axial load and the characteristic compressive strength of concrete, which are anticipated to significantly affect yield displacement and strength of columns. Moreover, the effects of the amounts of longitudinal and transverse reinforcements on yield curvature are not included in the suggested equation, which is presented as follows:

$$\varphi_y = 2.25\frac{\varepsilon_{ys}}{D} \tag{2}$$

where ε_{ys} is the yield strain of longitudinal reinforcements, and D is the gross section diameter.

In the same study, Priestley et al. [1] proposed an expression to estimate the ultimate curvature of circular bridge piers. Such an expression based on the ultimate strain limits of both concrete ε_{cu}, and steel ε_{su} as well as the neutral axis depth c of pier section, which is calculated by the following formula:

$$\frac{c}{D} = 0.2 + 0.65\frac{P}{f'_{ce}\,A_g} \tag{3}$$

where P is the axial load, A_g is the gross area of section, and f'_{ce} is the expected compressive strength of concrete. Accordingly, the ultimate curvature is calculated as follows:

$$\varphi_u = min(\frac{\varepsilon_{cu}}{c}, \frac{0.6\varepsilon_{su}}{d-c}) \tag{4}$$

where φ_u is the ultimate curvature, d is the effective depth of column section, and ε_{cu} is the ultimate strain capacity of confined concrete, which is evaluated by the formula given by [13].

Although the proposed ultimate curvature formula is simple and depends on the strain capacity of both confined concrete and reinforcing steel, it relies on estimating the depth of neutral axis, which is significantly affected by several factors such as the quantity of longitudinal reinforcements and steel strength capacity that are not indicated in the given expressions. Thus, the error that might arise from estimating neutral axis depth could lead to misestimating the ultimate curvature.

Another research study by Montes and Aschleim [14] presented a set of yield curvature estimation formulas for circular and rectangular columns. In these formulas, the effective yield curvature is expressed as a function of the effective depth d of column section and the yield strain of longitudinal reinforcements. Moreover, the accuracy of the proposed formulas is improved by including the axial load effect, which is expressed in the form of axial load ratio.

The yield curvature formulas for circular sections are given as follows:

$$\varphi_y = 2.4\frac{\varepsilon_{ys}}{d} \quad \text{for steel B}-400$$

$$\varphi_y = 2.3\frac{\varepsilon_{ys}}{d} \quad \text{for steel B}-500 \tag{5}$$

By including the axial load, the yield curvature is estimated using the following formulas;

$$\varphi_y = \frac{\varepsilon_{ys}}{d}[2.5 - (a - b\frac{P}{f_{cd}\,A_g})^2] \quad \text{for steel B}-400$$

$$\varphi_y = \frac{\varepsilon_{ys}}{d}[2.4 - (a - b\frac{P}{f_{cd}\,A_g})^2] \quad \text{for steel B}-500 \tag{6}$$

where *a*, and *b* are coefficients expressed as a function of section diameter

The yield curvature formulas for rectangular sections are given as follows:

$$\varphi_y = 2.2\frac{\varepsilon_{ys}}{d} \quad \text{for steel B}-400$$

$$\varphi_y = 2.1\frac{\varepsilon_{ys}}{d} \quad \text{for steel B}-500 \tag{7}$$

By including the axial load, the yield curvature is estimated using the following formulas:

$$\varphi_y = \frac{\varepsilon_{ys}}{d}[2.3 - (0.6 - 2.5\frac{P}{f_{cd}\,A_g})^2] \quad \text{for steel B}-400$$

$$\varphi_y = \frac{\varepsilon_{ys}}{d}[2.2 - (0.6 - 2.5\frac{P}{f_{cd}\,A_g})^2] \quad \text{for steel B}-500 \tag{8}$$

Sheikh et al. [15] proposed a new expression for estimating the yield curvature based on sectional analyses of reinforced concrete circular column sections. The provided expression accounts for several sectional parameters affecting the effective yield curvature. It is expressed as a function of gross section diameter, yield strain of the longitudinal reinforcements, axial load, characteristic compressive strength of concrete, and longitudinal reinforcements ratio. It is found that expressing the yield curvature in terms of gross section diameter rather than the effective depth results in better estimation. Moreover, insignificant effect of the cover depth on the yield curvature of columns is proven. The proposed expression by [15] is given as follows:

$$\varphi_y = 2.0 \times \frac{\varepsilon_{ys}}{D^{1.1}} \times MF(f'_c) \times MF(n) \times MF(\rho) \tag{9}$$

$$MF(f'_c) = 1.25 \times {f'_c}^{-0.07}$$

$$MF(n) = 1 + (0.041 \times f'_c - 0.26) \times n - (0.043 \times f'_c + 0.85) \times n^2$$

$$MF(\rho) = \rho^{0.16}$$

where n is the axial load ratio, and ρ is the longitudinal reinforcement ratio.

Although there are various equations for estimating the yield and ultimate curvatures in literature, some equations lack important parameters that might affect the estimated curvature values, where other equations are too complex and rely on many parametric estimations. Therefore, more accurate and simple equations for estimating yield and ultimate curvatures are needed to design and assess structures.

2.3 Strength Reduction Factor

Since the appearance of the seismic design principle, huge research efforts have been made to provide reliable methods for the design of structures supposed to resist lateral forces during seismic actions. The force-based seismic design is one of the most popular design methods adopted in several design codes for many decades. In force-based seismic design, structures are designed considering their strength capacity. The strength capacity of structures in force-based seismic design is defined by the nominal yield strength, which is correlated to yield displacement capacity calculated based on the elastic properties of structures [1], [16]. During the seismic design process, the required strength is determined by reducing the resultant elastic forces obtained from linear analyses using the strength reduction factor.

Therefore, the concept of strength reduction factor became an important aspect of the force-based seismic design. The strength reduction factor is defined as the ratio of the lateral elastic demand force to the required yielding strength capacity enabling structures to maintain certain ductility under a ground motion excitation.

Various research studies have been conducted to provide better understanding of R-factor and to develop equations to estimate R-factors for structures subjected to seismic actions. One of the earliest research studies on R-factor is the study done by Newmark and Hall [17], which is considered one of the most important research efforts that improved the seismic design [18]. The study [17] proposed an expression to evaluate R-factor based on ductility μ and period *T*.

$$R = 1 \qquad \text{For } 0 \le T < \frac{T_1}{10}$$

$$R = \sqrt{2\mu - 1}\left[\frac{T_1}{4T}\right]^{2.513\, log\left[\frac{1}{\sqrt{2\mu-1}}\right]} \qquad \text{For } \frac{T_1}{10} \le T < \frac{T_1}{4}$$

$$R = \sqrt{2\mu - 1} \qquad \text{For } \frac{T_1}{4} \le T < T_1' \qquad (10)$$

$$R = \frac{T\mu}{T_1} \qquad \text{For } T_1' \le T < T_1$$

$$R = \mu \qquad \text{For } T_1 \le T < T_2$$

$$R = \mu \qquad \text{For } T_2 \le T < 10\ s$$

where T_1, T_1', and T_2 are bound periods calculated based on expressions presented in [17] is obtained considering the ratio of elastic and inelastic spectra of SDOF systems having a bilinear Force-displacement relationship. It could be noticed from the above expressions that the reduction factor is equal to 1 for structures having short natural periods, where R is equal to the displacement ductility for structures of long periods.

Another R-factor expression was proposed by Nassar & Krawinkler [19]. The proposed expression was derived using ground motion records of alluvium rock site. The hardening stiffness effect of the elastoplastic SDOF systems was included in the proposed R-factor expression as following [19]:

$$R = [c\ (\mu\ - 1)\ + 1\ ]^{1/c} \qquad (11)$$

$$c(T, \alpha) = \frac{T^a}{1+T^a} + \frac{b}{T}$$

Herein α is the hardening stiffness, and *a* & *b* are coefficients depending on α.

A site-dependent R-factor was proposed by Miranda [20], considering the reduction factor of SDOF systems using 124 records of ground motions on different soil types such as rock, alluvium, and soft soil types classified based on their shear wave velocities. The proposed R-factor expression [20] is presented as follows:

$$R = \frac{\mu - 1}{\Phi} + 1 \tag{12}$$

$$\Phi = 1 + \frac{1}{10T - \mu T} - \frac{1}{2T}\, exp(-1.5(ln(T) - 0.6)^2) \quad \text{For rock soil}$$

$$\Phi = 1 + \frac{1}{12T - \mu T} - \frac{2}{5T}\, exp(-2(ln(T) - 0.2)^2) \quad \text{For alluvium}$$

$$\Phi = 1 + \frac{T_g}{3T} - \frac{3T_g}{4T}\, exp(-3(ln(T/T_g) - 0.25)^2) \quad \text{For soft soil}$$

where T_g is called the predominant period representing the period of maximum relative velocity within the entire period domain.

It is noteworthy to mention that the aforesaid studies [17], [19], [20] are some of the significant research studies that expressed R-factor in terms of ductility and period. Along with other *R_μ_T* relationships presented in several research studies [18], [21]–[25], these expressions basically depend on ductility and the fundamental period of systems. In 1994, Miranda & Bertero [9] presented a review study of the *R_μ_T* relationships available up to that time. The study [9] concluded that the value of R-factor is significantly affected by the maximum ductility, the natural period, and the site conditions of the system, where it is much less affected by other parameters such as damping, hysteretic type, and epicenter distance of the earthquake.

Recently, new R-factor expressions were presented in various studies [26]–[28]. Yi-Feng Wu et al. [26] proposed an expression to evaluate R-factors for seismic-isolated bridges in far-fault regions using 1410 ground motions. The study [26] investigated the effects of PGA/PGV ratio of ground motions, site conditions, and the post-to-pre-yield stiffness ratio on the strength reduction factors. Consequently, the results showed that R-factor is significantly affected by PGA/PGV ratio for systems of natural period greater than the characteristic period T_g of site soil, where it is dominated by the post-to-pre-yield stiffness ratio α within the period range of 0-T_g. The proposed expression by [26] is given as follows:

$$R = 1 + (\mu - 1) \cdot \left(1 - e^{f_1(T/T_g)}\right) + (\mu - 1) \cdot f_2(\mu) \cdot T \cdot e^{f_3(T/T_g)} \cdot (PGA/PGV)^{f_4(T/T_g)} \quad (13)$$

where, $f_1, f_2, f_3, and\ f_4$ are polynomial functions expressed in terms of $T/T_g, \mu, T/T_g, and\ T/T_g$, respectively.

In their study, Y. Zhang et al. [27] proposed a damage-based strength reduction factor R_D for structures exposed to mainshock-aftershock sequence ground motions. Considering various site conditions, the study [27] investigated the effects of several parameters, including damage index, ductility, natural period, and aftershock on the strength reduction factor of SDOF systems. The study concluded that strength reduction factors significantly decrease when the damage index of systems having long natural periods is considered. Indeed, more than 25% decrease in strength reduction factor is noticed due to cumulative damage ensued from aftershocks of high intensities resulting in greater inelastic strength demands. Consequently, the study proposed R_D expression presented as follows:

$$R_D = 1 + \frac{D(\mu - 1)(a_0 T + a_1 T^2)}{(\mu + a_2)(1 + a_3 T + a_4 T^2)} \cdot \frac{1}{0.87 + 0.08\, e^{\gamma}} \quad (14)$$

where $a_0, a_1, a_2, a_3, and\ a_4$ are regression coefficients determined in [27] based on post-yield stiffness and site conditions. D is the damage index, and γ is the aftershock to mainshock intensity ratio.

Having discussed some famous and recent R-factor expressions existing in literature, one could conclude that these expressions addressed the effects of specific parameters such as ductility, natural period, post-yield stiffness, site conditions, PGA/PGV, damage, and aftershock on strength reduction factors. However, the existing R-factor expressions are either complex or missing several parameters significantly affecting the seismic response of structures. Indeed, these expressions ignore the type of structures and are not developed in consistency with design assumptions and procedures presented in design codes. Therefore, the adoption of such expressions in seismic design codes might result in unreliable designs.

Current design codes recommend R-factor values for the seismic design of different bridge elements. Most of these design codes recommend R-factors considering overstrength and demand ductility by employing the ‘’equal displacement rule’’. AASHTO LRFD code [6] expresses R-factor as constant values in table form by classifying bridge structures based on their importance classes. Considering a life safety performance level associated with hazard level of 1000-year return period, AASHTO LRFD code [6] recommends R-factors for single column bents such as 1.5, 2.0, and 3.0 corresponding for critical, essential, and other bridge importance classes, respectively. For bridges of multiple column bents, AASHTO LRFD code [6] recommends using 1.5, 3.5, and 5.0 R-factors for critical, essential, and other bridges, respectively.

Unlike AASHTO LRFD code [6], Eurocode [7] provides R-factor equation to estimate the design forces of bridges piers. According to Eurocode [7], bridges are designed for two behavior levels as limited-ductile and ductile behaviors associated with 475-year return period. In the case of piers expected to have limited-ductile behavior, a constant R-factor (expressed as q in Eurocode [7]) equals to 1.5 is used. On the other hand, bridges of ductile behavior are designed using reduction factor (q) calculated by the following equation [7]:

$$q = 3.5\,\lambda(\alpha_s) \tag{15}$$

where α_s is the shear span to section depth ratio, and $\lambda(\alpha_s)$ is given by :

$$\begin{aligned} &\lambda(\alpha_s) = 1 \quad , \quad \alpha_s \geq 3 \\ &\lambda(\alpha_s) = \sqrt{\frac{\alpha_s}{3}} \quad , \; 3 > \alpha_s \geq 1 \end{aligned} \tag{16}$$

It should be noted that the abovementioned q equation is only valid for ductile members of axial load ratio η_k not larger than 0.3. In the case of ductile members of $0.3 < \eta_k \leq 0.6$, the calculated q is reduced using the following equation:

$$q_r = q - \frac{\eta_k - 0.3}{0.3}(q - 1) \geq 1 \tag{17}$$

where q_r is the reduced reduction factor. However, for members of $\eta_k \geq 0.6$, the used reduction factor should be equal to 1.

Compared to R-factors provided by AASHTO LRFD code [6], the strength reduction factors presented in Eurocode [7] account for two performance levels, where one performance level is considered in AASHTO LRFD code [6]. Moreover, Eurocode [7] recommends different reduction factors for piers considering their flexural behavior and axial load ratios. However, due to the fact that bridges are designed using different seismic levels in both AASHTO LRFD code [6] and Eurocode [7], a comparison between strength reduction factors used in both codes should be made carefully. Moreover, different material properties and detailing techniques adopted in various international codes should be considered in such a comparison [29].

Therefore, in this thesis, new R-factor equations are proposed to be used in the performance-based seismic design of bridges. The proposed equations are presented in a simple form and expressed in terms of design parameters affecting R-factor significantly. Moreover, the proposed equations account for the design displacement ductility, which is calculated based on the desired performance level of bridge piers.

2.4 Performance-Based Seismic Design

The origin of the performance-based design is back to the 1970s, as it appeared in New Zealand for the first time [1]. Afterwards, several research efforts continued to develop performance-based design procedures capable of being incorporated with design provisions. Some of the earliest efforts that formed the basis of performance-based design are presented in SEAOC Vision 2000 [30], ATC-40 [31], and FEMA-273 [32].

The document presented by SEAOC Vision 2000 [30] is one of the first attempts to accommodate the performance-based seismic design philosophy into an applicable design procedure. It introduces five seismic performance levels paving the way for designing structures able to achieve multiple performance objectives based on

specific drift limit states. Indeed, the document recommends extending the ordinary capacity design procedures to account for the inelastic response of structures.

The ATC-40 [31] document, which is presented by the Applied Technology Council, focuses on designing concrete buildings of stated performance criteria considering the capacity spectrum. The suggested design procedure is based on expressing the force-displacement relationship of any point on the structure in terms of spectral accelerations and spectral displacements using an equivalent single degree of freedom (SDOF) system. The spectral acceleration and spectral displacement corresponding to the specified performance point of the structure are equated to the elastic demand spectra created with high damping.

The FEMA 273 document [32] presented by the Federal Emergency Management Agency proposes various performance objectives defined based on different drift ranges rather than discreet limit states. It also correlates the performance objectives with stated seismic hazard levels determined based on probabilistic hazard analyses.

Later, several research studies proposed different performance-based seismic design methodologies for the next generation of seismic design codes. One of these methodologies is known as displacement-based seismic design, which was introduced by Priestley [33], [34]. For the sake of simplicity, the displacement-based seismic design suggests expressing design limit states in terms of displacements calculated using a set of formulas based on plastic hinge rotation [1].

Regarding the seismic design of bridge structures, an early study presented in [35] proposed a displacement-based seismic design procedure for single RC bridge columns. The procedure adopts defining target displacement rather than displacement limit. It is based on converting the inelastic structural system into an equivalent elastic system called as ‘’the substitute structure’’. The substitute structure is defined by effective stiffness, effective period, and effective damping. The effective stiffness is determined with respect to the maximum displacement point of a bilinear force-displacement relationship of the system, where the effective damping is calculated based on proposed expressions enabling the inelastic structure

to be analyzed as elastic SDOF system using elastic response spectra. This procedure was extended to account for multi-degree of freedom (MDOF) bridge systems in the study presented later by Calvi & Kingsley [36]. The study [36] adopted reducing a MDOF bridge system to an equivalent SDOF system using assumed target deformation profiles based on the work equivalency principle.

Kowalsky [37] presented a direct displacement-based seismic design approach that incorporated the displacement-based seismic design philosophy into a step-by-step performance-based seismic design procedure of MDOF bride structures. The proposed design procedure starts by selecting seismic performance levels defined based on acceptable damage levels associated with earthquake intensities. Then, target displacement is evaluated by calculating the so-called ‘’damage-based displacements’’ for each column using expressions that mainly depend on column rotations at plastic hinge levels. The target displacement is obtained basically according to the critical column that is determined based on mode shapes. Next, an equivalent SDOF system of the MDOF bridge structure is characterized by defining several properties such as system target displacement, system hysteretic damping, and system mass. Then, based on the identified equivalent SDOF system, the total base shear of the SDOF system is calculated in accordance with target system displacement. Back to the MDOF bridge system, the obtained total design force is distributed to bridge columns considering displacement ductility and secant stiffness of the cracked section of each column. Subsequently, column members are designed, and the revised displacement pattern is obtained. Accordingly, the design process is considered completed when the revised displacement pattern is the same as the initial pattern.

Later, the direct displacement-based seismic design approach was extended for various inelastic displacement patterns in the study presented by [38]. The study adopted a relative stiffness index, which is expressed in terms of superstructure and substructure stiffness, to classify the inelastic displacement patterns of multi-span continuous bridges into three patterns as rigid body translation, rigid body translation with rotation, and flexible pattern.

In 2007, Priestley et al. [1] presented a detailed study covering several displacement-based seismic design approaches of different types of structures including bridges. The study provided an extended design method similar to that presented by [38]. Moreover, it extended the direct displacement-based seismic design approach for various substructure-superstructure connections such as hinged, monolithic, and moveable bearing in both longitudinal and transverse directions.

Research efforts [39]–[41] addressed several aspects of displacement-based seismic design of bridges such as soil-structure interaction of bents supported by drilled shafts, effects of contraction and expansion joints on displacement patterns, and *P-Δ* effects on stability-based displacements of bridge piers.

As an alternative design approach, Bardakis & Fardis [42] proposed a multi-step design procedure for RC continuous bridges of monolithic pier-deck connection. According to [42], the procedure starts by estimating the effective stiffness of piers and deck based on idealized moment-curvature relationships obtained by performing sectional analyses for the considered elements. To simplify the implementation of the procedure, a set of expressions along with empirical equations are suggested to estimate the effective secant stiffness of piers at initial design iterations [43]. Using the effective stiffness of members, the inelastic displacement demands in both horizontal directions are estimated through modal response spectrum analyses performed with respect to 5%-damped design elastic spectrum. The flexural strength of piers is determined based on target chord rotation at yield obtained by employing modification factors considering ‘’equal displacement’’, whereas non-yielding behavior of deck is guaranteed. Indeed, shear failure of members and pier-deck connections is prevented using the capacity-design principle. Finally, the procedure is repeatedly iterated until the calculated secant effective stiffness values are consistent with the sections' geometry and detailing.

Although the existing performance-based design procedures have recognized advantages over the conventional design methods used in engineering practice, their capability of being incorporated into design codes is still under critical investigation.

Generally, the main reason for not having a comprehensive performance-based design method is that design procedures based on either linear or nonlinear analysis approaches require prior knowledge of structural element properties (e.g. geometry, longitudinal, and transverse reinforcements), which are considered as outputs of the design process itself. Moreover, other problems inherently associated with assumptions and approaches adopted in some design procedures restrict their applicability to a narrow bridge configuration. Design procedures such as those introduced by Priestley et al. [1] and Bardakis & Fardis [42] are limited to regular bridges in which the seismic response of structures could be estimated using equivalent SDOF systems and equal displacement rule, respectively [44]. Considering several direct displacement-based design procedures available in literature, various inherent problems are addressed in a review presented by Kappos et al. [45].

In addition to the aforesaid problems, the existing performance-based design procedures lack the ability to provide reliable levels of confidence in terms of achieving the targeted performance levels. Thus, the final design of structures is verified by complex nonlinear static or dynamic structural analyses resulting in huge computational efforts. Consequently, the need for such assessment analyses represents a violation to the simplicity requirements and reduces the differences between performance-based design procedures and the traditional design procedures adopted by current design codes.

Recently, seismic design codes such as CSA [46], NZT [47], and TKDY [48] have included the philosophy of performance-based design in the seismic design of bridge structures. However, the inclusion of performance-based design in these design codes is not associated with new design procedures but is limited to defining performance objectives, and deformation limit states only.

CHAPTER 3

PARAMETERS CONSIDERED IN THIS THESIS

3.1 Introduction

In this chapter, the design parameters anticipated to affect the R-factor of bridge structures are presented. To reduce the number of parameters, some of these parameters are expressed in dimensionless forms. Then, based on author's structural knowledge and practical design experience, the possible ranges of the considered parameters are investigated and determined in accordance with design limits specified in seismic design standards such as AASHTO [6] and Eurocode [7].

3.2 Selection of Ground Motions and Design Spectra

In this section, the selection and grouping procedures of the ground motions used in this research study are introduced. It should be mentioned that the ground motions used in this study are the same ground motions used in the study presented by Dicleli & Görgülü [49].

First, a set of 110 FFGM of different soil types is acquired from the PEER [10] database. Then, the selected ground motions are grouped according to their PGA/PGV ratios into ten groups each of 11 ground motions. These ground motions are selected carefully to represent different soil types as A, B, C, and D.

As the average spectrum of each group is used in both the RSA and NTHA, the 5%-damped response spectra of the ground motions are obtained. Next, the average spectra for each group of the selected ground motions are plotted, and their smoothed spectra are obtained by conducting nonlinear minimum least square regression analyses.

The obtained smoothed spectra are related to the average PGA/PGV ratios within each group and used as design spectra in the NTHA and RSA procedures.

3.2.1 Grouping of the Selected Ground Motions

Among several methods of grouping far-fault ground motions (soil type, magnitude, fault type, rupture distance, PGA/PGV ratio etc.), two methods are often used. The first one is classifying ground motions according to their site soil type considering similar spectral shapes within each set of ground motions. The other method is grouping far-fault ground motions according to their PGA/PGV ratio. In the seismic design of structures, a set of ground motions is selected and matched to the design spectrum to perform nonlinear time history analyses.

In selecting ground motions, particular attention is paid to important characteristics such as site soil type, fault type, distance to fault, and earthquake magnitude to obtain ground motions compatible with various site conditions.

Although the PGA/PGV ratio significantly affects the spectral shape of ground motions and hence, the seismic response of structures [26], [50], it is not considered one of the characteristics by which FFGM are grouped in practice as only the design spectrum is available. However, both soil type and PGA/PGV ratio are considered in grouping ground motions in this study. To tackle the unavailability of PGA/PGV ratio in engineering practice, the equation presented in [49] to correlate the PGA/PGV ratio with the second corner period of the design response spectrum is used.

A suite of 110 FFGM is considered in this research study. The ground motions are selected for various site conditions representing several soil classifications such as A, B, C, and D. Because of the lack of records representing ground motions of A and B soil types, only 10 ground motions are used for A&B soil types, where 52 and 48 ground motions are used representing C and D soil types, respectively. E and F soil

types are not considered in the scope of this research study as limited FFGM data are found for these types of soil.

Next, the selected FFGM are grouped according to their PGA/PGV ratio into 10 sets each of 11 ground motions. By sorting the ground motions with respect to their PGA/PGV ratio, it is found that ground motions having close PGA/PGV ratios indicate similar spectral shapes, which facilitates the matching procedures of the ground motions within each group to the design response spectrum and as a result, suitable scale factors are used for each ground motion.

To avoid near fault effect and pulse likewise ground motions, the ground motions are selected with distance to fault of more than 20 Km to represent far-fault properties. Moreover, the fault mechanisms considered in the selection of FFGM are normal and strike-slip fault mechanisms. A brief description of the obtained ground motions groups is summarized in Table 3.1. Further details of the used ground motions are available in appendix A.

Table 3.1 Ground motion groups summary

Group #	Soil Type	Min. PGA/PGV (1/s)	Max. PGA/PGV (1/s)	Average PGA/PGV (1/s)
1	D	4.9	5.6	5.2
2	D	5.8	6.9	6.5
3	D	7.0	7.8	7.5
4	D	7.9	8.9	8.6
5	C&D	9.1	10.2	9.6
6	C	10.2	10.8	10.5
7	C	10.8	11.6	11.2
8	C	12.0	13.5	12.8
9	C	13.5	15.0	14.2
10	A&B&C	15.4	42.2	27.2

3.2.2 Averaged and Smoothed Spectra

From many scaling procedures that have already been studied, several scaling approaches for FFGM have been proposed [51]. However, according to the current scaling procedures used in the seismic design of structures based on design codes, the acceleration-based scaling methods are still in use. Hence, the acceleration-based scaling procedure is used in this research study to scale the FFGM. Correspondingly, the ground motions within each group of the FFGM suite are scaled to the same intensity (PGA), and their average response spectra are obtained. Next, the smoothed average spectrum for each group is fitted by conducting nonlinear minimum least square regression analyses (MLSRA) on the average response spectrum.

The obtained smoothed average spectrum from each group is used in the RSA as a design spectrum. The smoothed average spectrum is adjusted to be similar in shape to the design response spectrum used in the seismic design of structures. It is composed of three spectral ranges: (1) the acceleration-sensitive range (ascending), (2) the velocity-sensitive range (constant), and (3) the displacement-sensitive range (descending).

To obtain the smoothed average spectrum, the starting points of the constant and descending parts are carefully determined from the average spectrum. These starting points represent the first and the second corner periods of the smoothed spectrum, respectively. Then, a minimum least square function is fitted between the second corner period point and the end period point of the average spectrum at 5 s. A spectral acceleration equation for the descending part is obtained as follows:

$$S_a = \frac{c}{T^{\alpha}} \tag{18}$$

where S_a is the spectral acceleration calculated as a function of the natural period (T) in the displacement sensitive range, c & α are coefficients determined by MLSRA. Next, the velocity-sensitive constant part of the smoothed spectrum is obtained by calculating the weighted average of the spectral acceleration with respect to the period range between the two corner periods as follows:

$$S_a = \frac{\sum S_{ai}\, \Delta T_i}{\sum \Delta T_i} \tag{19}$$

where S_{ai} is the discreet spectral acceleration corresponding to point i of which ΔT_i is the arbitrary period slot within the considered period range. The acceleration-sensitive ascending part of the smoothed spectrum is obtained by fitting linear function to the average response spectrum within the period range starting from 0 s to the first corner period. As a result, a linear equation is obtained as follows:

$$S_a = PGA + fT \tag{20}$$

where PGA is the peak ground acceleration and f is a coefficient representing the spectral acceleration slope in the considered period range. Accordingly, the smoothed spectrum for each group of ground motions is obtained and plotted as shown in Fig. 3.1.

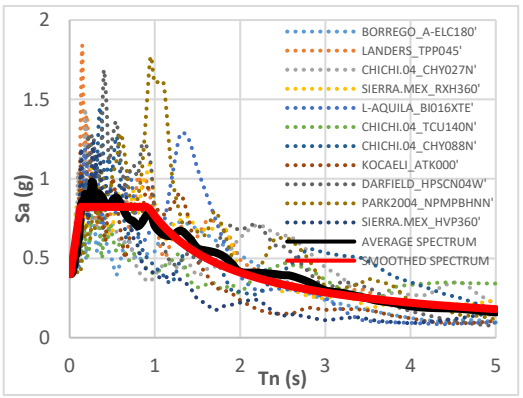

(a)

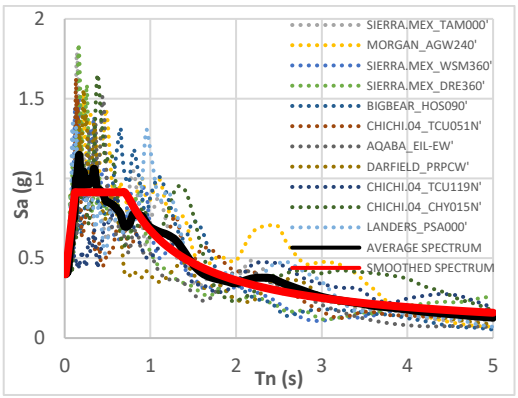

(b)

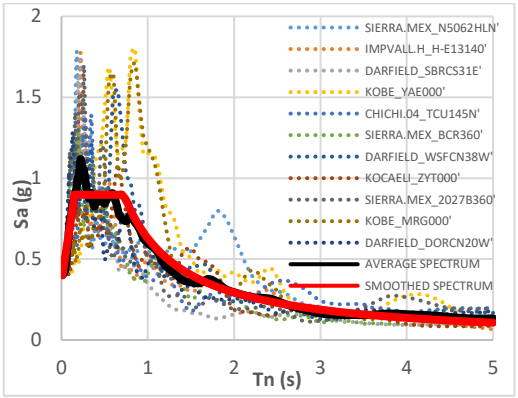

(c)

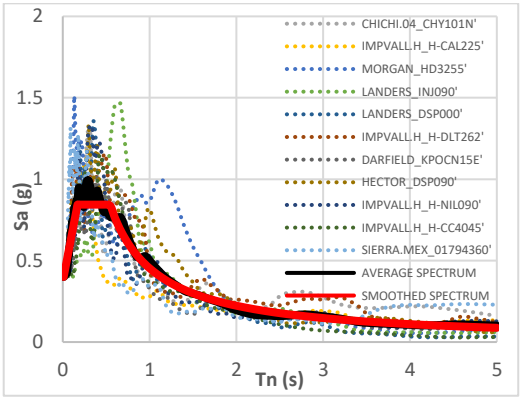

(d)

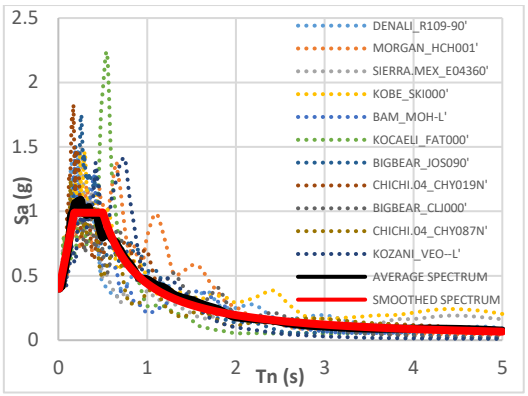

(e)

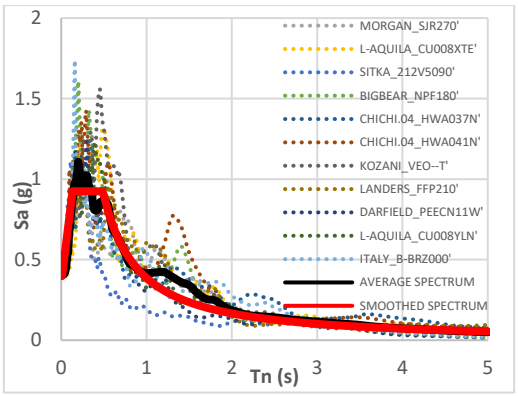

(f)

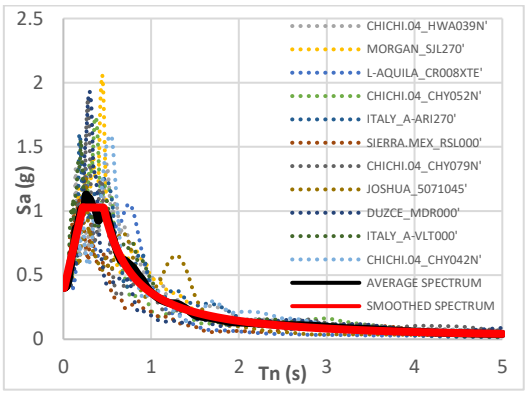

(g)

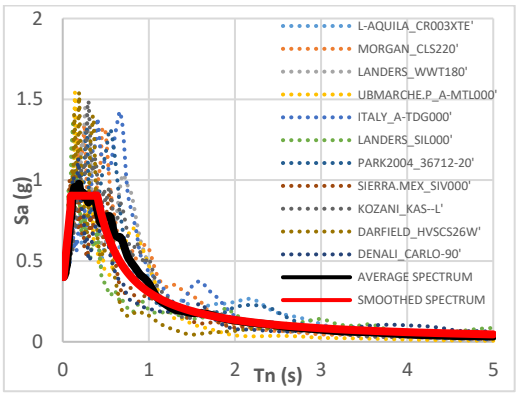

(h)

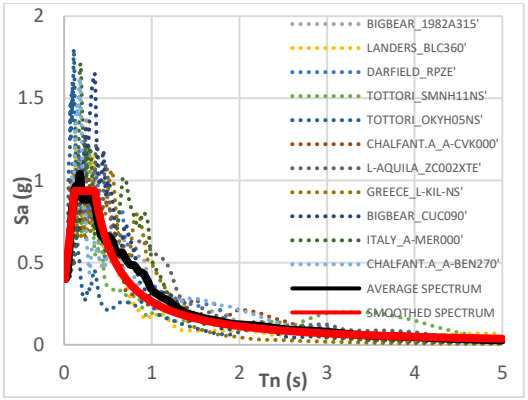

(i)

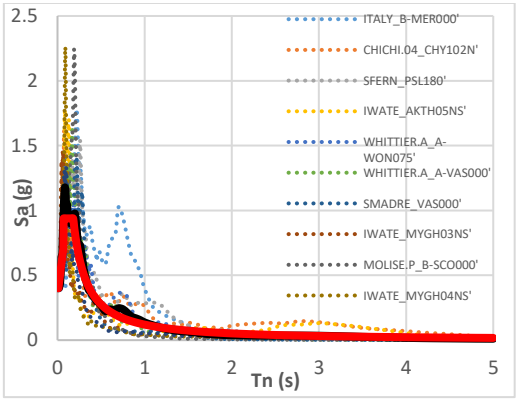

(j)

Figure 3.1. Average response spectra of ground motion groups, their smoothed average spectra. (a) - (j) represent group 1-10, respectively.

As the obtained smoothed response spectra are used in the RSA, they are considered as a design parameter representing the site seismic properties of soil and PGA/PGV ratio. To make this parameter more practical, additional study is conducted to relate the average PGA/PGV ratio to the second corner period (T_c) of the design response spectrum. The obtained second corner periods of the smoothed spectra are plotted versus the PGA/PGV ratios corresponding to each group of ground motions, as shown in Fig. 3.2.

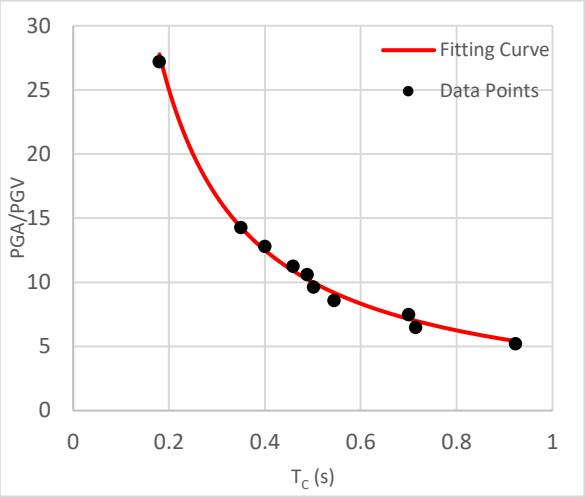

Figure 3.2. The second corner periods T_C of the smoothed response spectra versus the average PGA/PGV ratios of the ground motions groups, fitting curve of the plotted points.

The same equation of T_c presented in [49] is obtained by fitting a power function to the plotted points representing the relationship between T_c and the PGA/PGV ratio.

$$T_c = 5 \cdot \left(\frac{PGA}{PGV}\right)^{-1} \tag{21}$$

3.3 Design Parameters Affecting R-factor and Their Ranges

The strength reduction factor of the SDOF systems representing piers of bridges is affected by many parameters. The parameters considered in this research study are anticipated to have a significant impact on the seismic behavior of bridges and hence, the strength reduction factor, which is basically the force ratio of the elastic seismic demand to the plastic capacity of structures. These parameters are peak ground acceleration, natural period, corner period, the aspect ratio of pier, axial load, longitudinal reinforcements, transverse reinforcements, bearing stiffness, and concrete characteristic strength. The considered parameters are used in the RSA and NTHA procedures for various ranges determined by examining the design limits for each parameter in accordance with design codes. For simplicity, most of the parameters are combined and expressed in dimensionless forms, and their ranges are specified accordingly.

3.3.1 Pier's Aspect Ratio

The aspect ratio of pier (*H/D, H/h*) is considered as a dimensionless parameter in which the height of pier (*H*) to the section depth ratio of both circular and rectangular piers is used. For circular piers, by investigating the possible circular diameters in practice, the considered diameter (*D*) range varies between 1 and 2.8 m with an increment of 0.2 m. Similarly, the section depth (*h*) range of rectangular piers is taken between 1 and 2.4 m with an increment of 0.2 m.

However, for rectangular piers, an additional parameter is included to account for section width. It is defined as the section width to depth ratio (*b/h*), which is considered to vary between 1 and 2.

The minimum height of piers considered in this study is 6 m, where the maximum height is calculated for each section depending on their substructure-superstructure connection type to meet the slenderness ratio limits defined by AASHTO [6] as:

$$\frac{K\ H_{max}}{r} < 100 \tag{22}$$

where *K* is the effective length factor specified in table 3.2, H_{max} is the maximum height of pier, and r is the radius of gyration calculated depending on section type of pier as:

$$r = \left(\frac{I}{A_g}\right)^{0.5} \tag{23}$$

where I is the moment of inertia calculated about the weak axis for rectangular sections, and A_g is the gross section area of pier.

Table 3.2 Effective length factor

End support type	Fixed-pinned	Fixed-rotationally fixed
Buckled shape of pier		
Design value of K	2.1	1.2

Table 3.3 Aspect ratio limits for piers of circular sections

D (m)	Min(H/D)	Max(H/D)	Max(H/D)
1.0	6.0	11.0	20.0
1.2	5.0	11.7	20.8
1.4	4.3	11.4	20.7
1.6	3.8	11.9	20.6
1.8	3.3	11.7	20.6
2.0	3.0	11.5	20.5
2.2	2.7	11.8	20.5
2.4	2.5	11.7	20.8
2.6	2.3	11.5	20.8
2.8	2.1	11.8	20.7
Tip connection type		Pinned tip	Rotationally fixed tip

Table 3.4 Aspect ratio limits for piers of rectangular sections

h (m)	Min(H/D)	Max(H/D)	Max(H/D)
1.0	6.0	13.0	24.0
1.2	5.0	13.3	23.3
1.4	4.3	13.6	23.6
1.6	3.8	13.1	23.8
1.8	3.3	13.3	23.9
2.0	3.0	13.5	24.0
2.2	2.7	13.6	23.6
2.4	2.5	13.3	23.8
Tip connection type		Pinned tip	Rotationally fixed tip

Accordingly, the upper limits of the pier aspect ratio (*H/D, H/h*) are taken as (11,13) and (20,23) for pinned/elastomeric bearing connected and rotationally fixed tip piers, respectively.

3.3.2 Axial Load

The axial load is included in this study in a dimensionless form. The axial load on a pier is expressed by the axial load ratio (η), which is the ratio of the axial load (P) to the section ultimate axial load capacity.

$$\eta = \frac{P}{0.85\, f_c\, A_g\, (1-\rho_l) + f_{sy}\, \rho_l\, A_g} \tag{24}$$

The range of the axial load ratio (η) considered in this study varies between 0.07 and 0.20 (5 different values: 0.07, 0.10, 0.13, 0.16, 0.20).

3.3.3 Longitudinal Reinforcements

The ratio of the total longitudinal reinforcement area to the section gross area (ρ_l) is also considered as a parameter varying within the limits defined by AASHTO [6] from 0.01 to 0.04 (7 different values: 0.01, 0.015, 0.02, 0.025, 0.03, 0.035, and 0.04).

3.3.4 Transverse Reinforcements

Likewise, the volumetric ratio of transverse reinforcements (ρ_t) is included as a design parameter in this study. Its ranges is specified to vary between 0.003 and 0.015 by an increment of 0.002 (7 different values: 0.003, 0.005, 0.007, 0.009, 0.011, 0.013, and 0.015).

3.3.5 Characteristic Strength of Concrete

In this research study, the characteristic strength of concrete (f_c) is varied with 4 different values as 20, 30, 40, and 50 MPa.

3.3.6 Natural Period of Bridge

The natural period of bridge structure (T_n) is anticipated to be an important parameter affecting R-factor. However, the range of (T_n) is determined by varying the lateral dynamic mass ($mass_{dynamic}$) of piers between 0.5 and 1.5 of the axial rigid mass of pier (5 different values: 0.5, 0.75, 1, 1.25, 1.5), where the axial mass is calculated as:

$$mass_{axial} = \frac{0.85\, f_c\, A_g\, (1-\rho_l) + f_{sy}\, \rho_l\, A_g}{g}\eta - \rho_c A_g \frac{H}{2} \quad (25)$$

where $mass_{axial}$ is the arbitrary axial rigid mass of pier, A_g is the section gross area, f_{sy} is the longitudinal steel characteristic strength (420 MPa in this study), g is the gravitational acceleration, and ρ_c is the volumetric density of reinforced concrete.

Based on author's practical experience, and to obtain realistic natural period values, (T_n) is limited in this study between 0.2 (s) and 3 (s). The natural period is calculated for SDOF systems as following.

$$T_n = 2\pi \sqrt{\frac{mass_{dynamic}}{K_{pier}}} \quad (26)$$

where K_{pier} is the effective stiffness of pier corresponding to the cracked section.

3.3.7 Bearing Stiffness Ratio

For piers with elastomeric bearings, additional parameter is considered representing the lateral stiffness ratio of bearings to the effective pier stiffness (K_{reff}) that varies

between 0.05 and 0.80 (8 different values: 0.05, 0.10, 0.15, 0.20, 0.35, 0.50, 0.65, and 0.80).

$$K_{reff} = \frac{K_h}{K_{pier}} \quad (27)$$

where K_h is the lateral stiffness of elastomeric bearing.

3.3.8 Second Corner Period of the Design Spectrum

The second corner period of the design spectrum (T_c), which is a function of the *PGA/PGV* ratio, is also included in this study. To clarify the significance of the corner period of the design spectrum on the strength reduction factor, it is decided to perform the analyses in this study for only five different corner period values as (0.18 ,0.40, 0.50, 0.70, and 0.90 s) representing (10, 8, 5, 3, and 1) ground motions groups, respectively.

3.3.9 Peak Ground Acceleration

The peak ground acceleration PGA which illustrates the seismic intensity of ground motions is included in this study and varied between 0.2 (g) – 1.2 (g), 6 different values: 0.2 (g), 0.4 (g), 0.6 (g), 0.8 (g), 1.0 (g), 1.2 (g).

CHAPTER 4

SECTIONAL ANALYSES OF BRIDGE PIERS

4.1 Introduction

In this chapter, the sectional analyses performed for bridge piers are introduced. Based on the sectional parameters considered in this study, the RC sections of piers are modeled, and the corresponding moment-curvature relationships are obtained. For each section, the obtained moment-curvature relationship is idealized by fitting a trilinear least square function representing the nonlinear behavior of piers. Moreover, the effects of various sectional parameters on the effective yield curvature, the ultimate curvature, and the yield moment capacities of both circular and rectangular sections are investigated. Consequently, a set of equations to estimate the yield curvature, ultimate curvature, and the yield moment capacities of pier sections is proposed by performing parametric linear regression analyses on the obtained results.

4.2 Definitions of Yield and Ultimate Curvatures

Due to the nonlinear behavior of reinforced concrete, which results in a nonlinear moment-curvature relationship, different definitions of yield curvature have been suggested by various research studies. As described in Fig. 4.1, the section response starts with a linear moment-curvature relationship proceeded by nonlinear behavior ensued from the softening of concrete and yield of reinforcing steel. Park and Paulay [52] defined yield curvature as the minimum curvature corresponding to either the first yield of steel or concrete reaching a strain of 0.002.

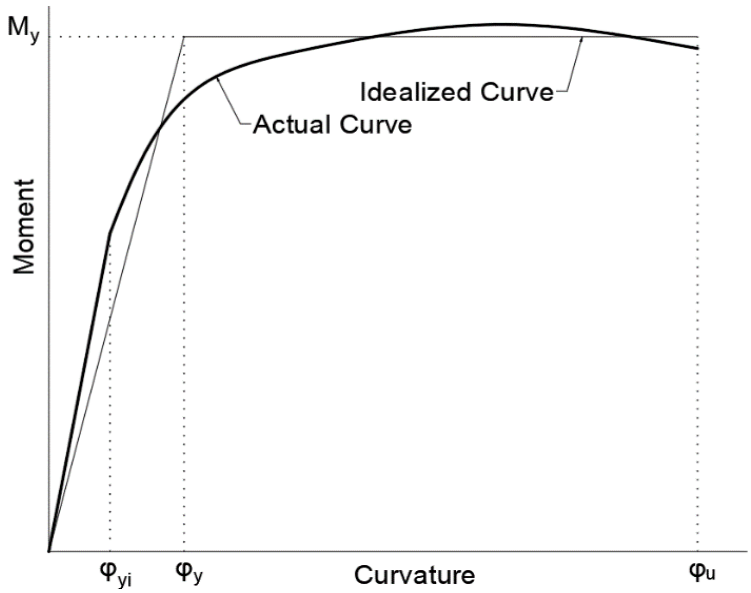

Figure 4.1. Actual versus idealized monolithic moment-curvature relationship.

For design purpose, the effective yield curvature is used rather than the initial yield curvature. The effective yield curvature is obtained by idealizing the actual moment-curvature curve into a bilinear relationship, as shown in Fig.4.1. The idealized moment-curvature curve consists of two parts representing the elastoplastic behavior of reinforced concrete sections. Moreover, the first part of the idealized moment-curvature curve is considered as the elastic range of effective flexural stiffness corresponding to the cracked section. The second part represents the plastic response of the RC column section. Priestley et al. [53] defined the effective yield curvature as the curvature corresponding to the intersection of the line from origin passing through the initial yield point with the tangent line of flexural strength capacity. However, this approach might result in inaccurate effective yield curvature estimation as many tangent lines of flexural strength capacity could be drawn.

In their study, Sheikh et al. [15] adopted a different approach in estimating the effective yield curvature. Such an approach that is based on both the initial yield point and the ultimate flexural strength capacity M_{max} of column as follows:

$$\varphi_y = min(\varphi_{yc}\frac{M_{max}}{M_{yc}}, \varphi_{ys}\frac{M_{max}}{M_{ys}}) \quad (28)$$

where φ_{yc} is the curvature at which the peak strain of concrete is reached, and φ_{ys} is the curvature corresponding to the first yield of reinforcing steel. In this study, the estimation of yield curvature is based on fitting a minimum least square multilinear function of the idealized moment-curvature curve, which is described in detail in the following sections.

Regarding the ultimate curvature, various analytical and experimental studies on the deformation capacity of columns attributed the flexural failure of columns to the fracture of reinforcing steel or/and concrete reaching its ultimate strain capacity ε_{cu} [54]–[57]. Hence, the ultimate deformation capacity of columns is defined in terms of material strains. Based on ultimate strains of concrete and reinforcing steel, Priestley et al. [1] defined the ultimate curvature of reinforced concrete sections as the curvature at which 60% of the ultimate steel strain ($0.6\varepsilon_{su}$) or the ultimate strain of confined concrete is reached. Accordingly, the ultimate curvature adopted in this study is based on the definition suggested by [13].

4.3 Modeling of Flexural Behavior of RC Sections

The flexural response of RC sections is inherently nonlinear. Such nonlinearities ensued from the combined nonlinear behavior of both concrete and steel under monotonic or cyclic loading. Thus, appropriate nonlinear material models are needed to be used in analytical sectional analysis to obtain proper moment-curvature response simulating the actual behavior of RC piers. In this research study, the analytical moment-curvature relationship for an RC section is obtained by performing sectional analysis considering appropriate material models of both concrete and steel. For this purpose, a moment-curvature program is developed via OpenSees [12] based on fiber section modeling of RC sections of columns. The modeled fiber section consists of a confined reinforced concrete core surrounded by

a concrete cover of constant depth. Results obtained by Sheikh et al. [15] showed insignificant effect of the depth of the concrete cover on the yield curvature of columns. Hence, the depth of concrete cover is considered constant as 0.05 m in this study. The properties of the material models used in this study are described in the following subsections:

4.3.1 Material Model of Concrete

The Mander [13] stress-strain model is used to simulate the response of confined concrete under uniaxial compressive loading. The model accounts for several confinement types for both circular and rectangular sections including spiral, hoops, and cross ties. It predicts the compressive strain of confined concrete based on balancing the strain energy capacity corresponding to the first fracture of transverse reinforcements with the strain energy stored in confined concrete due to the effective lateral pressure of confinements. As shown in Fig. 5.2, the Mander model [13] is used for the confined concrete core, where unconfined concrete is used for modeling the concrete cover.

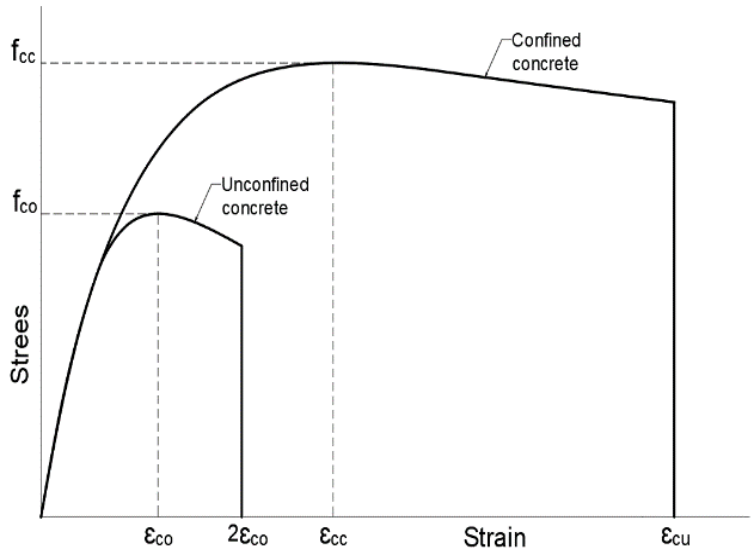

Figure 4.2. Stress-strain relationship of confined and unconfined concrete.

As could be noticed from Fig. 4.2., the stress values corresponding to ultimate strains of confined and unconfined concrete are dragged to zero to ensure a significant drop in the moment at the ultimate curvature of sections. The ultimate strain capacity of confined concrete is calculated based on the equation suggested by [13] as:

$$\varepsilon_{cu} = 0.004 + \frac{1.4\,\rho_s\,f_{yh}\,\varepsilon_{su}}{f_{cc}} \tag{29}$$

where $\rho_s\,is$ the transverse reinforcement ratio, f_{cc} is the peak strength of confined concrete, f_{yh} and ε_{su} are the yielding strength and ultimate strain of transverse steel, respectively.

4.3.2 Material Model of Steel

For simplicity, a classic idealized trilinear model is used in modeling the stress-strain relationship of the reinforcing steel under both tensile and compressive monotonic loading. As given in Fig. 4.3, the adopted model consists of three ranges accounting for the 1) elastic, 2) yielding, and 3) strain hardening behavior of the reinforcing steel. Firstly, the initial response of the reinforcing steel is assumed linear with elastic stiffness taken as 2×10^5 MPa. The second range of the idealized stress-strain relationship represents the yielding response of steel having constant yielding stress f_{sy} until the hardening strain ε_{sh}, then the strain hardening occurs till the ultimate strain capacity ε_{su} of steel is reached.

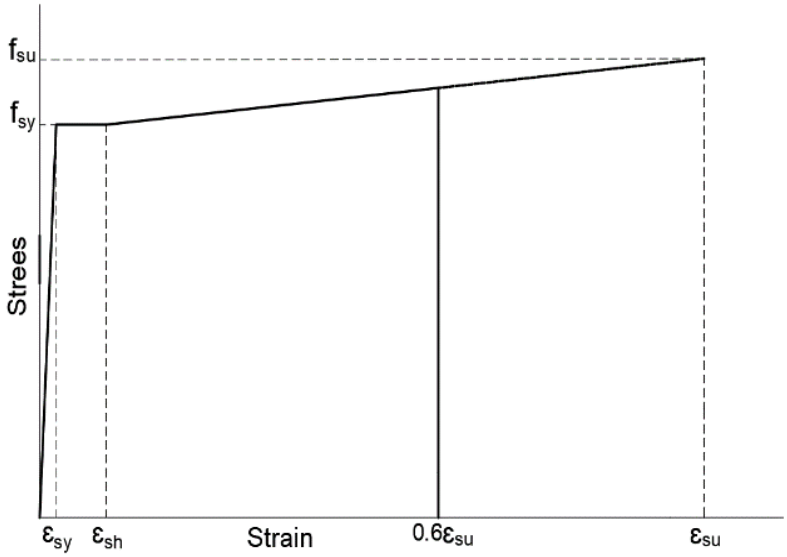

Figure 4.3. Stress-strain relationship of reinforcing steel.

Similar to the concrete model, the stress-strain relationship of steel is dragged to zero at the strain limit $0.6\varepsilon_{su}$ by which the ultimate curvature is defined.

4.4 Modeling of Flexural Behavior of RC Sections

As this research study focuses on the effective yield point rather than the initial yield point, the effective yield point is determined by idealizing the actual moment-curvature obtained from the sectional analysis. The idealized moment-curvature relationship is derived by dividing it into three parts. As described in Fig. 4.4, the first part of the idealized curve represents the elastic range. The second part is the hardening range, and the third part represents the softening range, where the flexural strength degrades due to the strain-softening in concrete and/or steel. The endpoints of these parts represent yielding, peak, and ultimate points, respectively.

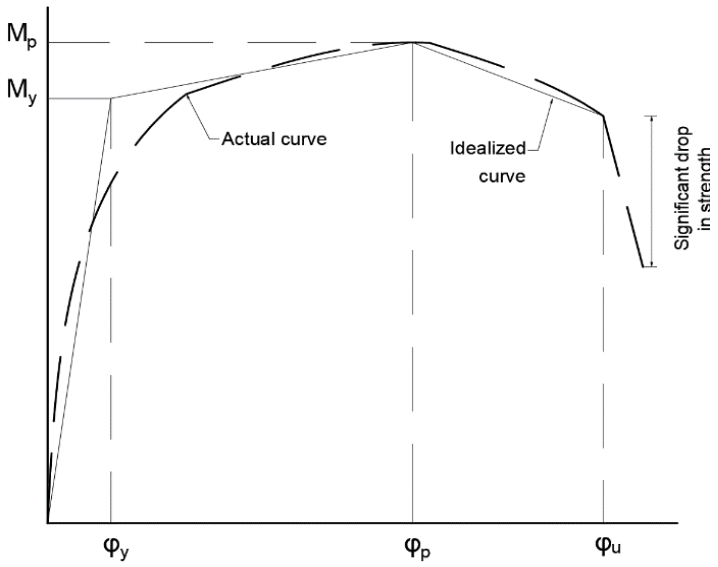

Figure 4.4. Actual versus idealized monotonic moment-curvature relationship

Firstly, the ultimate point is easily detected as a significant drop in flexural strength takes place based on the ultimate strain limits defined in the used material models. As it could be noticed from Fig. 4.4, the ultimate curvature is determined as the curvature value prior to the drop of strength. Next, the peak point is defined as the point corresponding to the maximum peak moment M_p. Then, the yield point is carefully examined as it represents the endpoint of the elastic range. Indeed, it corresponds to the yield curvature and the yield moment, which are important in the design of bridge structures. Hence, the yielding point is determined by fitting a trilinear minimum least square function to the actual curve followed by regression analysis as follows:

A linear function is fitted to the actual curve within the elastic range representing the elastic part of the idealized moment-curvature curve. The linear part has an equation as follows:

$$M = K_{cr}\,\varphi \tag{30}$$

where M is moment, and K_{cr} is the cracked section flexural stiffness illustrating the initial slope of the idealized curve corresponding to the curvature values φ within

the considered range. The second part of the idealized curve is obtained by fitting a linear function within the range between yielding and peak points. The equation of this function is as follows;

$$M = M_y + K_h (\varphi - \varphi_y) \quad (31)$$

where M_y is the yielding moment, K_h is the slope of the second part representing the hardening stiffness, and φ_y is the effective yield curvature. The yield moment M_y is calculated as the weighted average moment in the range between yielding and ultimate points.

$$M_y = \frac{\sum M_i \, \Delta\varphi_i}{\sum \Delta\varphi_i} \quad (32)$$

where M_i is the discreet moment value of the arbitrary curvature slot $\Delta\varphi_i$ within the considered range. Lastly, the softening part of the idealized curve is obtained by fitting a linear function between the peak and ultimate points as follows;

$$M = M_p + K_s (\varphi - \varphi_p) \quad (33)$$

where K_s is the slope of the softening part, illustrating the softening stiffness of the idealized curvature relationship, and φ_p is the peak curvature.

Accordingly, the trilinear idealized moment-curvature relationship is created, where the endpoint for each segment is obtained by conducting minimum least square regression analysis considering the areas under both actual and idealized curves.

4.5 Parametric Sectional Analyses

Sectional analyses have been performed considering the sectional parameters included in this study. Moreover, the variations of the effective yield curvature, ultimate curvature, and yield moment capacity of circular and rectangular sections are investigated on wide ranges of various sectional parameters. Accordingly, the

analytical sectional analyses are performed for 9800 circular sections and 33600 rectangular sections in both weak and strong axes.

4.5.1 Variation of the Effective Yield Curvature as A Function of Sectional Parameters

The effects of various sectional parameters on the effective yield curvature are investigated considering the specified ranges.

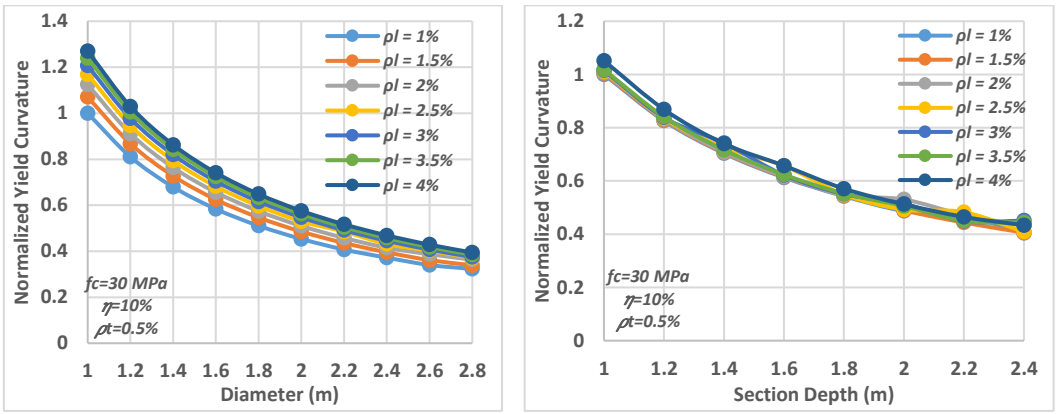

(a) (b)

Figure 4.5. Effects of section diameter/depth and longitudinal reinforcements on the normalized effective yield curvature. (a) Circular sections, (b) Rectangular sections.

In Fig. 4.5, the effect of the depth of section on the effective yield curvature for different longitudinal reinforcements ratios is described by normalizing the effective yield curvature values with the value corresponding to 1m section depth for both circular and rectangular sections. It could be noticed that the effective yield curvature decreases as the section depth increases for both section types. Moreover, Fig. 4.5 (a) shows a significant increase of the effective yield curvature due to the increase

of the amount of the longitudinal reinforcements for circular sections. On the other hand, a small effect of the longitudinal reinforcements is observed on the effective yield curvature of rectangular sections.

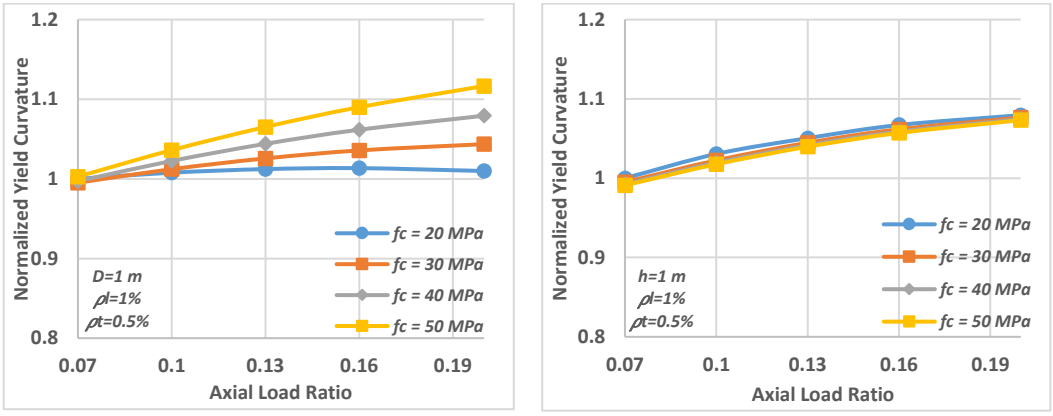

(a) (b)

Figure 4.6. Effects of axial load and characteristic strength of concrete on the normalized effective yield curvature. (a) Circular sections, (b) Rectangular sections.

Results shown in Fig. 4.6 indicate that the effective yield curvature significantly increases with higher axial load ratios. Indeed, it could be understood that the characteristic strength of concrete has significant influence on the effective yield curvature of circular sections, where it has very limited influence on the effective yield curvature of rectangular sections. The effective yield curvature values presented in Fig. 4.6 (a) and Fig. 4.6 (b) are normalized with respect to the values at 0.07 axial load ratio and 20 MPa concrete characteristic strength. It is noteworthy to mention that the amount of transverse reinforcements and section width showed no influence on the effective yield curvature.

4.5.2 Variation of Ultimate Curvature as A Function of Sectional Parameters

The effects of various sectional parameters on the ultimate curvature are investigated considering the specified ranges.

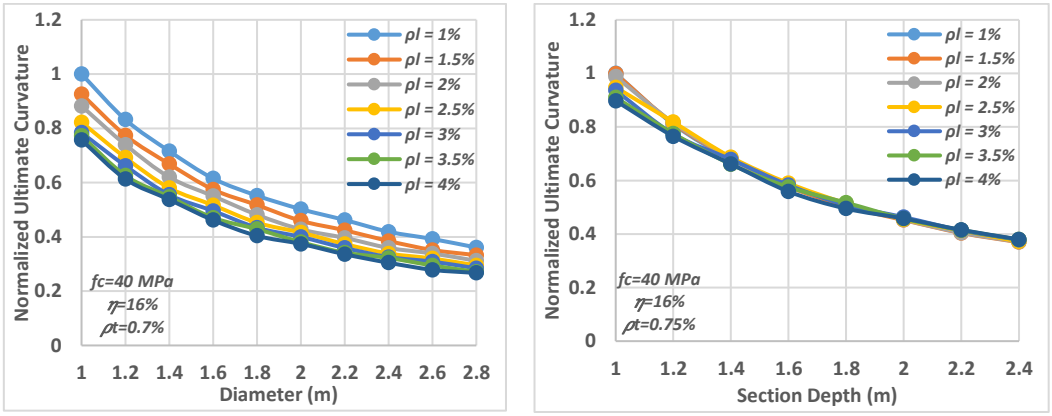

(a) (b)

Figure 4.7. Effects of section diameter/depth and longitudinal reinforcements on the normalized ultimate curvature. (a) Circular sections, (b) Rectangular sections.

The results show a significant influence of the section depth on the ultimate curvature capacity of column sections. As it could be concluded from Fig. 4.7, the ultimate curvature capacity decreases with higher section depth for both circular and rectangular sections. Regarding longitudinal reinforcements, the amount of longitudinal reinforcements appears to affect the ultimate curvature capacity of circular sections, where it has a negligible effect on the ultimate curvature capacity of rectangular sections.

From the results presented in Fig. 4.8, a significant effect of axial load ratio and characteristic strength of concrete could be observed on the ultimate curvature capacity of both circular and rectangular sections. It could be noticed that the

ultimate curvature decreases as axial load increases. Moreover, it decreases as the concrete characteristic strength increases.

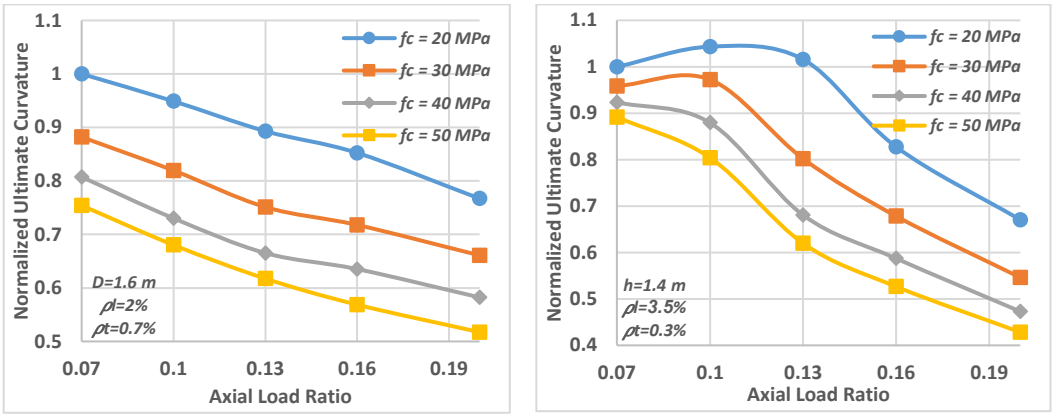

(a) (b)

Figure 4.8. Effects of axial load and characteristic strength of concrete on ultimate curvature. (a) Circular sections, (b) Rectangular sections.

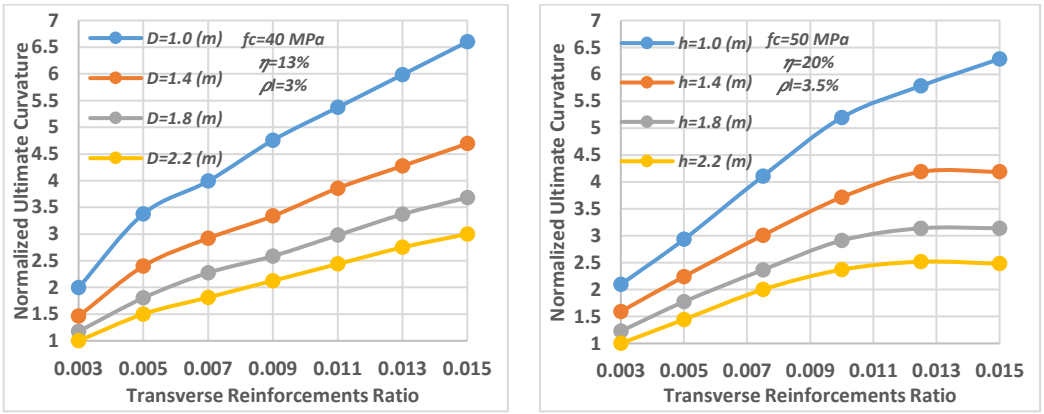

(a) (b)

Figure 4.9. Effects of transverse reinforcements on ultimate curvature. (a) Circular sections, (b) Rectangular sections.

As shown in Fig. 4.9, a significant increase in the ultimate curvature capacity of circular and rectangular sections is observed due to the increase of the transverse reinforcement ratio.

4.5.3 Variation of Yield Moment as A Function of Sectional Parameters

The effects of various sectional parameters on the yield moment capacity are investigated within the specified ranges.

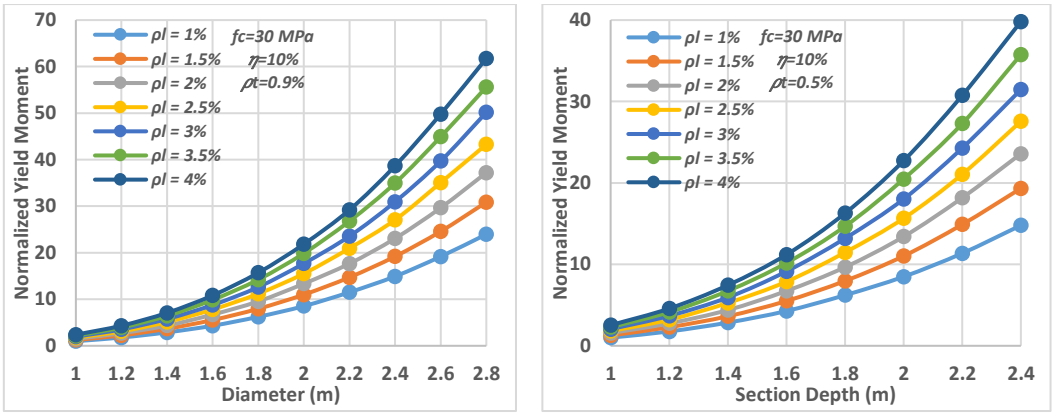

(a) (b)

Figure 4.10. Effects of section diameter/depth and longitudinal reinforcements on yield moment. (a) Circular sections, (b) Rectangular sections.

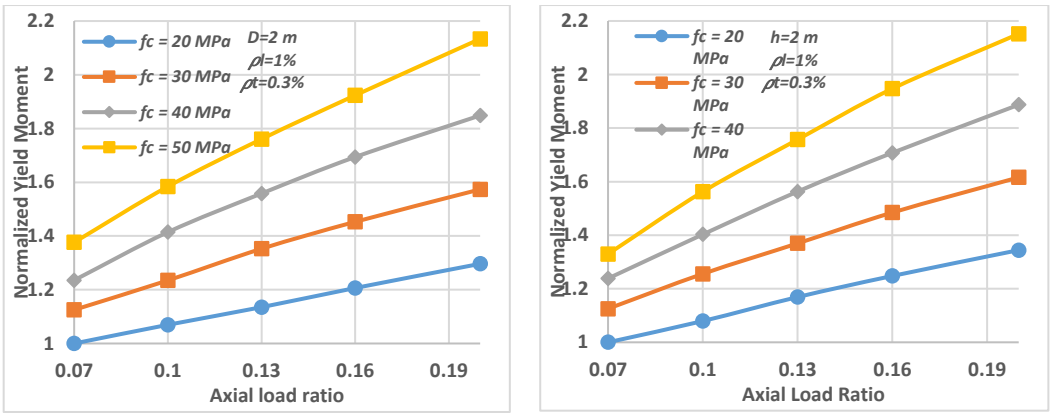

(a) (b)

Figure 4.11. Effects of axial load and characteristic strength of concrete on yield moment. (a) Circular sections, (b) Rectangular sections.

The results presented in Fig. 4.10 show a significant effect of both section depth and longitudinal reinforcements on the yield moment capacity of column sections. Indeed, the yield moment capacity tends to increase at higher axial load ratios within the range varying between 7% and 20% as described in Fig. 4.11. Moreover, yield moment capacity increases with higher characteristic strength of concrete.

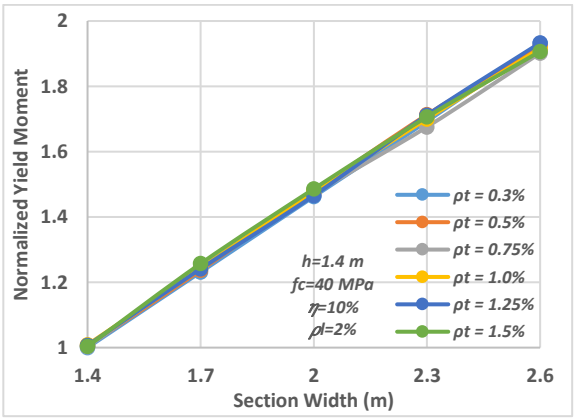

Figure 4.12. Section width versus normalized yield moment of rectangular sections for various transverse reinforcements ratios.

It could be noticed from Fig. 4.12 that the yield moment capacity of rectangular sections increases with higher section width. Indeed, results indicate no significant influence of transverse reinforcements on yield moment capacity for both circular and rectangular sections.

4.6 Data Analyses and Derivation of the Proposed Sectional Equations

In this section, six equations to estimate the effective yield curvature, ultimate curvature, and yield moment capacities for both circular and rectangular sections are presented. The derivation of these equations is achieved by performing parametric linear regression analyses on the data obtained from the conducted parametric sectional analyses. For simplicity, the proposed equations are decided to have power function shape expressed as a function of the considered parameters as following.

$$Y = C_0 \cdot {X_1}^{C_1} \cdot {X_2}^{C_2} \cdot \ldots . {X_n}^{C_n} \quad (34)$$

where Y is the estimated value, X_1, X_2, and X_n represent the considered sectional parameters, C_0, C_1, C_2, and C_n are coefficients determined via regression analysis. For this purpose, multiple linear regression analyses are performed after applying logarithmic transformation on the data to obtain the coefficients of the desired function shape.

The proposed effective yield curvature, ultimate curvature, and yield moment capacity equations for both circular and rectangular RC sections are introduced in the following subsections:

4.6.1 Proposed Effective Yield Curvature Equations

Two equations are proposed to estimate the effective yield curvature for both circular and rectangular sections.

- **For circular sections:**

$$\varphi_y = 0.0106 \cdot \frac{{\rho_l}^{0.16} \cdot \eta^{0.02}}{D^{1.1}} \tag{35}$$

To examine the accuracy of the above equation, a goodness of fit plot, representing the match of the estimated effective yield curvature values with 9800 calculated values obtained from the sectional analyses, is presented in Fig. 4.13. Moreover, the error distribution of the estimated data is introduced as shown in Fig. 4.14.

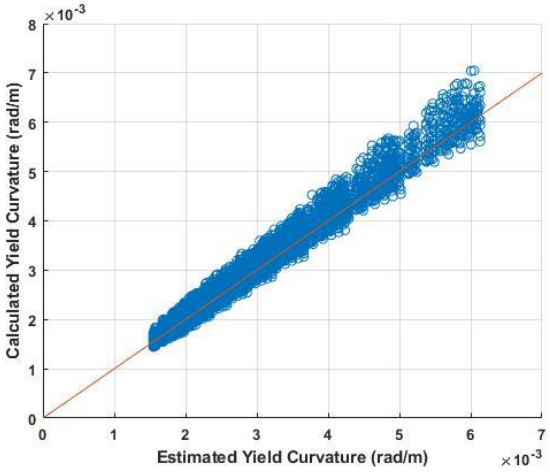

Figure 4.13. Effective yield curvature goodness of fit scatter plot for circular sections.

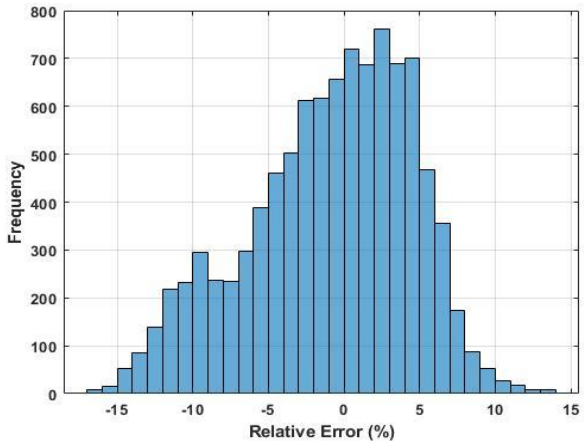

Figure 4.14. Relative error distribution of the estimated effective yield curvature values for circular sections.

As it could be noticed from Fig. 4.13, the proposed equation shows a very good fit of the estimated effective yield curvatures with R^2 value of 0.98. Indeed, the majority of the estimated values indicate very small errors compared to the calculated values.

- **For rectangular sections:**

$$\varphi_y = (6.5 \times 10^{-3}) \cdot \frac{{\rho_l}^{0.03} \cdot \eta^{0.05}}{h} \tag{36}$$

The goodness of fit scatter and the error distribution of the estimated yield curvature values using the above equation are presented in Fig. 4.15 and Fig. 5.16, respectively.

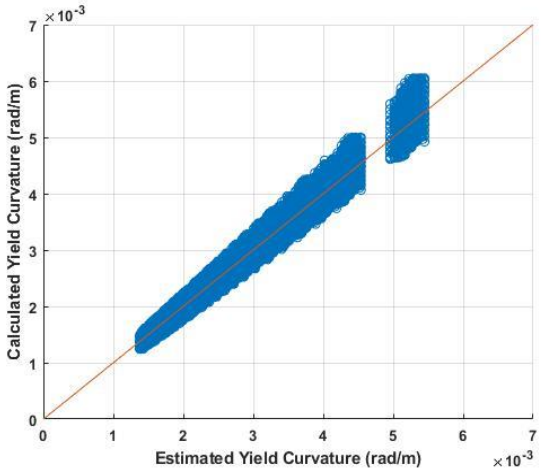

Figure 4.15. Effective yield curvature goodness of fit scatter plot for rectangular sections.

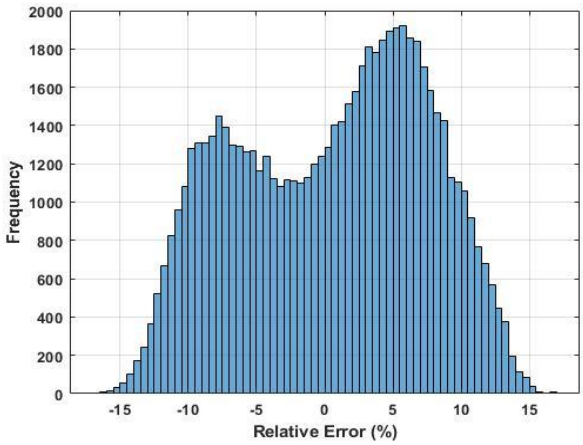

Figure 4.16. Relative error distribution of the estimated effective yield curvature values for rectangular sections.

The corresponding R^2 value of the above equation is 0.95.

4.6.2 Proposed Ultimate Curvature Equations

Two equations are proposed to estimate the ultimate curvature for both circular and rectangular sections.

- **For circular sections:**

$$\varphi_u = 0.26 \cdot \frac{{\rho_t}^{0.45}}{D \cdot {\rho_l}^{0.06} \cdot \eta^{0.27}} \tag{37}$$

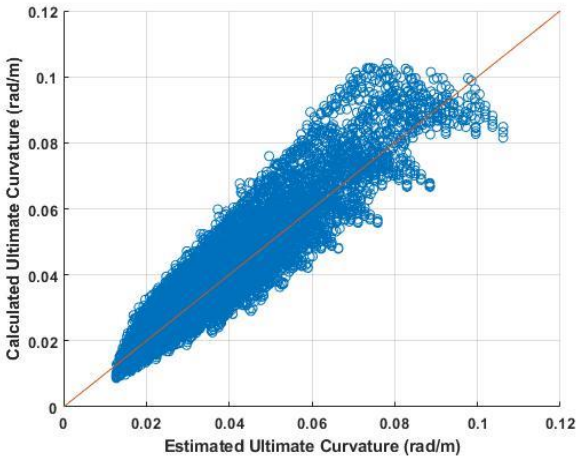

Figure 4.17. Ultimate curvature goodness of fit scatter plot for circular sections.

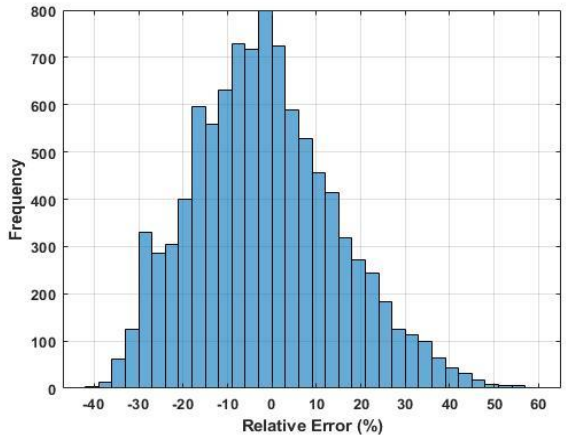

Figure 4.18. Relative error distribution of the estimated ultimate curvature values for circular sections.

The goodness of fit scatter along with the error distribution of the estimated ultimate curvature values using the above equation are presented in Fig. 4.17. and Fig. 4.18.

As it is illustrated in Fig. 4.17, the proposed equation provides a good estimation of the ultimate curvatures for the analyzed sections with R^2 value of 0.87. Moreover, From the error distribution plot, the errors of the estimated values have peak frequency oriented toward zero.

- **For rectangular sections:**

$$\varphi_u = 0.17 \cdot \frac{{\rho_t}^{0.16}}{h^{1.1} \cdot \eta^{0.03}} \tag{38}$$

The goodness of fit scatter and the error distribution of the estimated ultimate curvature values using the above equation are presented in Fig. 4.19. and Fig. 4.20.

The corresponding R^2 value of the above equation is 0.85.

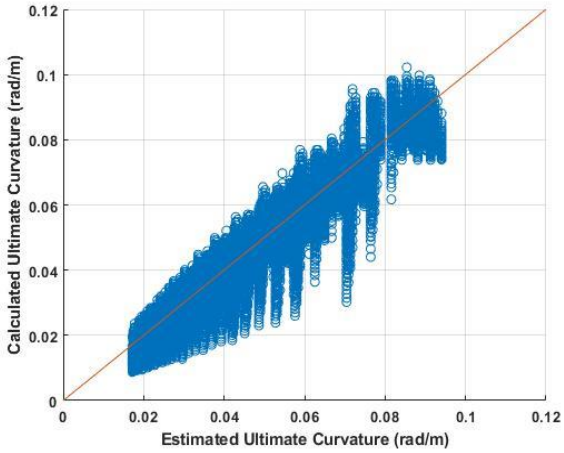

Figure 4.19. Ultimate curvature goodness of fit scatter plot for rectangular sections.

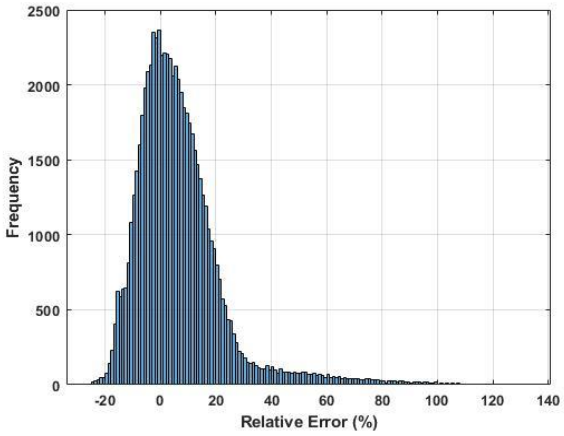

Figure 4.20. Relative error distribution of the estimated ultimate curvature values for rectangular sections.

4.6.3 Proposed Yield Moment Equations

Two equations are proposed to estimate the yield moment capacity for both circular and rectangular sections.

- **For circular sections:**

$$M_y = (2 \times 10^4) \cdot D^3 \cdot {f'_c}^{0.3} \cdot {\rho_l}^{0.6} \cdot \eta^{0.2} \quad (39)$$

where D is in *(m)*, f'_c is in *(MPa)* and M_y is in *(KN.m)*.

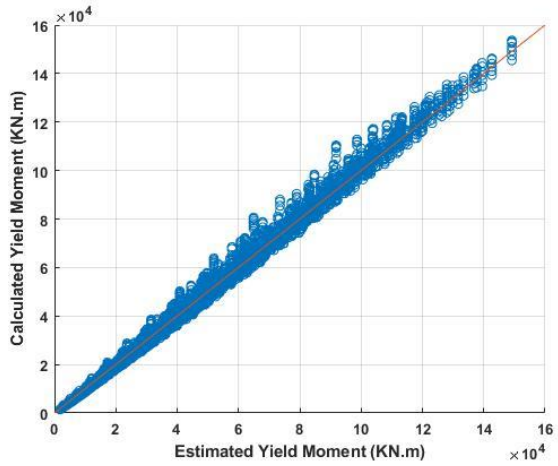

Figure 4.21. Yield moment capacity goodness of fit scatter plot for circular sections.

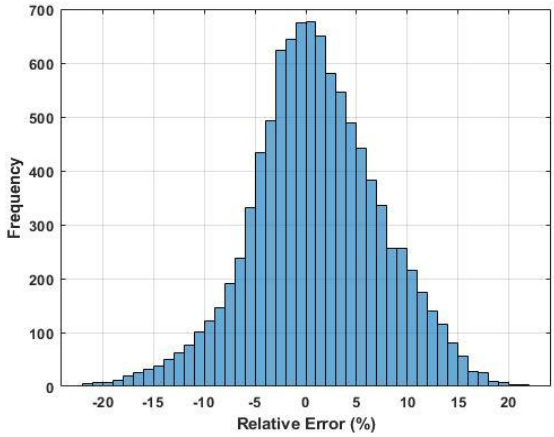

Figure 4.22. Relative error distribution of the estimated yield moment values for circular sections.

As illustrated in Fig. 4.21, perfect fit is achieved using the yield moment equation with R^2 equals 0.99.

- **For rectangular sections:**

$$M_y = (4.25 \times 10^4) \cdot h^2 \cdot b \cdot {f'_c}^{0.3} \cdot {\rho_l}^{0.7} \cdot \eta^{0.2} \quad (40)$$

where h & b are in *(m)*, f'_c is in *(MPa)* and M_y is in *(KN.m)*.

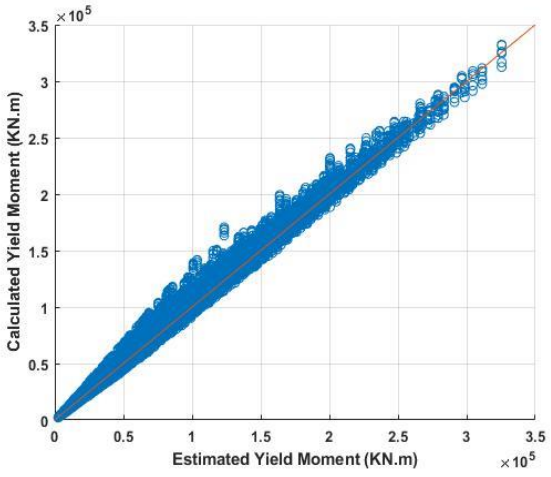

Figure 4.23. Yield moment capacity goodness of fit scatter plot for rectangular sections.

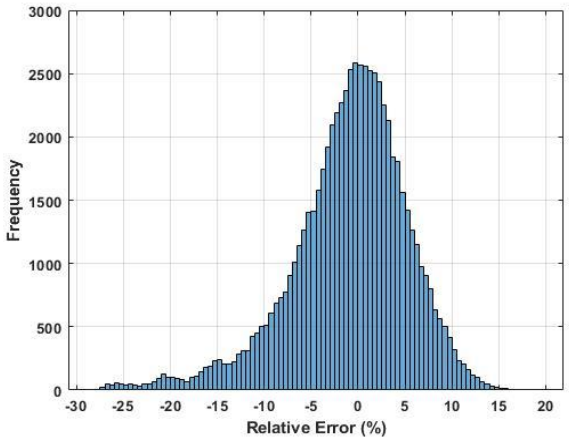

Figure 4.24. Relative error distribution of the estimated yield moment values for rectangular sections.

The corresponding R^2 value of the above equation is 0.98.

CHAPTER 5

STRENGTH REDUCTION FACTORS OF BRIDGE PIERS

5.1 Introduction

In this chapter, the structural modeling of piers as SDOF systems is thoroughly explained. Moreover, the strength reduction factors are derived by performing parametric RSA and NTHA procedures of the SDOF systems considering the selected FFGM. The parametric analyses are conducted for an extensive range of various design parameters including the peak ground acceleration (*PGA*), natural period (T_n), aspect ratio of pier (*H/D*), axial load ratio (η), bearing lateral stiffness (K_h), longitudinal reinforcement ratio (ρ_l), and concrete characteristic strength (f_c). In the NTHA, lumped plasticity method is used through plastic hinges defined by backbone curves obtained by conducting sectional analyses for piers. The hysteretic model used in the NTHA is adjusted to account for different failure modes as shear, shear-flexure combined, and flexure failure depending on some design parameters of piers.

5.2 Bridge Piers as SDOF Systems

In performance-based seismic design, Bridge structures are supposed to resist seismic forces within definite damage limits specified by design codes. According to the current design codes, the damage limits by which seismic performance levels are defined, are expressed by tip displacement of elements. Moreover, it is recommended by design codes to design bridges such that damages occur in piers rather than other elements such as abutments, deck, footings, and cap beams which are preferred to remain elastic during seismic actions [42]. Hence, the seismic

behavior of piers is regarded as a pivoting point of the strength reduction factor evaluation.

In this research study, piers are modeled as SDOF systems with lumped mass representing the corresponding arbitrary dynamic mass of superstructure. Indeed, three types of SDOF systems are created according to their substructure-superstructure connection type with fixed base supports, as shown in Fig.5.1.

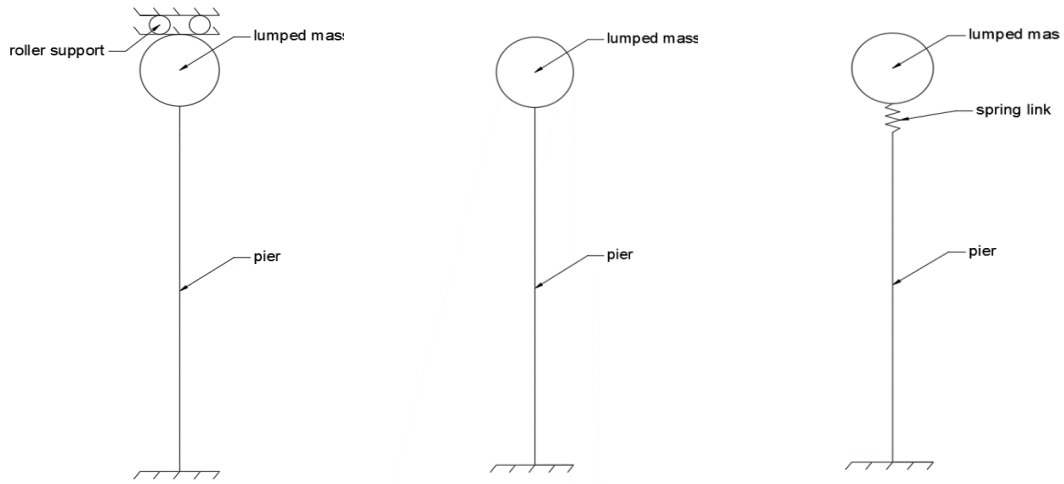

Monolithically-connected pier system

(a)

Pin-connected pier system

(b)

Elastomeric bearing-connected pier system

(c)

Figure 5.1. SDOF systems of piers

(a) Piers that are monolithically connected to deck of relatively high flexural stiffness are modeled with rotationally fixed tip SDOF systems.

(b) Piers that are pin connected to deck are modeled as cantilever elements with free tips.

(c) Piers which are elastomeric bearing connected to deck are modeled as cantilever elements with zero-length elastic links representing bearings.

In addition to connection type, two types of pier sections are considered in this research study. The analyses are performed for both circular and rectangular sections. In case of rectangular sections, the analyses are performed in both directions of sectional dimensions representing the seismic analyses of piers in both longitudinal and transverse directions of the bridge.

A study conducted on elastoplastic SDOF and MDOF systems by Behnoud Ganjavi and Hong Hao [58] shows that soil-structure interaction (SSI) ensued from the interaction between the foundations and the surrounding soil during earthquakes, affect the strength reduction factor of systems having high structure-to-soil stiffness ratio, especially with very loose soil. The results showed lower R-factor values for systems of loose soil due to the effect of foundation-soil interaction on the natural period. However, The SSI effect is not included in the scope of this study as the R-factor is based on the net displacement of piers and the natural period of bridge structures where the foundation-soil system effect might take place. Therefore, the foundation-soil system is neglected, and fixed-base SDOF systems are used.

5.3 Response Spectrum Analyses Procedure

The linear analyses in this research study are conducted via the response spectrum analyses procedure, which is the most widely used elastic analyses procedure in the seismic design of structures. It is performed on the SDOF systems for a variety of design parameters to obtain the elastic demand forces.

The parameters used in the RSA are T_c, *PGA*, T_n, and the arbitrary rigid mass. Next, the elastic moment demand at the base of the SDOF system is obtained by conducting simple RSA, in which the smoothed response spectrum of the considered corner period (T_c) is scaled in accordance with the PGA value and used to obtain the spectral acceleration corresponding to the fundamental natural period of the bridge T_n.

The elastic moment demand is calculated as follows:

$$M_e = mass \cdot S_a(T_n) \cdot H_s \quad (41)$$

where M_e is the elastic moment demand at the base of the SDOF system, $S_a(T_n)$ is the spectral acceleration corresponding to the period of structure T_n, and H_s is the shear span length of the pier.

5.4 Nonlinear Time History Analyses Procedure

In the performance-based seismic design of structures, the performance limit states are expressed in many forms such as curvature, rotation, strain, drift, and displacement. However, in engineering practice, displacement is considered as an important design parameter indicating the seismic response of structures.

In this research study, the average maximum displacement for each set of ground motions is obtained using NTHA procedure, which is one of the most preferred methods to estimate the actual nonlinear response of structures. Moreover, it is commonly used in the seismic design of bridges by simulating the seismic behavior of structures throughout various earthquake scenarios representing site seismicity.

Accordingly, the NTHA procedure is conducted for various ranges of the considered parameters, and its results are compared to those obtained from the RSA procedure.

Defining the nonlinear properties of the SDOF systems, lumped plasticity approach is used by localizing nonlinearity in certain regions in which plastic deformations are expected to take place. Therefore, plastic hinges are defined based on the idealized moment-curvature relationship of the pier section. Herein, the idealized moment-curvature relationship used in NTHA is derived based on the procedure presented in Chapter 4.

Among various hysteretic models that have been studied, The Ibarra-Medina-Krawinkler (IMK) hysteretic model [11] is used to simulate the seismic behavior of the SDOF systems.

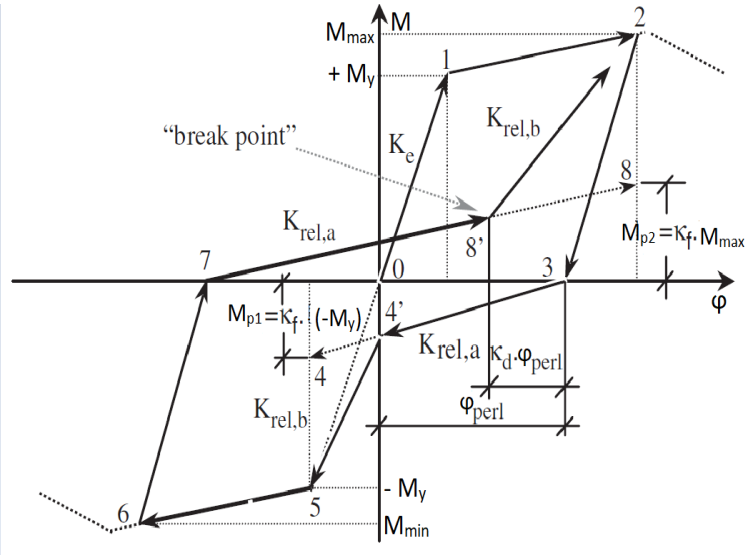

Figure 5.2. IMK pinching hysteretic model.

The IMK hysteretic model accounts for many properties and features such as pinching, strength, and stiffness deteriorations that are critical for estimating the strength and displacement demands of structures experiencing deteriorations or collapse [59]. However, due to the limited studies conducted to determine the model parameters, only the IMK pinching hysteretic model shown in Fig. 5.2 is used, where the strength and stiffness deteriorations are neglected in this research study.

The used pinching IMK model is based on defining a peak-oriented backbone curve representing the monolithic idealized moment-curvature relationship of the section, in addition to two parameters $k, and\ \gamma$ that represent pinching and the cyclic energy dissipation capacity, respectively. These parameters are obtained by the formulas proposed by Zhen Wang et al. [59] as follows:

$$k = 0.481 + 0.0886\,\frac{H_s}{h} - 7.42 \qquad k \geq 0.2\,, \leq 1.0 \tag{42}$$

$$\gamma = 1330 + 262\,\frac{H_s}{h} - 58000 \qquad \gamma \geq 100\,, \leq 2000 \tag{43}$$

Consequently, parametric NTHA of the SDOF systems are conducted for various ranges of the considered parameters by developing a finite element-based nonlinear time history analysis program using OpenSees [12].

The direct integration of NTHA procedure is performed by modeling a SDOF system with rigid mass. Moreover, the nonlinearity of the system is presented by assigning plastic hinges of lengths calculated in accordance with the following expression [1]:

$$L_p = 0.08H_s + 0.022\, f_{sy}\, d_{bl} \geq 0.044\, f_{sy}\, d_{bl} \tag{44}$$

where L_p is the plastic hinge length, and d_{bl} is the maximum diameter of the longitudinal steel bars used in the section. The other parts of pier are modeled to remain elastic with cracked section properties by applying the cracked section factor (CSF), which is calculated as:

$$CSF = \frac{E_c\, I_{cr}}{E_c\, I_g} = \frac{M_y}{\varphi_y (E_c\, I_g)} \tag{45}$$

where CSF is the cracked section factor, E_c is the modulus of elasticity of concrete, I_g is the gross moment of inertia, and I_{cr} is the cracked moment of inertia.

5.5 Strength Reduction Factor

By comparing the results obtained from the RSA and the NTHA procedures, the strength reduction factor is obtained as the ratio of the elastic moment force M_e from the RSA to the plastic moment capacity, which is considered as M_y obtained from the NTHA procedure.

$$Strength\ reduction\ factor\ (R) = \frac{M_e}{M_y} \tag{46}$$

5.6 Effect of Transverse Reinforcements on R-factor

A Sensitivity analysis is conducted on a sample of SDOF systems to examine the effect of transverse reinforcements on the strength reduction factor. RSA and NTHA procedures are performed on a wide range of transverse reinforcement ratio (ρ_t) varying between 0.003 and 0.015. As shown in Fig.5.3, the results of this sensitivity analysis indicate that the variation in transverse reinforcement ratio within the considered range does not significantly affect the strength reduction factor. This insignificant effect could be interpreted by the limited influence of transverse reinforcements on the yield strength capacity and the post-yield stiffness of piers. However, the results showed a notable increase in both the ultimate moment and curvature capacities of the analyzed piers.

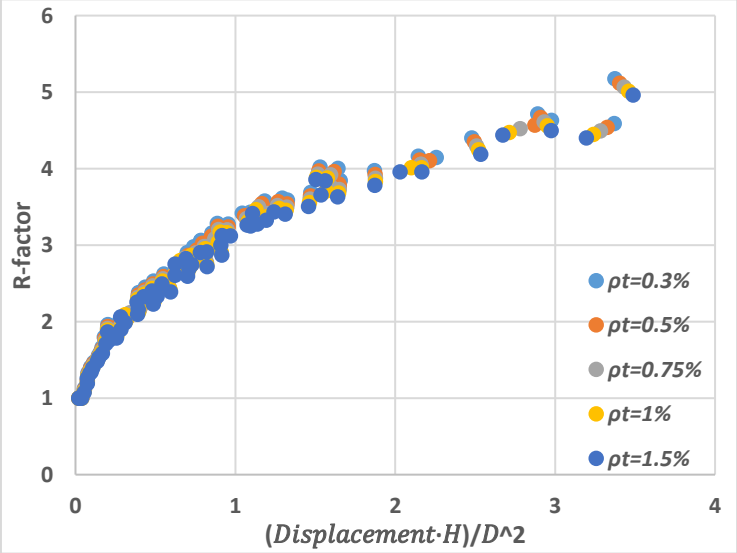

Figure 5.3. Effect of transverse reinforcements on R-factor.

Consequently, the transverse reinforcement ratio is not considered as a variant parameter in this research study but constant with an averaged post-yield stiffness.

Therefore, the used hysteretic model is modified so that an idealized bilinear moment-curvature relationship is used.

5.7 Development of the Proposed R-factor Equations

In this subsection, the data analysis procedures conducted on the results obtained from the parametric RSA and NTHA are introduced. Furthermore, the data model used to generate the proposed R-factor equations is presented.

First, the R-factors and tip displacements of the SDOF systems are collected. Next, the collected results are combined with the corresponding design parameters and structured in 9 different data sets. The obtained data sets represent various piers classified based on their substructure-superstructure connection, the direction of analyses, and section type. Then, these data sets are mined and analyzed by applying Principal Component Analysis to reduce their dimensionality. Next, 9 R-factor equations are developed by performing multiple linear regression analyses for each data set. Finally, the error performance of the proposed R-factor equations is investigated and discussed.

5.7.1 Data Mining

Nine strength reduction factor equations for bridges subjected to FFGM are aimed to be developed. For this purpose, 9 data sets are generated from the conducted parametric RSA and NTHA corresponding to different pier configurations are obtained.

Firstly, these data sets are structured in terms of the considered parameters in addition to the demand tip displacement resulted from the NTHA. The considered tip displacement is calculated as the average of the maximum tip displacements for each group of ground motions.

Secondly, the prepared data sets are mined such that the data of SDOF systems showing average displacements less than the corresponding yield displacement or more than the maximum displacement are eliminated.

In this research study, the yield displacement dy is calculated based on the yield curvature φ_y obtained from the conducted sectional analyses for each SDOF system as:

$$dy = c_1 \varphi_y H^2 \tag{47}$$

where, c_1 here is a constant depending on piers' tip connection type. It could be assumed as (1/3) for free end or elastomeric bearing connected piers and (1/6) for fixed tip piers [1]. The maximum displacement of the elastoplastic SDOF systems is defined as the displacement corresponding to the capping point of the moment-curvature relationship of 0.015 transverse reinforcement ratio. The capping displacement d_c is calculated as:

$$d_c = d_y + (\varphi_c - \varphi_y) L_P H \tag{48}$$

where, φ_c is the capping curvature, and L_P is the plastic hinge length.

5.7.2 Data Structuring

After the data sets have been mined, they are structured in the shape of matrices such that each column represents a design parameter. For simplicity and to reduce the dimensionality of the obtained data, we decided to reduce the number of parameters. For this purpose, a dimensionality reduction procedure of two steps is performed.

Firstly, based on our structural engineering knowledge, the parameters anticipated to have significant effects on R-factor are addressed in several forms resulting in different parametric combinations.

Secondly, Principal Components Analysis (PCA) procedure is performed on the obtained parametric combinations to eliminate the parameters that have negligible

effects on the parametric variation of the data sets. PCA procedure is one of the most popular techniques used in data science. The PCA procedure is generally performed on high dimensional data that consists of observations expressed by various inter-correlated variables. It is used to reduce the dimensionality by extracting the important variables which their variations significantly affect the data properties respectively with their eigenvalues and express them as a new data set of orthogonal components [60].

Accordingly, the dimensionality reduction procedure is conducted on several parametric combinations in which important parameters are expressed in different forms such as displacement d, drift ($\frac{d}{H}$), and ductility μ. As a result, we found that expressing tip displacement in terms of displacement ductility μ along with the other parameters yields the best combination.

5.7.3 Development of the Proposed R-factor Equations

Based on the adopted parametric combinations, parametric linear regression analyses are performed for each data set to derive R-factor equations. The R-factor equations proposed in this research study are derived to be used in the performance-based seismic design of bridge structures considering the seismic performance of bridge piers as the main earthquake resisting system. Hence, the proposed equations are prepared to estimate the R-factor values used in calculating the elastic design forces of piers considering their tip displacements. For simplicity, the proposed R-factor equations are assumed to have the following power function form.

$$R = C_0 \cdot {X_1}^{C_1} \cdot {X_2}^{C_2} \cdot \ldots {X_n}^{C_n} \quad (49)$$

where $C_0, C_1, C_2, and\ C_n$ are coefficients determined via regression analyses on the available data sets. Although liner regression analysis procedure is used to analyze data and to find coefficients of linear functions, the coefficients of the assumed power functions are calculated by applying linear regression analysis on the natural logarithmic transformation of the data such as:

$$ln(R) = ln(C_0) + C_1 \cdot ln(X_1) + C_2 \cdot ln(X_2) + \dots C_n \cdot ln(X_n) \quad (50)$$

It is noteworthy that all the proposed R-factor equations are expressed in simple dimensionless form enabling designers to calculate the corresponding R-factor for each pier easily. Moreover, the error performance of the proposed equations is investigated by performing error analyses based on the relative error of the R-factor values estimated via the proposed equations for the available data sets. The relative error for each data point is calculated as follows.

$$relative\ error\ (\%) = 100\% \cdot \frac{R_{estimated} - R_{calculated}}{R_{calculated}} \quad (51)$$

Accordingly, the proposed R-factor equations for the available data sets are presented along with their goodness of fit plots and their error distributions.

5.7.3.1 R-factor Equation for Circular Piers of Pinned Tip

$$R = 8 \cdot \frac{\mu^{0.21} \cdot (D \cdot PGA \cdot T_n \cdot T_C)^{0.75}}{H^{1.5} \cdot {\rho_l}^{0.12}} \geq 1 \tag{52}$$

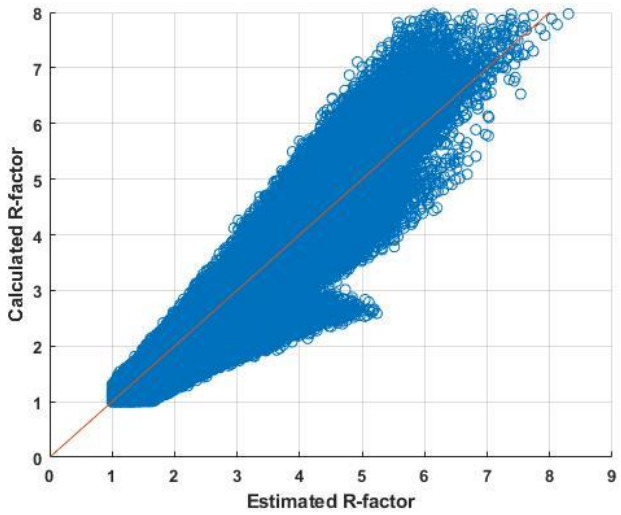

Figure 5.4. R-factor goodness of fit scatter plot for circular piers of pinned tip.

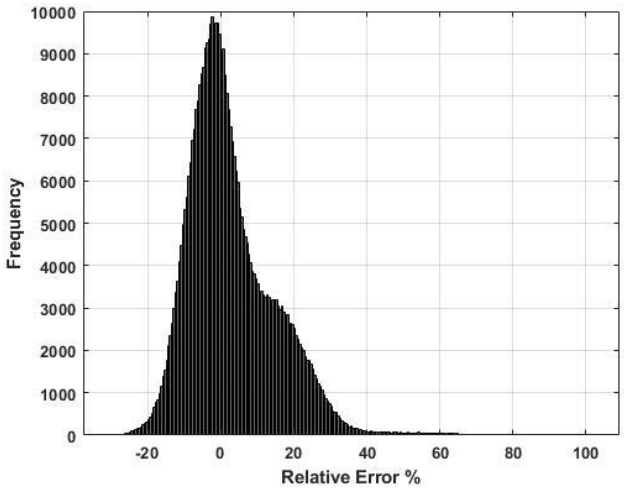

Figure 5.5. Relative error distribution of the estimated R-factor values for circular piers of pinned tip.

5.7.3.2 R-factor Equation for Circular Piers of Fixed Tip

$$R = 10 \cdot \frac{\mu^{0.27} \cdot D^{0.65} \cdot (PGA \cdot T_n \cdot T_C)^{0.7}}{H^{1.35} \cdot \rho_l{}^{0.11}} \geq 1 \tag{53}$$

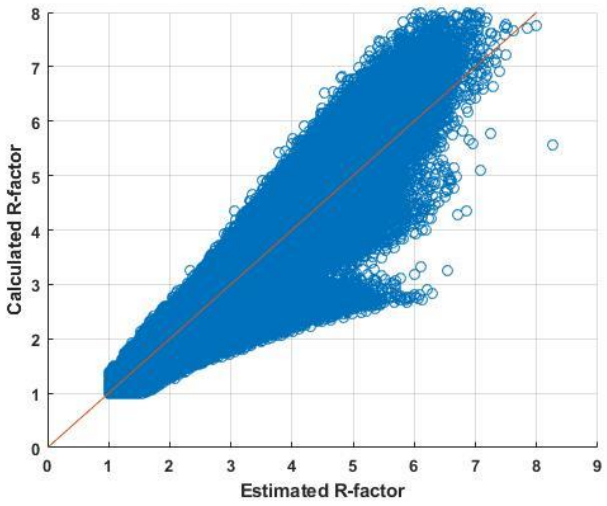

Figure 5.6. R-factor goodness of fit scatter plot for circular piers of fixed tip.

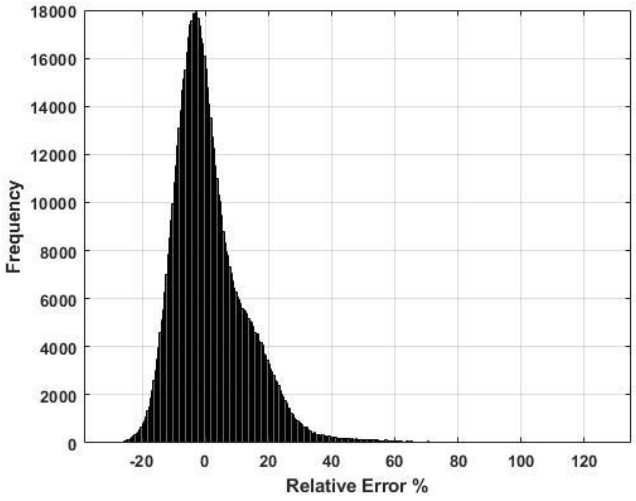

Figure 5.7. Relative error distribution of the estimated R-factor values for circular piers of fixed tip.

5.7.3.3 R-factor Equation for Circular Piers of Elastomeric Bearing Connected Tip

$$R = 2 \cdot \frac{\mu^{0.17} \cdot D^{0.52} \cdot (PGA \cdot T_n \cdot T_C)^{0.7} \cdot {K_r}^{0.6}}{H^{1.22} \cdot {\rho_l}^{0.36}} \geq 1 \tag{54}$$

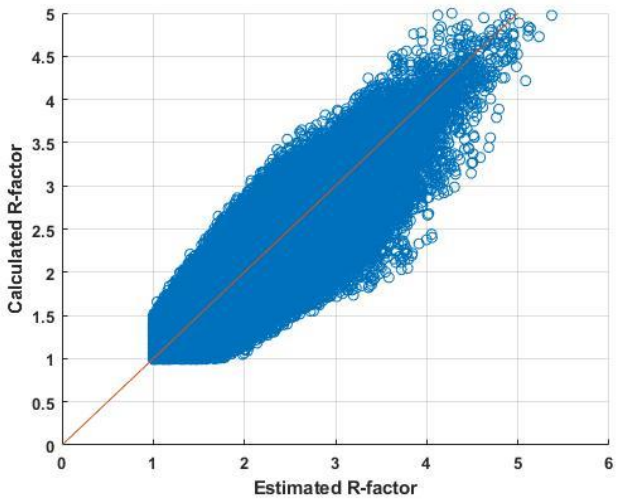

Figure 5.8. R-factor goodness of fit scatter plot for circular piers of elastomeric bearing connected tip.

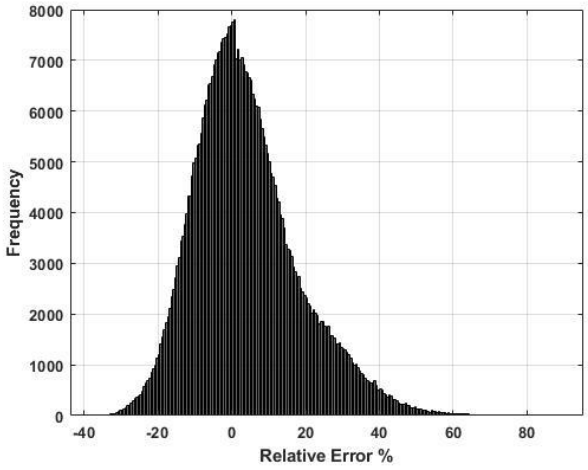

Figure 5.9. Relative error distribution of the estimated R-factor values for circular piers of elastomeric bearing connected tip.

5.7.3.4 R-factor Equation for Rectangular Piers of Pinned Tip in the Short Direction *(h < b)*

$$R = 11.4 \cdot \frac{\mu^{0.22} \cdot (h \cdot PGA \cdot T_n \cdot T_C)^{0.75}}{H^{1.5} \cdot \rho_l{}^{0.03}} \geq 1 \tag{55}$$

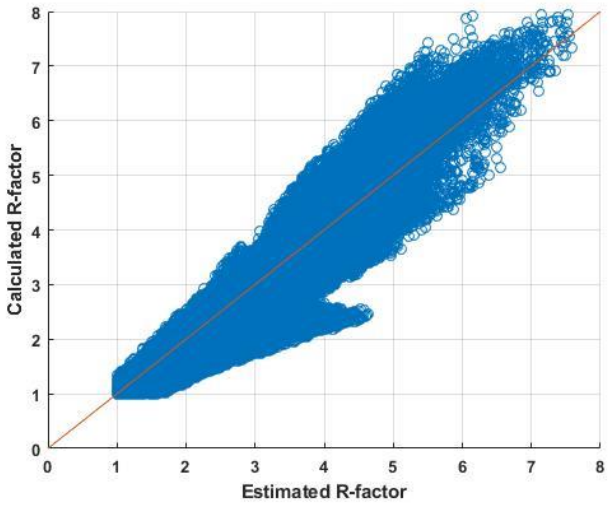

Figure 5.10. R-factor goodness of fit scatter plot for rectangular piers of pinned tip in the short direction.

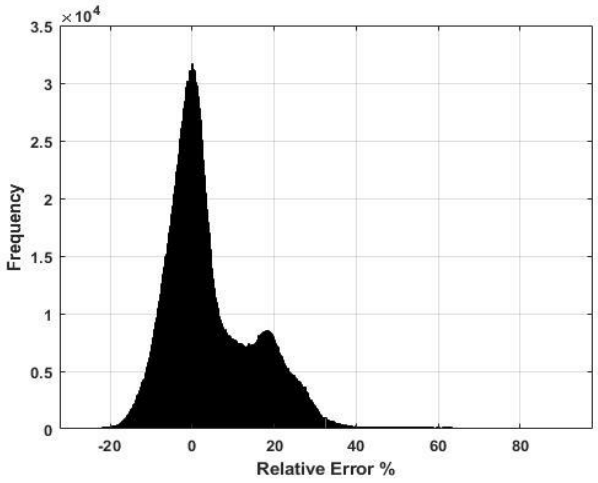

Figure 5.11. Relative error distribution of the estimated R-factor values for rectangular piers of pinned tip in the short direction.

5.7.3.5 R-factor Equation for Rectangular Piers of Fixed Tip in the Short Direction *(h < b)*

$$R = 7.8 \cdot \frac{\mu^{0.4} \cdot h^{0.52} \cdot PGA^{0.55} \cdot {T_n}^{0.5} \cdot {T_C}^{0.6}}{H^{1.07} \cdot {\rho_l}^{0.05}} \geq 1 \tag{56}$$

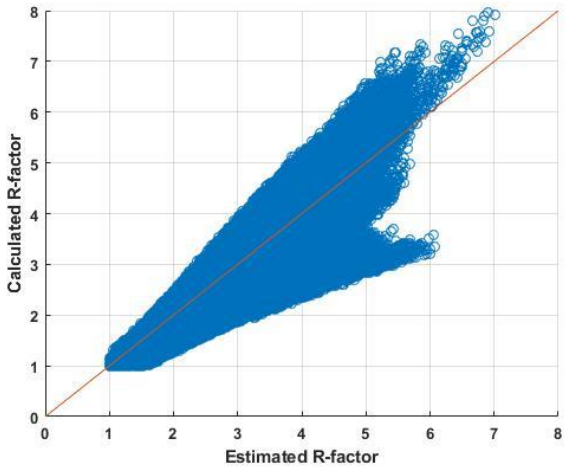

Figure 5.12. R-factor goodness of fit scatter plot for rectangular piers of fixed tip in the short direction.

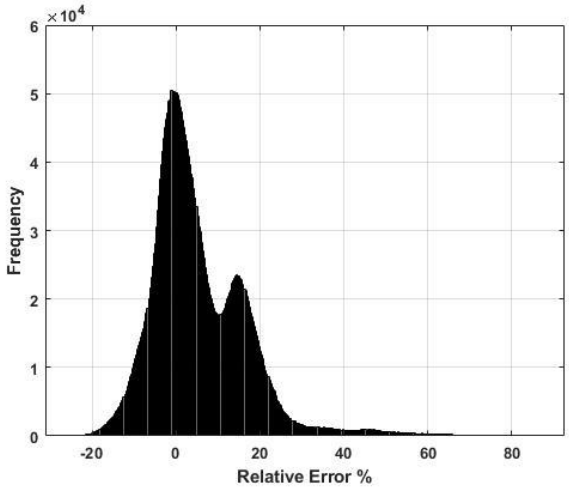

Figure 5.13. Relative error distribution of the estimated R-factor values for rectangular piers of fixed tip in the short direction.

5.7.3.6 R-factor Equation for Rectangular Piers of Elastomeric Bearing Connected Tip in the Short Direction *(h < b)*

$$R = 1.9 \cdot \frac{\mu^{0.22} \cdot h^{0.48} \cdot PGA^{0.62} \cdot {T_n}^{0.54} \cdot {T_C}^{0.7} \cdot {K_r}^{0.4}}{H^{1.1} \cdot {\rho_l}^{0.3}} \geq 1 \tag{57}$$

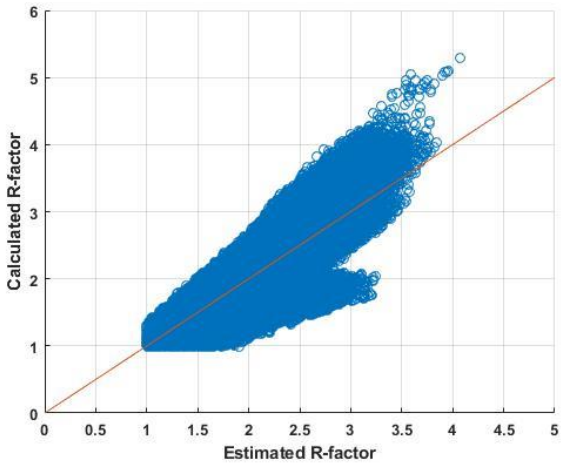

Figure 5.14. R-factor goodness of fit scatter plot for rectangular piers of elastomeric bearing connected tip in the short direction.

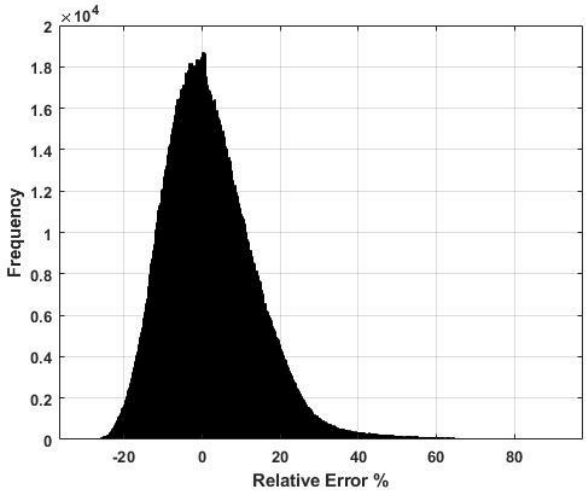

Figure 5.15. Relative error distribution of the estimated R-factor values for rectangular piers of elastomeric bearing connected tip in the short direction.

5.7.3.7 R-factor Equation for Rectangular Piers of Pinned Tip in the Long Direction *(h > b)*

$$R = 9.8 \cdot \frac{\mu^{0.26} \cdot h^{0.7} \cdot (PGA \cdot T_n \cdot T_C)^{0.7}}{H^{1.4} \cdot \rho_l{}^{0.04}} \geq 1 \tag{58}$$

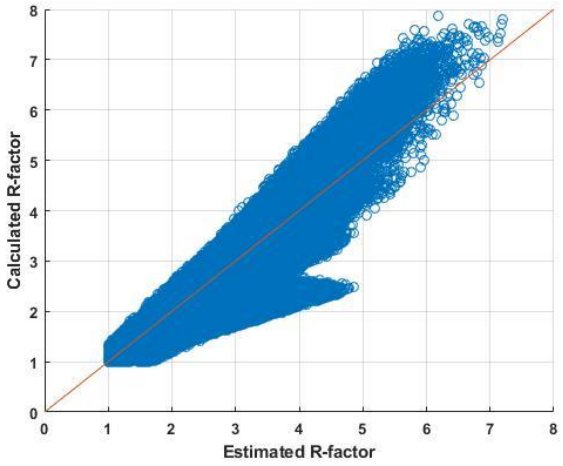

Figure 5.16. R-factor goodness of fit scatter plot for rectangular piers of pinned tip in the long direction.

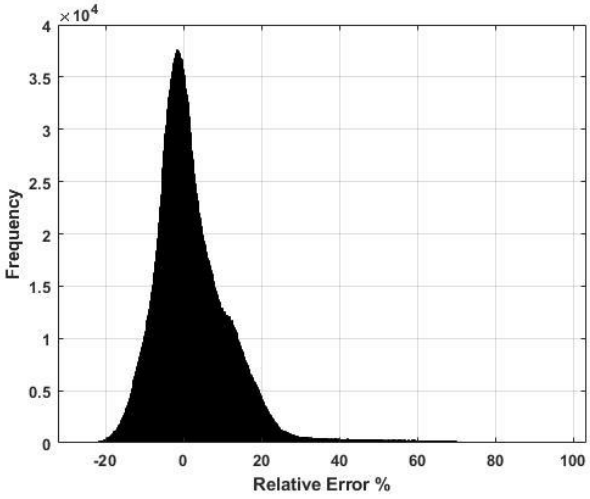

Figure 5.17. Relative error distribution of the estimated R-factor values for rectangular piers of pinned tip in the long direction.

5.7.3.8 R-factor Equation for Rectangular Piers of Fixed Tip in the Long Direction *(h > b)*

$$R = 7 \cdot \frac{\mu^{0.43} \cdot (h \cdot PGA \cdot T_n \cdot T_C)^{0.5}}{H \cdot {\rho_l}^{0.04}} \geq 1 \tag{59}$$

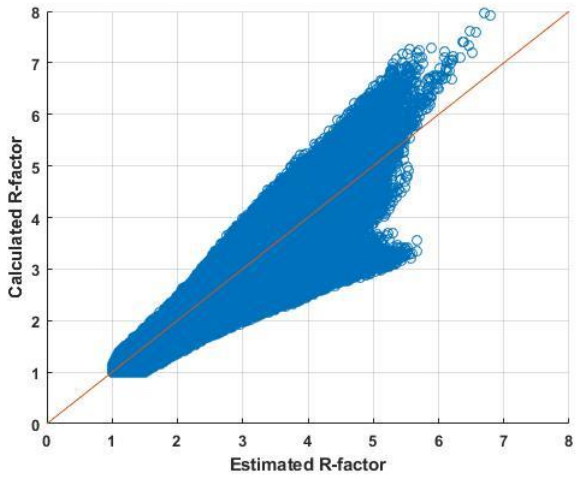

Figure 5.18. R-factor goodness of fit scatter plot for rectangular piers of fixed tip in the long direction.

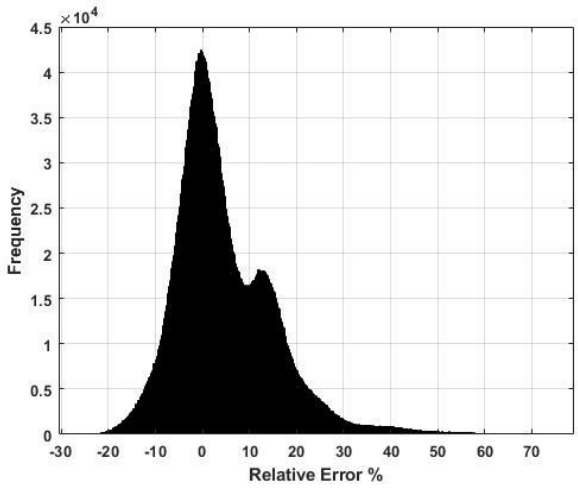

Figure 5.19. Relative error distribution of the estimated R-factor values for rectangular piers of fixed tip in the long direction.

5.7.3.9 R-factor Equation for Rectangular Piers of Elastomeric Bearing Connected Tip in the Long Direction *(h > b)*

$$R = 1.5 \cdot \frac{\mu^{0.26} \cdot h^{0.4} \cdot PGA^{0.53} \cdot {T_n}^{0.5} \cdot {T_C}^{0.56} \cdot {K_r}^{0.4}}{H^{0.93} \cdot {\rho_l}^{0.3}} \geq 1 \tag{60}$$

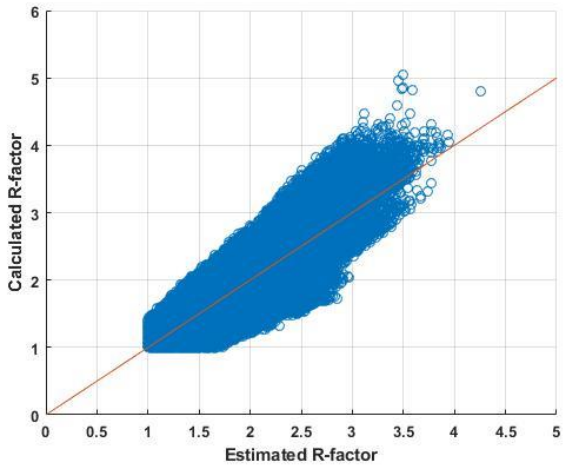

Figure 5.20. R-factor goodness of fit scatter plot for rectangular piers of elastomeric bearing connected tip in the long direction.

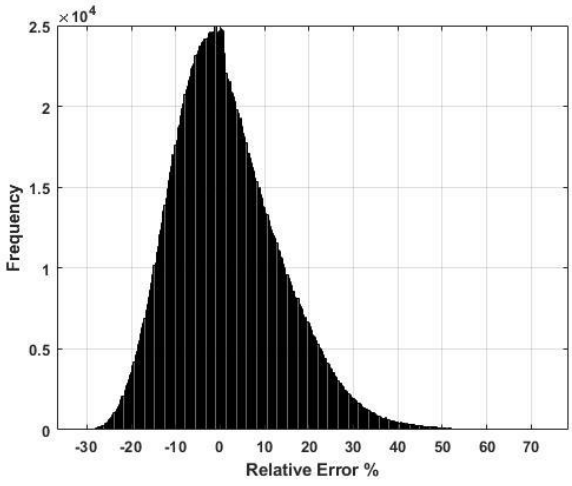

Figure 5.21. Relative error distribution of the estimated R-factor values for rectangular piers of elastomeric bearing connected tip in the long direction.

5.7.4 Discussion of Results

From the results described in Fig. (5.4-5.21), the proposed R-factor equations show acceptable fitting to the identity line, which illustrates the goodness of fit of the estimated values to the actual values. Furthermore, the performed error analyses show high accuracy of the data models as the error distributions have peaks around values very close to zero. Further details of the error performance of the derived equations are presented in Table 5.1 as follow:

Table 5.1 Data analysis results of the derived R-factor equations

Section	*Connection*	*Data Points*	R^2	*Mean Error %*	*Error STD %*	
Circular	Pin	429261	0.95	2.83	11.98	
	Rotationally Fixed	757128	0.94	1.6	11.94	
	Elastomeric Bearing	463514	0.87	3.94	14.31	
Rectangular	Pin	1724858	0.94	4.55	11.39	*Short Direction*
	Rotationally Fixed	3167386	0.94	5.31	11.32	
	Elastomeric Bearing	1634068	0.85	0.85	11.64	
	Pin	2116949	0.94	2.5	10.79	*Long Direction*
	Rotationally Fixed	3765609	0.94	4.54	10.53	
	Elastomeric Bearing	2252771	0.83	1.47	12.05	

CHAPTER 6

PERFORMANCE-BASED SEISMIC DESIGN PROCEDURE

6.1 Introduction

In this chapter, a new performance-based seismic design procedure for RC bridge structures is proposed. The proposed design procedure mainly depends on the derived R-factor equations in Chapter 5. The implementation of the proposed design procedure is clearly explained throughout design examples for several bridge structures of different types. Moreover, the verification of the designs is done by performing nonlinear time history analyses on the designed bridges showing their reliability of achieving the stated performance objectives.

6.2 Performance Objectives

In the performance-based design of structures, the performance objective is a statement correlating seismic levels with several performance levels defined based on acceptable damage limit states. Starting with damage limit states, the damage status of elements during seismic actions is considered an important factor in performance-based design. The damage statuses of members are determined based on material strains and expressed using quantitative limit states of many forms such as displacement, drift, and rotation.

Among several damage limit states recommended by various research studies [2], [61]–[64], serviceability, damage control, and collapse prevention limit states are widely used in literature and many design codes. Serviceability indicates no need for damage repair. Damage control accounts for repairable damage only. Collapse prevention means that damage could not be repairable, but collapse must be prevented. Quantitatively, research studies [61], [64] recommended material strain

values for both serviceability and damage control limit states. Regarding serviceability limit state, it is recommended that tensile strain of reinforcing rebars (ε_s) should be limited to 0.015, where the compressive strain of concrete (ε_c) should be limited to 0.004. Similarly, the strain limits of tension rebars and concrete corresponding to damage control are suggested not to exceed 0.06, 0.018, respectively.

In the report presented by Hwang *et al.* [65], five damage levels of highway bridge columns are suggested based on damage severity. The corresponding limit states are expressed in terms of displacement ductility ratios calculated with respect to the first yield displacement of columns. Although expressing limit states in terms of material strains is the best way to describe damage, the measurement of strains during design and assessment stages may not be practical.

In the study presented by Ghobarah [2], five damage limit states are introduced in drift form such as (No damage < 0.2%, Repairable damage < 0.5%, Irreparable damage < 1.5%, Near collapse < 2.5%, and Collapse > 2.5%). Based on earlier research efforts [30]–[32], the study [2] related the introduced damage levels into various operation levels.

To indicate damage limit states in more simple engineering parameters, Priestley et al. [1] recommended four damage levels expressed in displacement limit states. The proposed limit states are based on flexural rotations of bridge columns at plastic hinge levels. Accordingly, the limit states are indicated as a function of column's yield (d_y) and ultimate (d_u) displacements. Nevertheless, the study [1] provided a set of expressions to calculate tip displacements of bridge columns considering yield and ultimate curvatures.

A summary of the aforesaid limit states proposed by various research studies is presented in Table 6.1.

Table 6.1 Damage /Performance levels and limit states

Study	Damage/ Performance level	Limit states
Priestley *et al.* [64] & Kowalsky [61]	Serviceability	$\varepsilon_s < 0.015$ *or* $\varepsilon_c < 0.004$
	Repairable damage	$\varepsilon_s < 0.06$ *or* $\varepsilon_c < 0.018$
Hwang *et al.* [65]	No damage	$\mu_d < \mu_{(first\ yield)}$
	Slight damage	$\mu_{(first\ yield)} < \mu_d < \mu_{(global\ yield)}$
	Moderate damage	$\mu_{(global\ yield)} < \mu_d < \mu_{(\varepsilon_c = 0.002)}$
	Extensive damage	$\mu_{(\varepsilon_c = 0.002)} < \mu_d < \mu_{max}$
	Complete damage	$\mu_{max} < \mu_d$
Ghobarah [2]	No damage/Immediate occupancy	*Drift* < 0.2%
	Repairable damage/Operational	*Drift* < 0.5%
	Irreparable damage/Life safe	*Drift* < 1.5%
	Severe damage/Near collapse	*Drift* < 2.5%
	Collapse	*Drift* > 2.5%
Priestley *et al.* [1]	Slight damage	$d < d_y$
	Moderate damage	$d < d_y + \frac{1}{2}(d_u - d_y)$
	Severe damage	$d < d_y + \frac{2}{3}(d_u - d_y)$
	Collapse prevention	$d < d_u$

According to most seismic design codes of bridge structures (e.g. TKDY [48]), limit states of piers are usually presented in terms of flexural damage, where damage due to shear is prevented by capacity design.

For reliable performance-based designs of structures, performance levels are generally associated with various hazard levels that are usually defined in accordance with the frequency of seismic events. Some of the commonly used hazard levels presented in [2] are listed in Table 6.2.

Table 6.2 Seismic hazard levels [2]

Frequency of seismic event	Return period (years)	Probability of exceedance
Frequent	43	50% in 30 years
Occasional	72	50% in 50 years
Rare	475	10% in 50 years
Very rare	970	5% in 50 years
Extremely rare	2475	2% in 50 years

For the sake of designing structures able to achieve multiple performance levels accounting for more than one possible seismic event, several design objectives were proposed by various researchers [30]–[32]. Indeed, structures are classified into different types based on their importance. Three main importance classes of structures are used in engineering practice such as basic, essential, and critical structures. For example, the performance objectives introduced by Vision 2000 [30] are presented in Fig. 6.1.

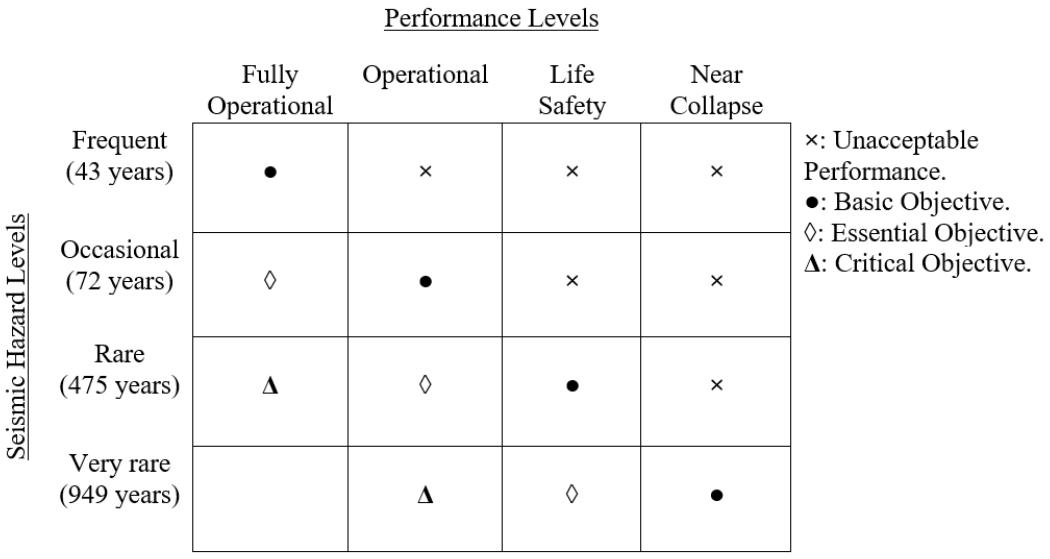

Figure 6.1. Performance objectives suggested by vision 2000 [30].

It should be noted that there are various performance objectives as well as importance classes for different types of structures presented in literature and seismic design codes. Regarding the seismic design of bridges, several design codes recommended designing bridges for multiple performance levels. In contrast with the LRFD specifications [6], in which bridges are designed for a single performance level of 1000-year return period earthquake, other design codes and guidelines recommended multi-performance levels. In Eurocode [7], bridges are designed to achieve limited ductile/damage and life safety performance levels associated with seismic hazards of 95-year and 475-year return periods, respectively. According to the highway bridge specifications by the South Carolina Department of Transportation SCDOT [66], two hazard levels of 462-year and 975-year return periods are used. For the 462-year hazard level, limited damage state is required, where repairable damage shall be sustained for the 975-year hazard level. The Canadian Highway Bridge Design Code CSA [46] recommends two hazard levels associated with 475-year and 2475-year return periods. The 475-year hazard level required a performance level of minimal damage, where at the 2475-year hazard level, severe damage is allowed. Along with these design criteria, other seismic design criteria existing in different design codes are compared and discussed in the review study presented by Zhang & Alam [3].

A summary of the design criteria recommended by some seismic design codes mentioned above is presented in Table 6.3.

Table 6.3 Design criteria recommended by some seismic design codes

Design Code	Seismic Hazard Level	Damage/ Performance level
AASHTO LRFD [6]	1000-year	Life Safety
Eurocode [7]	95-year	Limited Damage
	475-year	Life Safety
SCDOT [66]	462-year	Limited Damage
	975-year	Repairable Damage
CSA [46]	475-year	Minimal Damage
	2475-year	Severe Damage

6.3 Evaluation of Performance Displacement Profile

Among various forms of performance limit states, expressing flexural damage in terms of displacement is very common as it is easy to be measured and calculated in engineering practice. For this reason, the design displacements of piers are calculated with respect to curvature values determined based on predefined material strains at plastic hinge locations. Accordingly, the design displacements of bridge piers are calculated in this study based on the displacement limit states proposed by Priestley et al. [1]. As shown in Table 6.1, displacement limit states are defined as a function of ultimate and yield displacements calculated as:

$$d_u = d_y + (\varphi_u - \varphi_y) L_P H \quad (61)$$

Regarding estimating the yield and ultimate curvatures of pier sections, the equations proposed in Chapter 4 are adopted in this study. Based on the design parameters of pier sections, the proposed equations account for estimating the yield and ultimate curvature capacities for both circular and rectangular sections.

Unlike longitudinal direction, in which the estimation of the performance displacement profile is straightforward, the determination of the displacement performance profile in transverse direction might be more complex. Based on several characteristics of multiple span bridges with continuous decks (such as geometry, abutment connection, superstructure stiffness, and substructure stiffness), various inelastic displacement patterns could be defined. As described in Fig. 6.2, Dwairi et al. [38] identified three patterns of inelastic displacement of bridges as (a) and (b) where translation motion of rigid superstructure is expected with equal displacements of all members. (c) and (d) displacement patterns illustrate a rigid body translation combined with rotation ensued from the eccentricity of mass and rigidity centers. (e) and (f) illustrate symmetric displacement patterns of flexible superstructure.

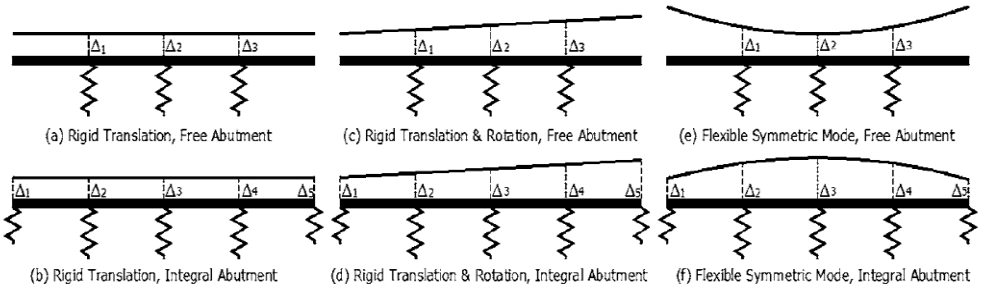

Figure 6.2. Plan views of possible inelastic displacement patterns for continuous bridges [38].

Along with the abovementioned inelastic displacement patterns, other patterns could be derived depending on different bridge configurations. It is important to mention that in order to obtain the performance displacement profile corresponding to a predefined performance level, the derived displacement pattern needed to be scaled to the so-called ‘’performance point’’ determined based on the critical bridge element.

The derivation of the performance displacement profile has been under critical investigation for the past decades. In the studies presented by Kowalsky [37] and that by Dwairi et al. [38], a procedure to derive the performance displacement profile of bridge structures was introduced. The introduced procedure is based on elastic modal analysis in which a 5%-damped spectrum is used. Accordingly, for bridges expected to have elastic response in transverse direction, the performance displacement profile could be obtained using the elastic properties. However, for bridges in which significant relative stiffness difference of piers and abutments is anticipated due to the inelastic response of elements, the derivation of the performance displacement profile becomes more challenging. To tackle this issue, the abovementioned studies [37], [38] proposed the so-called ‘’effective mode shape’’ approach which is based on the secant stiffness of substructure to detect more realistic inelastic displacement patterns, particularly for bridges of flexible superstructures.

It should be noted that the performance displacement profile obtained using the effective mode shape (EMSh) approach is necessarily derived with respect to the fundamental mode neglecting the effects of higher modes. Since higher modes might have a significant effect on the seismic response of bridge structures, the use of the EMSh approach for bridges having higher modes effect could result in unrealistic performance displacement profiles and hence unreliable designs. Thus, Kappos et al. [67] proposed an extension to the EMSh approach to account for higher mode effects using suitable modal combination rules such as SRSS and CQC.

In addition to the abovementioned procedures that are mainly based on linear analysis, other procedures to derive the profile displacement profile are based on nonlinear analysis. Procedures such as the displacement-based pushover analysis presented by [68], and that presented by [69], which is based on modal pushover analysis to account for higher modes effects, are proposed. Nevertheless, other studies [70]–[72] adopted rational approaches to estimate the displacement profile of bridges. Such approaches are based on approximate functions of deformation patterns determined depending on bridge characteristics [73].

It should be mentioned that for an accurate approximation of the performance displacement profile using procedures based on inelastic properties, prior knowledge of design parameters is required. Thus, estimating the performance displacement profile using elastic methods is more appealing, especially in design stages, where prior knowledge of the inelastic properties might not be available. However, the performance-based design procedure proposed in this study is aimed to be suitable for many performance displacement profile estimation techniques.

6.4 Proposed Performance-Based Seismic Design Procedure

The proposed performance-based seismic design is presented as follows:

Step 1: Determination of performance objective.

Step 2: Dimensioning of piers, deck, and other elements of the bridge.

Step 3: Performing non-seismic structural analyses.

Step 4: Preliminary estimation of longitudinal reinforcements and effective elastic stiffness of piers.

In this step, the initial estimation of longitudinal reinforcements is made, where the effective stiffness EI_{eff} of piers is calculated as follows:

$$EI_{eff} = \frac{M_y}{\varphi_y} \tag{62}$$

where, M_y and φ_y are the yield moment and yield curvature capacities of the section calculated using the equations proposed in chapter 3.

Step 5: Performing 5%-damped modal and response spectrum analyses.

In this step, the resultant elastic forces (e.g., shear V_E, moment M_E), and the natural period of the bridge are calculated.

Step 6: Capacity-based shear design of piers.

In this step, the brittle failure of piers due to shear is prevented by satisfying the following relationship:

$$V_{CD} = \gamma_o \cdot \frac{M_y}{H_S} \tag{63}$$

where, V_{CD} is the shear capacity design force, and γ_o is the pier overstrength factor (has a value between 1.25 and 1.35 as recommended by [42]). From this step, the required transverse reinforcements are calculated, and the corresponding transverse reinforcement ratio is obtained for each pier.

Step 7: Derivation of the performance displacement profile.

In this step, the net displacements of piers are calculated with respect to the obtained performance displacement profile. It should be noted that the performance displacement profile could be derived by several means as described in the previous

section. Thus, this procedure provides the possibility of using various performance displacement profile derivation techniques.

Step 8: Evaluation of the strength reduction factor.

In this step, the strength reduction factor for each pier is evaluated using the equations proposed in chapter 5.

Step 9: Checking the capacity of the designed sections.

In this step, the yield moment capacities of piers calculated in step 4 are compared with the required yield moments calculated using the obtained R-factors. For a proper design, the following relationship must be satisfied:

$$|M_y - \frac{M_E}{R}| \leq \text{tolerance} \tag{64}$$

If this relationship is not satisfied, the assumed design parameters are changed, and the abovementioned steps are repeated.

Step 10: Designing for multiple performance objectives.

In case of designing bridges for multiple performance objectives, this step is added so that the performance of the designed bridge is validated for another performance level. Therefore, steps 7 & 8 are applied for the new performance level PL_2 using the same pier section properties resulted from the design process of PL_1. Accordingly, the performance displacement profile corresponding to PL_2 is derived from step 7. Next, the R-factor values of piers corresponding to PL_2 are calculated from step 8. Then, the design of piers is validated by satisfying the following relationship:

$$R_1 \cdot \frac{PGA_2}{PGA_1} \leq R_2 \tag{65}$$

where, R_1 & R_2 , and PGA_1 & PGA_2 are the R-factor values and peak ground acceleration values corresponding to PL_1 and PL_2, respectively.

6.5 Implementation of the Proposed Performance-Based Seismic Design Procedure

In this section, the implementation of the proposed design procedure is described via design examples representing bridge structures of various configurations. For this sake, three multiple-span straight bridges of various substructure-superstructure connections are presented (See Fig. 6.3). The bridges shown in Fig. 6.3 are designed for circular sections, where the final design is verified by performing NTHA.

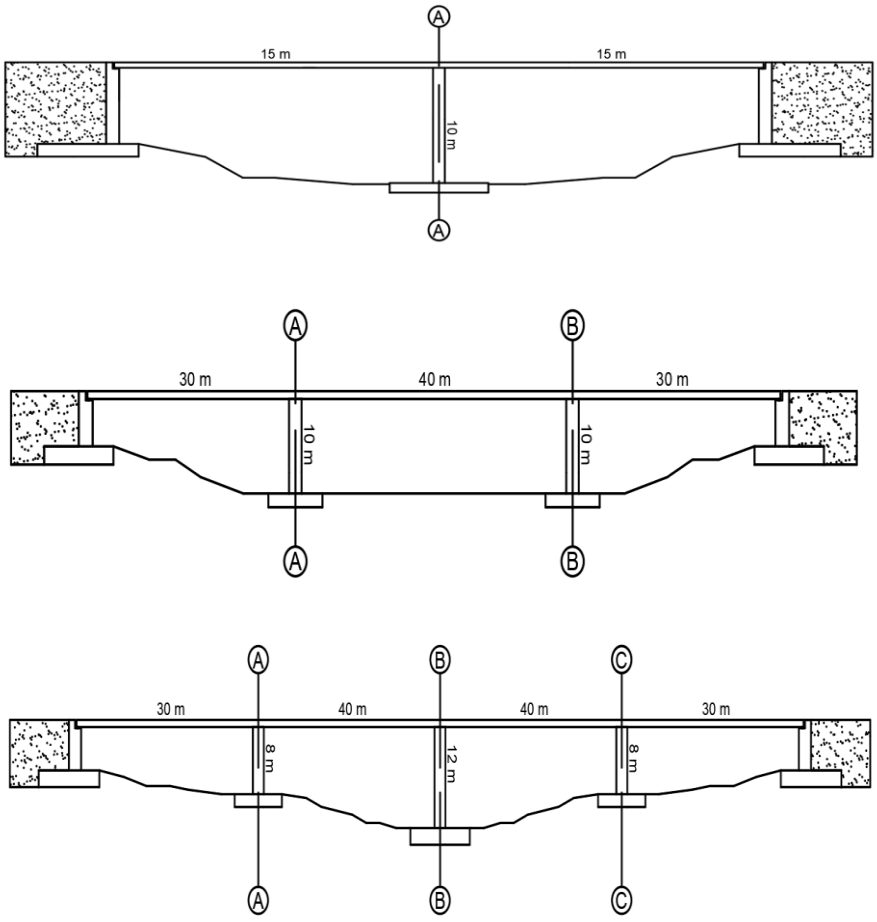

Figure 6.3. Design examples of continuous bridge structures.

For all bridges shown in Fig. 6.3, the superstructure is modeled as a continuous deck of 10 m width, and supported by seven I-shaped girders as shown in Fig. 6.4 below:

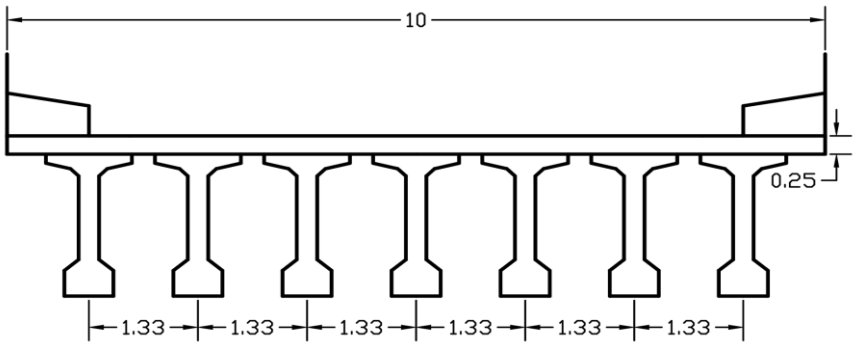

Figure 6.4. Cross-section of superstructure.

Indeed, the bridges shown in Fig. 6.3 are modeled, including the soil-structure interaction effect at abutments. For all the designed bridges, the same abutment is used. The abutment is designed to have a height of 6 m and a width of 10 m.

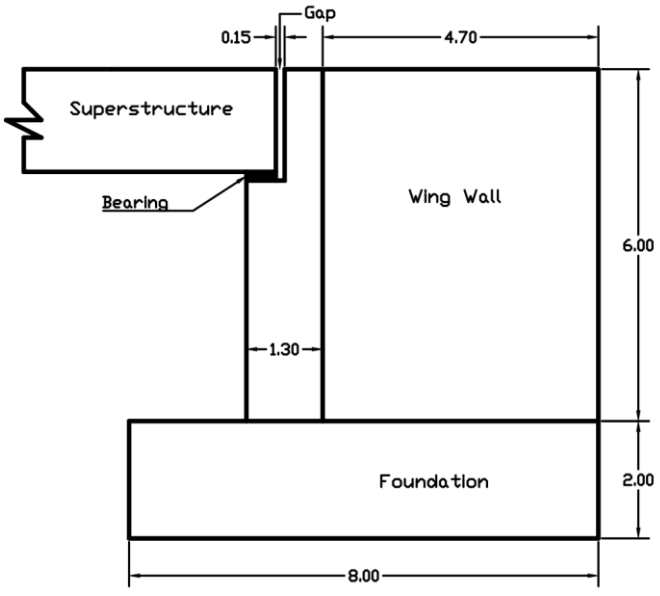

Figure 6.5. Side view of abutment.

As shown in Fig. 6.5, the superstructure is supported at abutments by elastomeric bearings placed over a seat of 0.65 m length. Moreover, an expansion joint

represented by a gap of 0.15 m length is provided to minimize damage at abutments and to enable the movement of the superstructure in longitudinal direction.

The backfill soil is modeled using linear links each of a stiffness value representing 1 m soil depth. Thus, the backfill behind the abutment wall is divided into 6 layers, and the stiffness of each soil layer is calculated based on the initial stiffness of the force-deformation relationship for passive soil pressure proposed by Duncan and Mokwa [74]. Accordingly, the soil-structure interaction at abutments is modeled in SAP2000 [75] using gap elements of a zero-gap length connected in series with the linear links to simulate the soil effect which takes place only in compression during seismic actions. Indeed, the mass of backfill soil is represented by lumped masses for each soil layer as shown in Fig. 6.6.

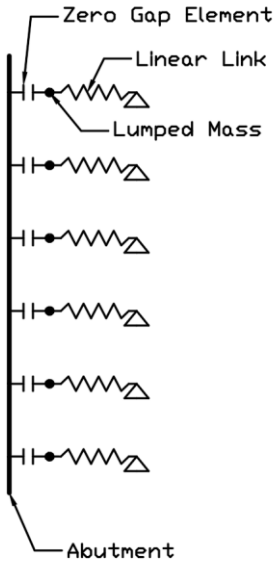

Figure 6.6. Modeling of backfill soil-structure interaction.

Bridge 1 represents a V-shaped valley bridge having two equal spans each of 15 m. The bridge is supported by a single pier of 10 m height connected to the deck monolithically.

Bridge 2 consists of 3 spans having 30 m, 40 m, and 30 m lengths, respectively. In addition to the abutments, the bridge is supported by two double-column bents such that the clear height of columns in each bent is equal to 10 m. The columns are anticipated to behave as a cantilever in the longitudinal direction and as rotationally fixed in the transverse direction due to the rigidity of the cap beam, which has dimensions of 2 m × 1.5 m.

In bridge 3, a continuous deck of 4 spans (30 m, 40 m, 40 m, 30 m) is supported by elastomeric bearings over single-column bents at A&C, and a pier with pin connection at B. As shown in Fig.6.3, piers A&C have a clear height of 8 m, where pier B has a 12 m height.

In all Bridges, the deck is modeled to move in longitudinal direction, where it is restrained in transverse direction using shear keys at abutments.

6.5.1 Determination of Performance Objectives

The considered bridges are designed to achieve two performance levels PL_1& PL_2, in which moderate damage is allowed at PL_1, and severe damage at PL_2. Accordingly, the corresponding displacement limit states are defined such as [1]:

$$d_{LS1} = d_y + \frac{1}{2}(d_u - d_y) \tag{66}$$

$$d_{LS2} = d_y + \frac{2}{3}(d_u - d_y) \tag{67}$$

where, d_{LS1} & d_{LS2} are the displacement limit states corresponding to $PL_1$and PL_2, respectively.

6.5.2 Determination of the design seismic levels

In this research study, the design seismic levels associated with performance levels PL_1& PL_2 are defined based on seismic actions of return periods T_{R1} & T_{R2} as 975 and 2475 years, respectively. Accordingly, the seismic intensities expressed in terms of peak ground accelerations PGA_1 & PGA_2 are calculated as:

$$PGA_i = PGA_{ref}\left(\frac{T_{R,ref}}{T_{Ri}}\right)^{-1/k} \quad (68)$$

where, PGA_{ref} is the peak ground acceleration associated with a predefined reference seismic level with a reference return period $T_{R,ref}$, and k is a coefficient that varies between 1.5 and 4.5 depending on the seismicity and the natural period of the structure [76]. Herein, a reference peak ground acceleration of $PGA_{ref} = 0.4\ (g)$ corresponding to a reference return period of 475 years is used, where a constant k value of 2.3 is assumed for all bridges. Consequently, the design peak ground accelerations are calculated as: $PGA_1 = 0.55\ (g)$ & $PGA_2 = 0.82\ (g)$.

After determining the seismic intensities, the bridges are designed using the smoothed spectrum obtained from group 7, which was not included in the derivation of R-factor equations. Accordingly, the used design spectrum has a corner period of 0.45 s and corresponds to soil type C.

6.5.3 Final design details

The considered bridges are designed using the proposed step-by-step performance-based seismic design procedure. To minimize errors that might be ensued from estimating the performance displacement profile, it is derived using modal nonlinear pushover analysis, which is considered one of the most accurate methods for performance displacement profile estimation. Consequently, bridges are primarily designed for the upper-performance level PL_2 corresponding for a return period of

2475 years, then the designs are checked for the lower performance level PL_1 of a 975-years return period.

The final design details of the considered bridges are presented as follows:

Bridge 1:

Bridge 1 is designed in the longitudinal direction only as it remains within the elastic range in the transverse direction. This is due to the fact that Bridge 1 is restrained in the transverse direction at abutments with a relatively rigid superstructure of 30 m length only.

The final design details of Bridge 1 is reported in Table 6.4 as follows:

Table 6.4 Design details of Bridge 1

Parameter	*Unit*	*Longitudinal*
T_n	*(s)*	*0.8*
Pier	-	*A*
Connection Type	-	*Rotationally Fixed*
H	*(m)*	*10*
D	*(m)*	*1.5*
f_c	*(MPa)*	*30*
ρ_l	-	*0.017*
η	-	*0.065*
ρ_t	-	*0.004*
k_r	-	-
d_{LS}	*(m)*	*0.17*
d_{design}	*(m)*	*0.17*
μ_{design}	-	*3.16*
R	-	*2.61*

Bridge 2:

Bridge 2 is designed in both transverse and longitudinal directions separately, where the final design corresponding to the dominant direction is adopted.

The design details of Bridge 2 is reported in Table 6.5 as follows:

Table 6.5 Design details of Bridge 2

Parameter	*Unit*	*Transverse*	*Longitudinal*
T_n	*(s)*	*0.6*	*2*
Pier	-	*A & B*	*A & B*
Connection Type	-	*Rotationally Fixed*	*Pinned*
H	*(m)*	*10*	*10*
D	*(m)*	*1.4*	*1.4*
f_c	*(MPa)*	*30*	*30*
ρ_l	-	*0.01*	*0.013*
η	-	*0.09*	*0.09*
ρ_t	-	*0.0023*	*0.003*
k_r	-	-	-
d_{LS}	*(m)*	*0.14*	*0.28*
d_{design}	*(m)*	*0.14*	*0.28*
μ_{design}	-	*2.61*	*2.41*
R	-	*2.1*	*2.9*

From Table 6.5, it is clear that the design of Bridge 2 is dominated by the longitudinal direction. Thus, the design in the longitudinal direction is considered as the final design of piers.

Bridge 3:

Bridge 3 is designed in both transverse and longitudinal directions separately, where the final design corresponding to the dominant direction is adopted.

The design details of Bridge 3 is reported in Table 6.6 as follows:

Table 6.6 Design details of Bridge 3

Parameter	*Unit*	*Transverse*		*Longitudinal*	
T_n	*(s)*	*1.1*		*1.52*	
Pier	-	*A & C*	*B*	*A & C*	*B*
Connection Type	-	*Elastomeric Bearing*	*Pinned*	*Elastomeric Bearing*	*Pinned*
H	*(m)*	*8*	*12*	*8*	*12*
D	*(m)*	*1.8*	*2*	*1.8*	*2*
f_c	*(MPa)*	*30*	*30*	*30*	*30*
ρ_l	-	*0.01*	*0.012*	*0.025*	*0.02*
η	-	*0.10*	*0.09*	*0.087*	*0.084*
ρ_t	-	*0.002*	*0.002*	*0.004*	*0.002*
k_r	-	*0.38*	-	*0.38*	-
d_{LS}	*(m)*	*0.136*	*0.23*	*0.178*	*0.24*
d_{design}	*(m)*	*0.12*	*0.23*	*0.178*	*0.2*
μ_{design}	-	*2.21*	*2.1*	*2.8*	*1.64*
R	-	*1.92*	*1.81*	*1.8*	*2.06*

Considering the performance displacement profiles in both directions, it could be noted that pier B represents the critical element in the transverse direction, whereas piers A&C are the critical elements in the longitudinal direction. However, the final design of bridge 3 is determined based on the design outputs of the longitudinal direction.

6.5.4 Verification of Bridge Designs

The designs obtained by implementing the proposed performance-based seismic design procedure in the previous section are verified by performing NTHA using SAP2000 [75]. In Fig 6.7-6.8, the design tip displacements of the considered bridges are compared with those obtained by NTHA in both transverse and longitudinal directions, respectively.

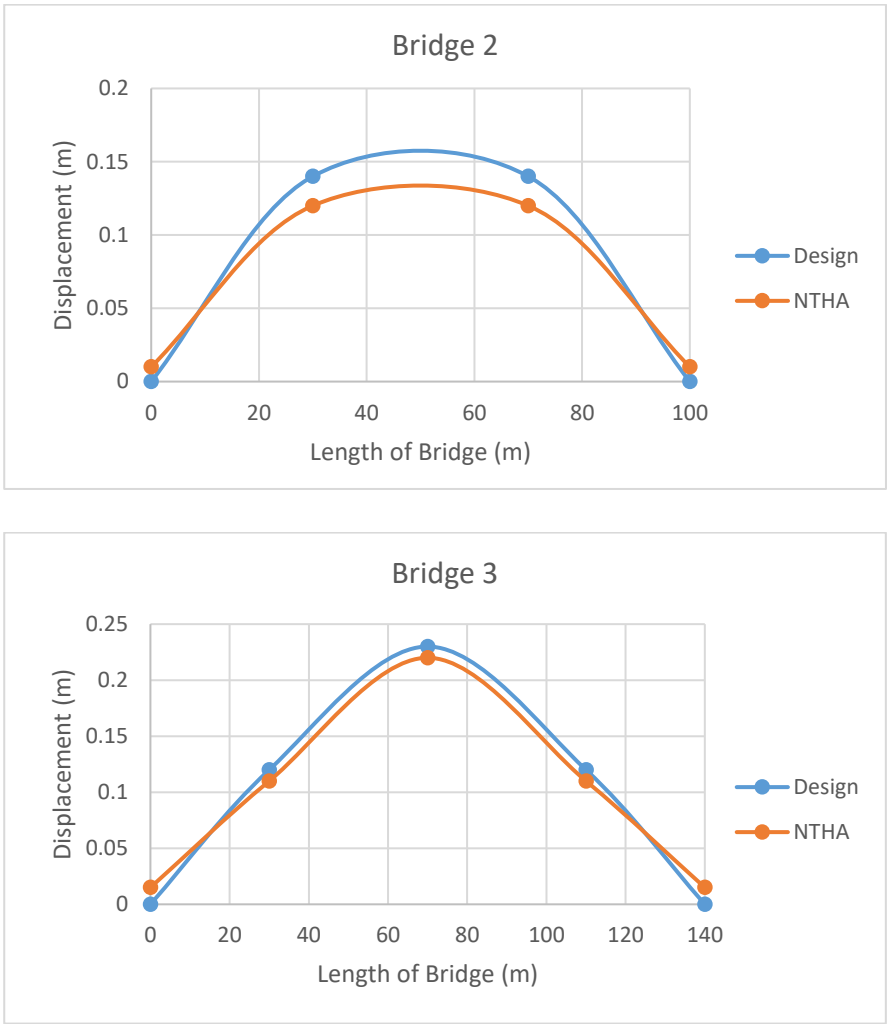

Figure 6.7. Comparison between design tip displacements and averaged tip displacements of piers from NTHA corresponding to the upper performance level in transverse direction.

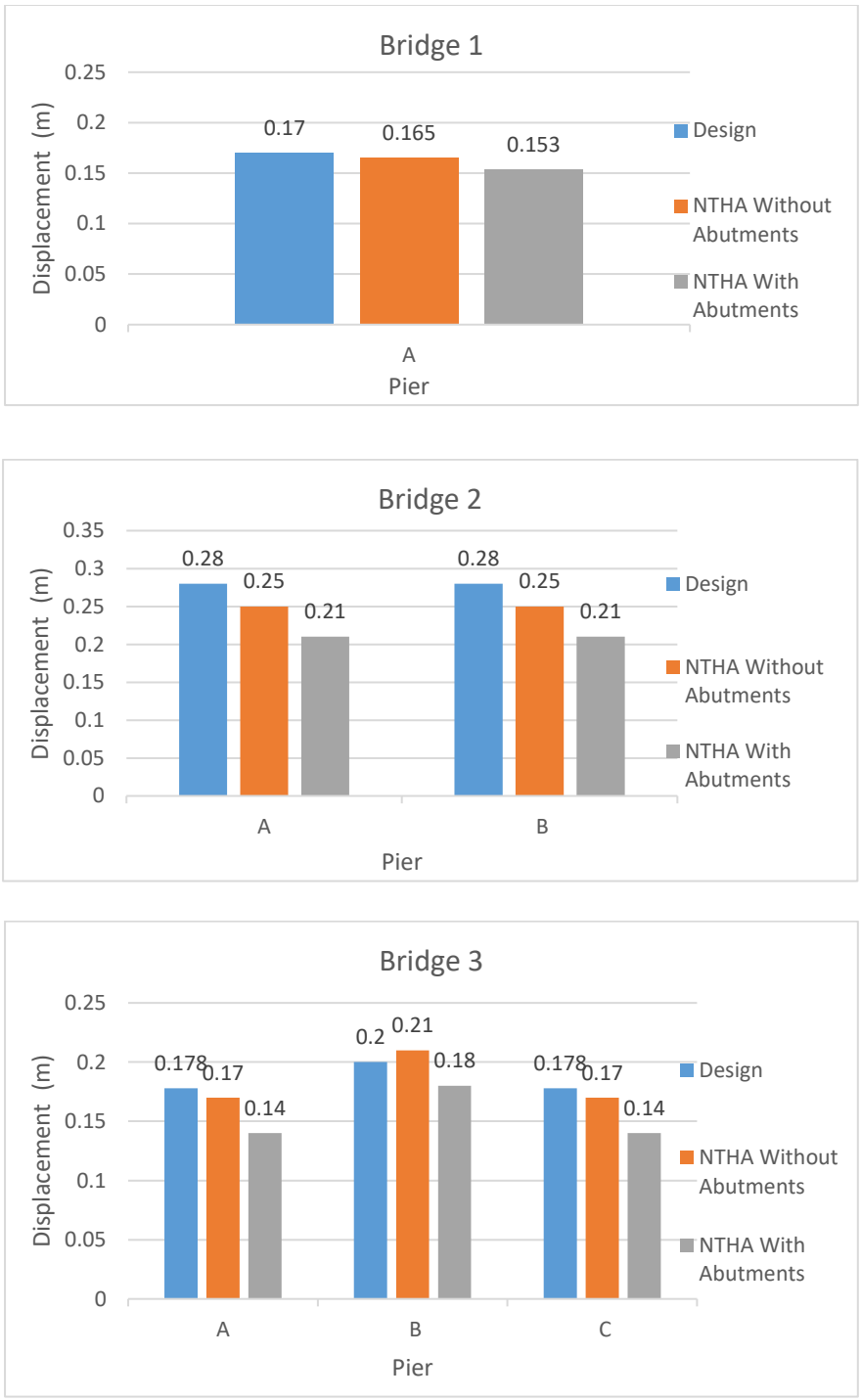

Figure 6.8. Comparison between design tip displacements and averaged tip displacements of piers from NTHA corresponding to the upper-performance level in longitudinal direction.

In Fig. 6.7, the resulted tip displacements of piers from NTHA procedure, which is considered as an accurate procedure to estimate the actual seismic response of structures, are compared with the design tip displacements in transverse direction.

For Bridge 2, more conservative results are obtained from NTHA compared to those obtained for bridge 3. This is simply ascribed to the restraining effect of abutments in transverse direction, which significantly takes place in bridges of shorter continuous superstructures. In bridge 3, compared to the design tip displacements of piers, almost identical but also conservative values are obtained from NTHA.

In Fig. 6.8, the design tip displacements of Bridges 1-3 in longitudinal direction are compared with the values obtained from NTHA. Moreover, the effect of abutments in longitudinal direction is investigated by performing NTHA for bridge models with and without abutments. For bridge models in which abutments are included, a significant effect of abutments could be noticed, especially for the bridges designed to undergo displacements relatively much larger than the expansion joint length. For example, the piers of Bridge 2 are designed to have tip displacements of 0.28 m, which is significantly larger than the provided expansion joint length (0.15 m for all cases). However, the obtained tip displacements of piers from NTHA in bridge 2 modeled including abutments are equal to 0.21 m, which is far less than the design displacements. On the other hand, the demand tip displacements of piers obtained from NTHA for the same bridge modeled without abutments show larger values that are closer to the design displacements.

Although the same trend is observed from the displacement results of Bridges 1&3 presented in Fig. 6.8, limited effect of abutments is found as the seismic forces in these bridges are mainly resisted by piers rather than abutments, enabling the bridges to undergo displacement close to the design values.

Considering the results of the designed bridges, it could be concluded that the proposed performance-based seismic design procedure provides acceptable designs for all the designed bridge piers, which are anticipated to resist seismic forces considering predefined performance objectives. However, more conservative

designs are obtained for bridges in which significant seismic forces are resisted by abutments, resulting in lower damage levels at piers.

CHAPTER 7

CONCLUSIONS

In this thesis, a new methodology to estimate strength reduction factors for performance-based seismic design of RC bridges is presented. The presented methodology is developed by modeling bridge piers as single degree of freedom (SDOF) systems with a lumped mass representing the arbitrary mass of superstructure. Bridge piers are classified according to their substructure-superstructure connection into three types such as pinned, rotationally fixed, and elastomeric bearing connected piers. The strength reduction factors (R-factor) of the SDOF systems are evaluated by performing linear 5%-damped response spectrum analyses (RSA) and nonlinear time history analyses (NTHA) for both circular and rectangular sections considering wide ranges of design parameters. Moreover, the SDOF systems are analyzed using a suite of far-fault ground motions acquired from PEER database [10]. The acquired ground motions are grouped according to their PGA/PGV ratios into ten groups. The smoothed average spectra of these groups are obtained and used as design spectra in the RSA and NTHA. As the PGA/PGV ratio is not usually used as a design parameter in engineering practice, it is correlated to the second corner period of the design spectrum using the relationship proposed in [49]. Therefore, the design parameters anticipated to have significant effects on the seismic response of bridge piers are investigated, and their possible ranges are determined considering the limits existing in design codes.

In this study, the R-factor is calculated as the ratio of the elastic demand force to the yield strength capacity of piers. Thus, the yield moment and curvature capacities of the considered piers are determined by developing a moment-curvature program via OpenSees software [12]. Accordingly, parametric moment-curvature analyses are performed for the adopted ranges of the sectional parameters and the corresponding idealized moment-curvature relationships are obtained.

In the performed sectional analyses, the Mander model [13] is used to simulate the concrete behavior, and a simplified trilinear stress-strain relationship is used for the reinforcing steel. Consequently, the effects of the considered sectional parameters on the yield curvature, ultimate curvature, and yield moment capacities are investigated. The results show a significant effect of section depth on the yield curvature of circular and rectangular sections. Fewer effects of longitudinal reinforcements, axial load, and concrete strength are observed on the yield curvature for both section types. Indeed, insignificant effect of the transverse reinforcements on the yield curvature and yield moment capacities is noticed. It is found that the ultimate curvature is greatly influenced by section depth and transverse reinforcements, where it is less affected by the longitudinal reinforcements and axial load. From the resulted data, a set of equations to estimate the yield curvature, ultimate curvature, and yield moment capacities of RC sections is proposed. Such equations are used in the seismic design and assessment of bridges to calculate the displacement and strength capacities of piers.

Afterwards, the R-factors corresponding for the considered SDOF systems are obtained by performing RSA using the design spectra. Then, the nonlinear responses of the systems are simulated by performing NTHA to obtain the corresponding demand displacements. In the NTHA, the nonlinear behavior is simulated by assigning plastic hinges at specific locations expected to undergo plastic deformations along the pier height. The assigned plastic hinges are defined based on the idealized moment-curvature relationships obtained from the sectional analyses. Moreover, the pinching IMK hysteretic model [11] is used to simulate the cyclic behavior of piers considering various failure modes such as shear, shear-flexure, and flexure failure mode. To investigate the effects of the design parameters on R-factor, a sensitivity analysis of R-factor for a sample SDOF systems is performed. The sensitivity analysis indicated no effect of the transverse reinforcements on R-factor. However, very limited effect of transverse reinforcements on the resulted demand displacements is noticed due to the effect of transverse reinforcements on the post-yield stiffness. Therefore, the transverse reinforcements ratio is excluded from the

parameters used in R-factor derivation. Indeed, the analyzed SDOF systems are adjusted to have bilinear moment-curvature relationships having an average post-yield stiffness.

Next, parametric RSA and NTHA of the SDOF systems are performed on high-performance computer machines using parallel computation techniques, and the corresponding R-factor as well as the maximum tip displacements values are obtained. As a result of the performed parametric analyses, a total of 9 huge data sets are structured and mined to eliminate unrealistic values. Subsequently, 9 R-factor equations are derived by performing multiple regression analyses on the obtained data sets. In addition to the design parameters affecting the strength reduction factor, the R-factor equations are expressed by including the average maximum displacement of each group resulted from the NTHA. To investigate the accuracy of the proposed R-factor equations, error performance analyses are performed by comparing the actual R-factor values of the SDOF systems with those calculated using the proposed equations. The results show excellent accuracy of the proposed R-factor equations as the mean error values are very closed to zero in all the analyzed data sets. Moreover, acceptable error standard deviations varying between 10.35% and 14.31% are obtained for the analyzed data.

Based on the proposed equations in this thesis, a new performance-based seismic design procedure for bridges is presented. The presented procedure mainly depends on the strength reduction factor estimated by assuming initial values of the design parameters for bridge piers. The step-by-step design procedure is iterated till the appropriate design achieving the desired performance objective is reached. The proposed procedure is simple and could be implemented using simple 5%-damped response spectrum analysis. Moreover, it enables designers to have optimal seismic designs of bridges corresponding to multi-performance levels.

The proposed design procedure is implemented for three bridges of various configurations. To describe the implementation of the procedure in both directions, the designs of the considered bridges are obtained in transverse and longitudinal

directions separately. Consequently, the final designs of both directions are verified by performing NTHA. Indeed, the soil-structure interaction effect at abutments is investigated by performing the NTHA for bridges with and without abutments. As a result, the designed bridges showed acceptable performance satisfying the design performance levels. The results of the NTHA indicated a significant effect of abutments on the resultant displacements for the bridges expected to undergo displacements relatively much larger than the provided expansion joints resulting in less damage at piers.

Although the proposed design procedure shows good reliability for the bridges presented in this thesis, the application of this procedure should be investigated on bridges in which irregularities due to the relative stiffness of piers and redistribution of seismic forces take place.

REFERENCES

[1] Priestley M.J.N., M. C. Calvi, and M. J. Kowalsky, *Displacement-Based Seismic Design of Structures*. Pavia: IUSS Press, 2007.

[2] A. Ghobarah, "Performance-based design in earthquake engineering: state of development," 2001. [Online]. Available: www.elsevier.com/locate/engstruct

[3] Q. Zhang and M. S. Alam, "Performance-based seismic design of bridges: a global perspective and critical review of past, present and future directions," *Structure and Infrastructure Engineering*, vol. 15, no. 4, pp. 539–554, Apr. 2019, doi: 10.1080/15732479.2018.1558269.

[4] "Mackie, K. R., & Stojadinovi_c, B. (2005). Fragility basis for California highway overpass bridge seismic decision making (Report No. 2005/ 02). Berkeley, CA: University of California Berkeley, Pacific Earthquake Engineering Research Center."

[5] R. D. Bertero and V. v. Bertero, "Performance-based seismic engineering: The need for a reliable conceptual comprehensive approach," *Earthquake Engineering and Structural Dynamics*, vol. 31, no. 3, pp. 627–652, 2002, doi: 10.1002/eqe.146.

[6] "AASHTO LRFD bridge design specifications." American Association of State Highway and Transportation Officials, Washington, D.C, 2014.

[7] "Eurocode 8–design of Structures for earthquake resistance." Brussels, 2005.

[8] "ASCE 7-16 Minimum Design Loads and Associated Criteria for Buildings and Other Structures." American Society of Civil Engineers New York, NY, 2016.

[9] E. Miranda and V. v. Bertero, “Evaluation of Strength Reduction Factors for Earthquake-Resistant Design,” *Earthquake Spectra*, vol. 10, no. 2, pp. 357–379, May 1994, doi: 10.1193/1.1585778.

[10] “Pacific Earthquake Engineering Research Center. PEER Strong Motion Database.” [Online]. Available: https://ngawest2.berkeley.edu/spectras/new

[11] L. F. Ibarra, R. A. Medina, and H. Krawinkler, “Hysteretic models that incorporate strength and stiffness deterioration,” *Earthquake Engineering and Structural Dynamics*, vol. 34, no. 12, 2005, doi: 10.1002/eqe.495.

[12] F. McKenna, G. L. Fenves, and M. H. Scott, “Open System for Earthquake Engineering Simulation (OpenSees).” University of California, Berkeley, 2000. [Online]. Available: http://opensees.berkeley.edu

[13] J. B. Mander, M. J. N. Priestley, and R. Park, “Theoretical Stress-Strain Model for Confined Concrete,” *Journal of Structural Engineering*, vol. 114, no. 8, 1988, doi: 10.1061/(asce)0733-9445(1988)114:8(1804).

[14] E. Hernández-Montes and M. Aschleim, “Estimates of the yield curvature for design of reinforced concrete columns,” *Magazine of Concrete Research*, vol. 55, no. 4, 2003, doi: 10.1680/macr.2003.55.4.373.

[15] M. N. Sheikh, H. H. Tsang, T. J. McCarthy, and N. T. K. Lam, “Yield curvature for seismic design of circular reinforced concrete columns,” *Magazine of Concrete Research*, vol. 62, no. 10, 2010, doi: 10.1680/macr.2010.62.10.741.

[16] M. J. N. Priestley, “PERFORMANCE BASED SEISMIC DESIGN,” *Bulletin of the New Zealand society for earthquake engineering*, vol. 33, no. 3, pp. 325–346, 2000.

[17] N. Newmark and W. Hall, “Seismic Design Criteria for Nuclear Reactor Facilities,” *Report No.46*. Building Practice for Disaster Mitigation, National Bureau of Standards, U.S. Department of Commerce, pp. 209–236, 1973.

[18] C.-H. Zhai and L.-L. Xie, “Study on strength reduction factors consid-ering the effect of classification of design earthquake,” *Acta Seismologica Sinica*, vol. 19, no. 3, pp. 299–310, 2006.

[19] A. Nassar and Krawinkler H, “Seismic Demands for SDOD and MDOF Systems,” California, USA, 1991.

[20] E. Miranda, “SITE-DEPENDENT STRENGTH-REDUCTION FACTORS,” *Journal of Structural Engineering*, vol. 119, no. 12, pp. 3503–3519, 1993.

[21] R. Riddell and N. M. Newmark, “Statistical analysis of the response of nonlinear systems subjected to earthquakes,” *Structural research Series No. 468*. Dept. of Civ. Engrg. University of Illinois, Urbana, pp. 54–65, 1979.

[22] G. D. Hatzigeorgiou, “Behavior factors for nonlinear structures subjected to multiple near-fault earthquakes,” *Computers and Structures*, vol. 88, no. 5–6, pp. 309–321, Mar. 2010, doi: 10.1016/j.compstruc.2009.11.006.

[23] H. Qu, J. Zhang, and J. X. Zhao, “Strength reduction factors for seismic analyses of buildings exposed to near-fault ground motions,” *Earthquake Engineering and Engineering Vibration*, vol. 10, no. 2, pp. 195–209, Jun. 2011, doi: 10.1007/s11803-011-0058-0.

[24] T. Vidic, P. Fajfar, and M. Fischinger, “Consistent inelastic design spectra: strength and displacement,” *Earthquake Engineering & Structural Dynamics*, vol. 23, no. 5, pp. 507–521, 1994.

[25] I. Cuesta and M. A. Aschheim, “Isoductile strengths and strength reduction factors of elasto-plastic SDOF system subjected to simple waveforms,” *Earthquake Engineering and Structural Dynamics*, vol. 30, no. 7, pp. 1043–1059, 2001, doi: 10.1002/eqe.51.

[26] Y. F. Wu, H. Wang, A. Q. Li, B. Sha, and K. M. Bi, “The Strength Reduction Factors for Seismic-Isolated Bridges Characterized by SDOF Bilinear

Systems in Far-Fault Areas," *Journal of Earthquake Engineering*, vol. 23, no. 3, pp. 404–421, Mar. 2019, doi: 10.1080/13632469.2017.1326425.

[27] Y. Zhang, J. Chen, and C. Sun, "Damage-based strength reduction factor for nonlinear structures subjected to sequence-type ground motions," *Soil Dynamics and Earthquake Engineering*, vol. 92, pp. 298–311, Jan. 2017, doi: 10.1016/j.soildyn.2016.10.002.

[28] M. Zerbin, A. Aprile, K. Beyer, and E. Spacone, "Ductility reduction factor formulations for seismic design of RC wall and frame structures," *Engineering Structures*, vol. 178, pp. 102–115, Jan. 2019, doi: 10.1016/j.engstruct.2018.10.020.

[29] A. J. Kappos, T. S. Paraskeva, and I. F. Moschonas, "Response Modification Factors for Concrete Bridges in Europe," *Journal of Bridge Engineering*, vol. 18, no. 12, pp. 1328–1335, Dec. 2013, doi: 10.1061/(asce)be.1943-5592.0000487.

[30] "SEAOC. Vision 2000, Performance based seismic engineering of buildings, vols. I and II: Conceptual framework. Sacramento (CA):," 1995.

[31] "ATC 40, Seismic evaluation and retrofit of existing concrete buildings. Redwood City (CA): Applied Technology Council, 1996."

[32] "FEMA 273, NEHRP guidelines for the seismic rehabilitation of buildings; FEMA 274, Commentary. Washington (DC): Federal Emergency Management Agency, 1996." [Online]. Available: http://www.springer.com/series/6011

[33] M. J. N. Priestley, "Myths and fallacies in earthquake engineering," *Bulletin of the New Zealand Society for Earthquake Engineering*, vol. 26, no. 3, pp. 329–341, 1993.

[34] M. J. N. Priestley, “Myths and Fallacies in Earthquake Engineering, Revisited: The Ninth Mallet Milne Lecture, 2003.” IUSS Press, Pavia, Italy, 2003.

[35] M. J. Kowalsky, M. J. N. Priestley, and G. A. Macrae, “Displacement-based design of RC bridge columns in seismic regions,” *Earthquake engineering & structural dynamics*, vol. 24, no. 12, pp. 1623–1643, 1995.

[36] G. M. Calvi and G. R. Kingsley, “Displacement-based seismic design of multi-degree-of-freedom bridge structures,” *Earthquake engineering & structural dynamics*, vol. 24, no. 9, pp. 1247–1266, 1995.

[37] M. J. Kowalsky, “A displacement-based approach for the seismic design of continuous concrete bridges,” *Earthquake Engineering and Structural Dynamics*, vol. 31, no. 3, pp. 719–747, 2002, doi: 10.1002/eqe.150.

[38] H. Dwairi and M. Kowalsky, “Implementation of inelastic displacement patterns in direct displacement-based design of continuous bridge structures,” *Earthquake Spectra*, vol. 22, no. 3, pp. 631–662, Aug. 2006, doi: 10.1193/1.2220577.

[39] V. Suarez and M. J. Kowalsky, “Displacement-based seismic design of drilled shaft bents with soil-structure interaction,” *Journal of Earthquake Engineering*, vol. 11, no. 6, pp. 1010–1030, Nov. 2007, doi: 10.1080/13632460701232683.

[40] V. A. Suarez and M. J. Kowalsky, “Direct Displacement-Based Design as an Alternative Method for Seismic Design of Bridges,” *Special Publication, 271*. pp. 63–78, 2010.

[41] V. A. Suarez and M. J. Kowalsky, “A stability-based target displacement for direct displacement-based design of bridge Piers,” *Journal of Earthquake Engineering*, vol. 15, no. 5, pp. 754–774, Jun. 2011, doi: 10.1080/13632469.2010.534233.

[42] V. G. Bardakis and M. N. Fardis, “A displacement-based seismic design procedure for concrete bridges having deck integral with the piers,” *Bulletin of Earthquake Engineering*, vol. 9, no. 2, pp. 537–560, Apr. 2011, doi: 10.1007/s10518-010-9215-5.

[43] D. Biskinis and M. N. Fardis, “Deformations at flexural yielding of members with continuous or lap-spliced bars,” *Structural concrete*, vol. 11, no. 3, pp. 127–138, 2010.

[44] K. I. Gkatzogias, “Performance-based seismic design of concrete bridges for deformation control through advanced analysis tools and control devices,” Doctoral dissertation, City, Universtiy of London, 2017.

[45] A. J. Kappos, I. G. Gidaris, and K. I. Gkatzogias, “Problems associated with direct displacement-based design of concrete bridges with single-column piers, and some suggested improvements,” *Bulletin of Earthquake Engineering*, vol. 10, no. 4, pp. 1237–1266, Aug. 2012, doi: 10.1007/s10518-012-9354-y.

[46] “CSA Canadian highway bridge design code.” Canadian Standards Association, Mississauga, 2014.

[47] “NZT New Zealand bridge manual .” Transit New Zealand, Wellington, 2016.

[48] “TKDY Turkish seismic design code for bridges.” 2020.

[49] M. Dicleli and A. G. Görgülü, “Proposed minimum restoring force requirements for seismic isolated structures,” *Engineering Structures*, vol. 228, Feb. 2021, doi: 10.1016/j.engstruct.2020.111549.

[50] M. Dicleli and S. Buddaram, “Comprehensive evaluation of equivalent linear analysis method for seismic-isolated structures represented by sdof systems,” *Engineering Structures*, vol. 29, no. 8, pp. 1653–1663, Aug. 2007, doi: 10.1016/j.engstruct.2006.09.013.

[51] M. Grigoriu, “To Scale or Not to Scale Seismic Ground-Acceleration Records,” *Journal of Engineering Mechanics*, vol. 137, no. 4, pp. 284–293, Apr. 2011, doi: 10.1061/(asce)em.1943-7889.0000226.

[52] R. Park and T. Paulay, *Reinforced Concrete Structures*. New York: John Wiley & Sons, 1975.

[53] M. Priestley, G. Ranzo, G. Benzoni, and M. Kowalsky, “Yield displacement of circular bridge columns,” *Proceedings of the 4th Caltrans Seismic Research Workshop, California Department of Transportation, Sacramento*. 1996.

[54] D. E. Lehman and J. P. Moehle, *Seismic performance of well-confined concrete bridge columns*. University of California, Berkeley, 1998.

[55] Panagiotakos TB and Fardis MN, “Deformation of reinforced concrete members at yielding and ultimate,” *ACI Structural Journal*, vol. 98, no. 2, pp. 135–48, 2001.

[56] M. N. Fardis and D. E. Biskinis, “Deformation capacity of RC members as controlled by flexure or shear.” In Otani Symposium (Vol. 511530), 2003.

[57] S. Grammatikou, D. Biskinis, and M. N. Fardis, “Ultimate Strain Criteria for RC Members in Monotonic or Cyclic Flexure,” *Journal of Structural Engineering*, vol. 142, no. 9, 2016, doi: 10.1061/(asce)st.1943-541x.0001501.

[58] B. Ganjavi and H. Hao, “Strength reduction factor for MDOF soil-structure systems,” *Structural Design of Tall and Special Buildings*, vol. 23, no. 3, 2014, doi: 10.1002/tal.1022.

[59] Z. Wang, J. Wang, J. Zhu, and J. Zhang, “A simplified method to assess seismic behavior of reinforced concrete columns,” *Structural Concrete*, vol. 21, no. 1, 2020, doi: 10.1002/suco.201800223.

[60] H. Abdi and L. J. Williams, “Principal component analysis,” *Wiley interdisciplinary reviews: computational statistics*, vol. 2, no. 4, pp. 433–459, 2010.

[61] M. J. Kowalsky, “Deformation limit states for circular reinforced concrete bridge columns,” *Journal of Structural Engineering*, vol. 126, no. 8, pp. 869–878, 2000.

[62] D. Lehman, M. Asce, ; Jack Moehle, S. Mahin, ; Anthony Calderone, and L. Henry, “Experimental Evaluation of the Seismic Performance of Reinforced Concrete Bridge Columns”, doi: 10.1061/ASCE0733-94452004130:6869.

[63] A. H. M. M. Billah and M. S. Alam, “Performance-Based Seismic Design of Shape Memory Alloy–Reinforced Concrete Bridge Piers. I: Development of Performance-Based Damage States,” *Journal of Structural Engineering*, vol. 142, no. 12, p. 04016140, Dec. 2016, doi: 10.1061/(asce)st.1943-541x.0001458.

[64] M. N. Priestley and F. Seible, “Seismic design and retrofit of bridges.” John Wiley & Sons, 1996.

[65] H. Hwang, J. B. Liu, and Y.-H. Chiu, “Seismic Fragility Analysis of Highway Bridges.” Mid-America Earthquake Center CD Release 01-06, 2001.

[66] “SCDOT The South Carolina Department of Transportation seismic design specifications for highway bridges (Specifications).” SC: Department of Transportation, Columbia, 2008.

[67] A. J. Kappos, K. I. Gkatzogias, and I. G. Gidaris, “Extension of direct displacement-based design methodology for bridges to account for higher mode effects,” *Earthquake Engineering and Structural Dynamics*, vol. 42, no. 4, pp. 581–602, Apr. 2013, doi: 10.1002/eqe.2229.

[68] S. Antoniou and R. Pinho, “Development and verification of a displacement-based adaptive pushover procedure,” *Journal of Earthquake Engineering*, vol. 8, no. 5, pp. 643–661, 2004, doi: 10.1080/13632460409350504.

[69] A. J. Kappos, T. S. Paraskeva, and A. G. Sextos, “Modal pushover analysis as a means for the seismic assessment of bridge structures.” In Proc. of the 4th European Workshop on the Seismic Behaviour of Irregular and Complex Structures, pp. 26–27, 2005.

[70] F. Alfawakhiri and M. Bruneau, “Flexibility of superstructures and supports in the seismic analysis of simple bridges,” *Earthquake engineering & structural dynamics*, vol. 29, no. 5, pp. 711–729, 2000.

[71] G. M. Calvi and T. Sullivan, “A model code for the displacement based seismic design of structures: DBD09 draft subject to public enquiry.” Iuss Press, 2009.

[72] V. A. Suarez, “Implementation of direct displacement based design for highway bridges.” North Carolina State University, 2008.

[73] D. Cardone, “Displacement limits and performance displacement profiles in support of direct displacement-based seismic assessment of bridges,” *Earthquake Engineering and Structural Dynamics*, vol. 43, no. 8, pp. 1239–1263, Jul. 2014, doi: 10.1002/eqe.2396.

[74] J. M. Duncan and R. L. Mokwa, “Passive earth pressures: theories and tests,” *Journal of Geotechnical and Geoenvironmental Engineering*, vol. 127, no. 3, pp. 248–257, 2001.

[75] “SAP 2000 V.23 Computers and Structures INC.” Berkeley, CA, USA, 2021.

[76] G. Weatherill, H. Crowley, and L. Danciu, “Preliminary reference Euro-Mediterranean seismic hazard zonation.” Zürich, CH: Swiss Seismological Service. Seismic Hazard Harmonization in Europe (SHARE), 2013.

APPENDICES

A. Selected Ground Motions

Table A.1 Selected Ground Motions

Group #	EQ #	RSN	Event	Mg	Fault Mechanism	Rrup (km)	Vs30 (m/s)	PGA/PGV (1/s)
Group 1	1	36	Borrego Mtn	6.6	strike slip	45.7	213	4.9
	2	3758	Landers	7.3	strike slip	36.9	334	4.9
	3	2702	Chi-Chi, Taiwan-04	6.2	strike slip	54.5	210	4.9
	4	6036	El Mayor-Cucapah, Mexico	7.2	strike slip	58.5	309	5.0
	5	4462	L'Aquila, Italy	6.3	Normal	26.9	199	5.1
	6	2898	Chi-Chi, Taiwan-04	6.2	strike slip	53.1	224	5.1
	7	2744	Chi-Chi, Taiwan-04	6.2	strike slip	48.4	319	5.3
	8	1149	Kocaeli, Turkey	7.5	strike slip	58.3	310	5.3
	9	6912	Darfield, New Zealand	7	strike slip	25.4	206	5.5
	10	8487	Parkfield-02, CA	6	strike slip	29.4	308	5.6
	11	6005	El Mayor-Cucapah, Mexico	7.2	strike slip	36.5	203	5.6

Table A.1 Selected Ground Motions (continued)

Group #	EQ #	RSN	Event	Mg	Fault Mechanism	Rrup (km)	Vs30 (m/s)	PGA/PGV (1/s)
Group 2	12	5832	El Mayor-Cucapah, Mexico	7.2	strike slip	26.6	242	5.8
	13	447	Morgan Hill	6.2	strike slip	24.5	240	5.9
	14	5859	El Mayor-Cucapah, Mexico	7.2	strike slip	42.6	194	6.3
	15	5988	El Mayor-Cucapah, Mexico	7.2	strike slip	30.6	196	6.5
	16	931	Big Bear-01	6.5	strike slip	35.2	297	6.6
	17	2857	Chi-Chi, Taiwan-04	6.2	strike slip	56.1	350	6.6
	18	1144	Gulf of Aqaba	7.2	strike slip	44.1	355	6.6
	19	6953	Darfield, New Zealand	7	strike slip	24.6	206	6.6
	20	2891	Chi-Chi, Taiwan-04	6.2	strike slip	54.9	222	6.6
	21	2694	Chi-Chi, Taiwan-04	6.2	strike slip	50	229	6.8
	22	884	Landers	7.3	strike slip	36.2	312	6.9

Table A.1 Selected Ground Motions (continued)

Group #	EQ #	RSN	Event	Mg	Fault Mechanism	Rrup (km)	Vs30 (m/s)	PGA/PGV (1/s)
Group 3	23	8492	El Mayor-Cucapah, Mexico	7.2	strike slip	58	191	7.0
	24	176	Imperial Valley-06	6.5	strike slip	22	250	7.2
	25	6965	Darfield, New Zealand	7	strike slip	24.3	263	7.2
	26	1121	Kobe, Japan	6.9	strike slip	27.8	256	7.3
	27	2900	Chi-Chi, Taiwan-04	6.2	strike slip	56.4	240	7.4
	28	5969	El Mayor-Cucapah, Mexico	7.2	strike slip	32.9	223	7.5
	29	6988	Darfield, New Zealand	7	strike slip	26.9	344	7.6
	30	1177	Kocaeli, Turkey	7.5	strike slip	53.9	342	7.6
	31	6013	El Mayor-Cucapah, Mexico	7.2	strike slip	28.3	276	7.7
	32	1110	Kobe, Japan	6.9	strike slip	24.8	256	7.8
	33	6896	Darfield, New Zealand	7	strike slip	32.9	280	7.8

Table A.1 Selected Ground Motions (continued)

Group #	EQ #	RSN	Event	Mg	Fault Mechanism	Rrup (km)	Vs30 (m/s)	PGA/PGV (1/s)
Group 4	34	2752	Chi-Chi, Taiwan-04	6.2	strike slip	21.7	259	7.9
	35	163	Imperial Valley-06	6.5	strike slip	24.6	206	8.1
	36	464	Morgan Hill	6.2	strike slip	26.4	216	8.1
	37	3754	Landers	7.3	strike slip	48.8	292	8.4
	38	850	Landers	7.3	strike slip	21.8	359	8.6
	39	169	Imperial Valley-06	6.5	strike slip	22	242	8.8
	40	6923	Darfield, New Zealand	7	strike slip	30.5	255	8.8
	41	1776	Hector Mine	7.1	strike slip	56.4	359	8.8
	42	186	Imperial Valley-06	6.5	strike slip	36.9	212	8.8
	43	166	Imperial Valley-06	6.5	strike slip	50.1	336	8.9
	44	5838	El Mayor-Cucapah, Mexico	7.2	strike slip	29	186	8.9

Table A.1 Selected Ground Motions (continued)

Group #	EQ #	RSN	Event	Mg	Fault Mechanism	Rrup (km)	Vs30 (m/s)	PGA/PGV (1/s)
Group 5	45	2111	Denali, Alaska	7.9	strike slip	43	342	9.1
	46	462	Morgan Hill	6.2	strike slip	30.8	199	9.1
	47	8160	El Mayor-Cucapah, Mexico	7.2	strike slip	35.5	209	9.2
	48	1115	Kobe, Japan	6.9	strike slip	28.1	256	9.4
	49	4054	Bam, Iran	6.6	strike slip	46.2	575	9.5
	50	1160	Kocaeli, Turkey	7.5	strike slip	55.5	387	9.6
	51	910	Big Bear-01	6.5	strike slip	41.9	379	9.7
	52	2697	Chi-Chi, Taiwan-04	6.2	strike slip	54.5	498	9.8
	53	926	Big Bear-01	6.5	strike slip	59.8	390	10.1
	54	2743	Chi-Chi, Taiwan-04	6.2	strike slip	38.4	505	10.1
	55	1128	Kozani, Greece-01	6.4	Normal	57.3	491	10.2

Table A.1 Selected Ground Motions (continued)

Group #	EQ #	RSN	Event	Mg	Fault Mechanism	Rrup (km)	Vs30 (m/s)	PGA/PGV (1/s)
Group 6	56	472	Morgan Hill	6.2	strike slip	31.9	544	10.2
	57	4487	L'Aquila, Italy	6.3	Normal	49.1	575	10.2
	58	1626	Sitka, Alaska	7.7	strike slip	34.6	650	10.3
	59	6060	Big Bear-01	6.5	strike slip	41.9	368	10.85
	60	2785	Chi-Chi, Taiwan-04	6.2	strike slip	51.8	470	10.5
	61	2788	Chi-Chi, Taiwan-04	6.2	strike slip	49.8	485	10.5
	62	1128	Kozani, Greece-01	6.4	Normal	57.3	491	10.8
	63	3752	Landers	7.3	strike slip	45.3	436	10.7
	64	6949	Darfield, New Zealand	7	strike slip	53.8	551	10.7
	65	4487	L'Aquila, Italy	6.3	Normal	49.1	575	10.8
	66	299	Irpinia, Italy-02	6.2	Normal	42.7	561	10.8

Table A.1 Selected Ground Motions (continued)

Group #	EQ #	RSN	Event	Mg	Fault Mechanism	Rrup (km)	Vs30 (m/s)	PGA/PGV (1/s)
Group 7	67	2787	Chi-Chi, Taiwan-04	6.2	strike slip	50.1	460	10.8
	68	471	Morgan Hill	6.2	strike slip	31.9	544	10.9
	69	4491	L'Aquila, Italy	6.3	Normal	37.2	388	10.9
	70	2717	Chi-Chi, Taiwan-04	6.2	strike slip	45.4	573	11.0
	71	283	Irpinia, Italy-01	6.9	Normal	52.9	613	11.2
	72	5830	El Mayor-Cucapah, Mexico	7.2	strike slip	45.5	524	11.3
	73	2738	Chi-Chi, Taiwan-04	6.2	strike slip	50.3	573	11.4
	74	6875	Joshua Tree, CA	6.1	strike slip	22.3	396	11.4
	75	1619	Duzce, Turkey	7.1	strike slip	34.3	535	11.5
	76	291	Irpinia, Italy-01	6.9	Normal	30.1	575	11.5
	77	2712	Chi-Chi, Taiwan-04	6.2	strike slip	34.1	665	11.6

Table A.1 Selected Ground Motions (continued)

Group #	EQ #	RSN	Event	Mg	Fault Mechanism	Rrup (km)	Vs30 (m/s)	PGA/PGV (1/s)
Group 8	78	4503	L'Aquila, Italy	6.3	Normal	39.1	613	12.0
	79	450	Morgan Hill	6.2	strike slip	23.2	462	12.0
	80	3759	Landers	7.3	strike slip	27.1	425	12.3
	81	4351	Umbria Marche, Italy	6	Normal	25.2	437	12.6
	82	293	Irpinia, Italy-01	6.9	Normal	59.6	593	12.6
	83	891	Landers	7.3	strike slip	50.9	659	13.0
	84	4086	Parkfield-02, CA	6	strike slip	43.4	411	13.1
	85	8163	El Mayor-Cucapah, Mexico	7.2	strike slip	57.5	483	13.1
	86	1125	Kozani, Greece-01	6.4	Normal	49.7	579	13.1
	87	6915	Darfield, New Zealand	7	strike slip	24.5	422	13.4
	88	2107	Denali, Alaska	7.9	strike slip	50.9	399	13.5

Table A.1 Selected Ground Motions (continued)

Group #	EQ #	RSN	Event	Mg	Fault Mechanism	Rrup (km)	Vs30 (m/s)	PGA/PGV (1/s)
Group 9	89	6057	Big Bear-01	6.5	strike slip	26.5	362	13.5
	90	3760	Landers	7.3	strike slip	45.5	430	13.6
	91	6963	Darfield, New Zealand	7	strike slip	57.7	638	13.9
	92	3955	Tottori, Japan	6.6	strike slip	40.1	671	14.0
	93	3923	Tottori, Japan	6.6	strike slip	46.8	610	14.1
	94	551	Chalfant Valley-02	6.2	strike slip	31.2	382	14.2
	95	4485	L'Aquila, Italy	6.3	Normal	36	650	14.4
	96	815	Griva, Greece	6.1	Normal	29.2	455	14.4
	97	925	Big Bear-01	6.5	strike slip	59.9	509	14.8
	98	290	Irpinia, Italy-01	6.9	Normal	29.8	429	14.8
	99	548	Chalfant Valley-02	6.2	strike slip	21.9	371	15.0

Table A.1 Selected Ground Motions (continued)

Group #	EQ #	RSN	Event	Mg	Fault Mechanism	Rrup (km)	Vs30 (m/s)	PGA/PGV (1/s)
Group 10	100	301	Irpinia, Italy-02	6.2	Normal	44.4	429	15.4
	101	2753	Chi-Chi, Taiwan-04	6.2	strike slip	39.3	804	15.5
	102	80	San Fernando	6.6	Reverse	21.5	969	16.2
	103	5483	Iwate, Japan	6.9	Reverse	39.4	829	16.8
	104	643	Whittier Narrows-01	6	Reverse Oblique	27.6	1223	25.0
	105	703	Whittier Narrows-01	6	Reverse Oblique	50.4	996	27.3
	106	1649	Sierra Madre	5.6	Reverse	39.8	996	32.3
	107	5679	Iwate, Japan	6.9	Reverse	56.7	934	32.5
	108	4438	Molise-02, Italy	5.7	strike slip	51.3	865	34.9
	109	5680	Iwate, Japan	6.9	Reverse	40.4	850	41.2
	110	5685	Iwate, Japan	6.9	Reverse	57.2	859	42.2